Drew University

College of Liberal Arts

Comparing the Kinetic Behavior of Aldo-Keto Reductases Isolated from *Saccharomyces cerevisiae*

A Thesis in Biochemistry and Molecular Biology

By

Abigail Goldman

Submitted in Partial Fulfillment

of the Requirements

for the Degree of

Bachelor of Science

With Specialized Honors in Biochemistry and Molecular Biology

May 2026

Abstract

Aldo-keto reductases (AKRs) are a superfamily of enzymes that reduce carbonyls to alcohols in a stereospecific manner, making them useful for biocatalysis. Previous studies of the α-amide ketoreductase variant AKR 163 from the *Saccharomyces cerevisiae* strain SC108 have found that it exhibits substrate inhibition. In particular, AKR 163 is only inhibited by substrates with electron-withdrawing groups, such as ethyl-4-chloroacetoacetate (E4ClAA), ethyl-2-fluoroacetoacetate (E2FAA), and ethyl pyruvate (EP). To test the generality of substrate inhibition in AKRs, AKR 308, a variant of D-arabinose dehydrogenase (Ara1), was overexpressed in *E. coli* and purified via glutathione affinity chromatography. In contrast to AKR 163, AKR 308 exhibited Michaelis-Menten kinetics with E4ClAA, E2FAA, and 2,3-pentanedione (2,3-PD). AKR 308 displayed both substrate inhibition and cooperativity with EP, with a Hill coefficient of 3.9. Overall, AKR 308 exhibited higher turnover numbers and greater K_M values than AKR 163 with these substrates, with k_{cat} values between 1.5 and 7 s^{-1} and K_M values between 6.7 and 80 mM. AKR 308 also displayed distinct kinetic behavior from AKR 163 with ethyl acetoacetate (EAA) analogs containing alkyl substituents. Whereas increased steric bulk at the C2 position decreased AKR 163's k_{cat}, AKR 308-catalyzed ethyl-2-ethylacetoacetate reduction displayed a higher k_{cat} of 4.5 s^{-1} compared to 0.8 s^{-1} for EAA. Substantial AKR 308 activity was not observed with 2,4-pentanedione or 1,1,1-trifluoro-2,4-pentanedione, suggesting that β-ketone carbonyls are not effective AKR 308 substrates, even if they have electron-withdrawing substituents. Fluorescence titrations yielded a K_D value of 1.2 ± 0.2 μM for $NADP^+$ binding to AKR 308, compared to a K_D value of 0.5 ± 0.1 μM for $NADP^+$ binding to AKR 163. This indicates that AKR 308 has slightly lower affinity for $NADP^+$

compared to AKR 163. Substrate docking with Cresset Flare revealed that EP adopts nonproductive poses in Ara1's active site that are more energetically favorable than the catalytic pose, whereas E4ClAA and 2,3-PD do not. Allosteric pockets were generated using PASSer to investigate potential mechanisms of EP's cooperativity, and a pocket that favors binding of EP over E4ClAA and 2,3-PD was identified. However, this pocket has a low calculated probability of being an allosteric site. These findings indicate that AKR 163's mechanism of substrate inhibition is not general across yeast AKRs, as AKR 308's substrate inhibition appears to be mediated by nonproductive pose formation rather than binding of substrate to the enzyme-$NADP^+$ complex. Furthermore, this study identifies conditions under which AKR 163 and AKR 308 would be most optimal for biocatalysis, demonstrating the importance of enzyme screening studies.

Table of Contents

List of Figures and Tables

Background

Overview

A common issue faced by the pharmaceutical industry is the need for more efficient and environmentally friendly methods to synthesize chiral drugs. To solve this problem, pharmaceutical companies are increasingly turning to biocatalysis, where enzymes are used to synthesize chiral molecules in a stereospecific manner that eliminates the need to remove the unwanted enantiomer.[1] Aldo-keto reductases (AKRs) are particularly useful for the production of chiral alcohols.[2] This superfamily of oxidoreductases reduces aldehydes and ketones to alcohols via hydride transfer from NADPH, which is oxidized to $NADP^+$.[3] AKRs share a common $(\alpha/\beta)_8$-barrel fold structure, catalytic tetrad, and ordered bi-bi reaction mechanism.[3] Screening studies have characterized the substrate specificities of novel AKRs, with the goal of identifying AKRs that are useful for certain biocatalytic applications. For example, Zarina Akbary identified five AKRs from the *Saccharomyces cerevisiae* strain SC108, which was isolated from ancient amber, that demonstrated stereospecific reduction of α- and β-keto esters.[4] An SC108 AKR called AKR 163 was selected for further study and found to exhibit substrate inhibition with substrates containing electron-withdrawing groups, which would impair biocatalysis.[5] It was hypothesized that electron-withdrawing substituents increase the rate of the hydride transfer step, allowing a second substrate molecule to bind to the enzyme-$NADP^+$ complex and block further catalysis.[5] The present study aimed to systematically compare AKR 163's behavior to another SC108 AKR called AKR 308 in order to determine whether AKR 163's mechanism of substrate inhibition is general across yeast AKRs.

Enzyme Kinetics and Industrial Applications

Biocatalysis in the Pharmaceutical Industry

The chirality of a drug is one of the most important considerations in pharmaceutical synthesis. Chiral molecules have four unique substituents attached to a central atom. These molecules exist as two non-superimposable mirror images called enantiomers (Figure 1). Enantiomers share the same physical properties, but they differ in chemical properties and thus in the molecules with which they interact. As a result, enantiomers of a drug may exhibit different reactivity with biomolecules. Often, one enantiomer of a drug, termed the eutomer, will have the desired reactivity, while the other enantiomer, termed the distomer, will have no effect or may even cause harm.[6] Due to this phenomenon, the U.S. Food and Drug Administration released guidelines in 1992 mandating that pharmaceutical companies characterize the biological activity of each enantiomer of a drug and justify the decision to market a drug as a racemate, or as a mixture of both enantiomers.[6] These guidelines have promoted a shift toward marketing chiral drugs as single enantiomers. However, traditional organic methods for stereospecific synthesis often involve hazardous and expensive chemical catalysts as well as complex and wasteful procedures for removing the distomer. Therefore, it is of interest to develop more efficient and environmentally friendly methods for the synthesis of chiral drugs.

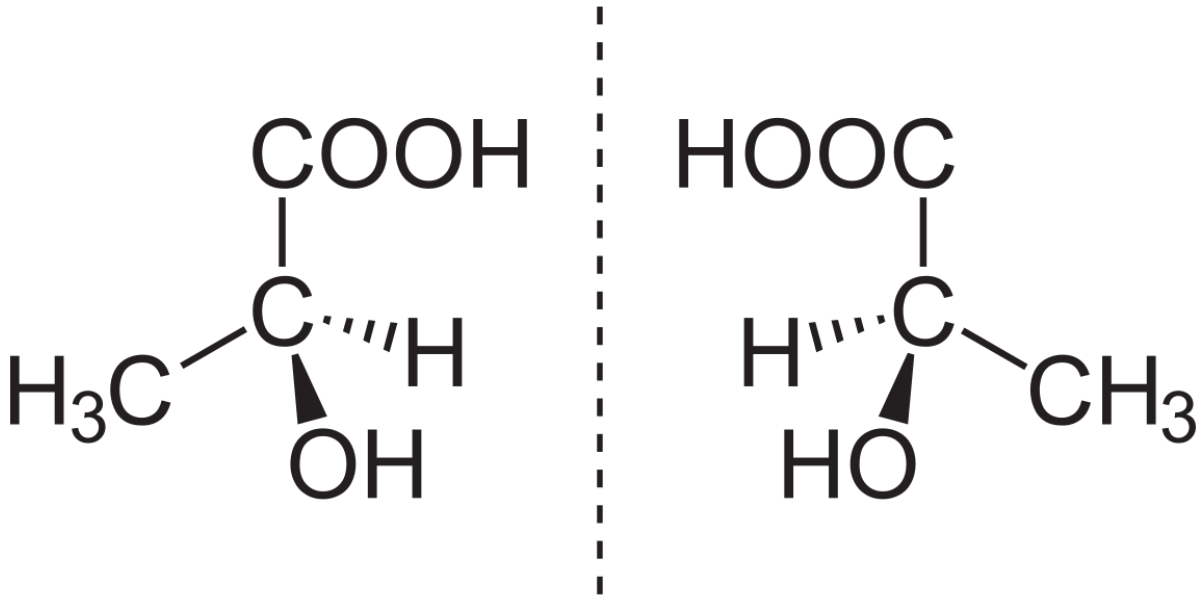

Figure 1. Two enantiomers of a chiral molecule. The enantiomers are mirror images of each other.

One solution is biocatalysis, or the use of enzymes to catalyze industrial reactions. Enzymes are biological catalysts that increase the rate of biochemical reactions. They are highly specific for certain reactants, or substrates. As catalysts, enzymes are not consumed in the reaction, allowing them to achieve a high turnover rate. Biocatalysis is utilized as an alternative to chemical catalysts in a wide variety of industries to increase product yield, minimize cost, and reduce environmental impacts. Examples include the use of proteases in detergents to help remove stains, the use of α-amylase to catalyze the first step in the conversion of starch to fructose, the use of phytases as animal feed additives to improve phosphorus uptake, the use of transglutaminase as a texturing agent, and the use of lipolytic enzymes as emulsifiers in the baking industry.[7] Many enzymes are also highly stereospecific, producing a single enantiomer of the product. As a result, biocatalysis is an attractive option for synthesizing enantiopure chiral

drugs, eliminating the need for costly chemical catalysts and distomer removal. In addition, enzymes are biodegradable, and enzymatic syntheses require fewer steps and can be carried out under mild conditions,[1] making biocatalysis a more sustainable alternative. For these reasons, interest in pharmaceutical biocatalysis has increased rapidly in the past 25 years.

The syntheses of the anti-ulcer drug dexlansoprazole and the GABA analogue Pregabalin illustrate the advantages of biocatalysis over traditional organic synthesis. Dexlansoprazole contains a chiral sulfur atom, as shown in Figure 2. Raju et al's[8] chemocatalytic synthesis of dexlansoprazole employs a chiral titanium catalyst for asymmetric sulfoxidation, requiring a wasteful crystallization process to remove the undesired (*S*) enantiomer, expensive reagents, multiple synthetic and work-up steps, and the use of heating and cooling. Liu et al.[9] sought to develop a biocatalytic alternative for dexlansoprazole synthesis involving *Cb*BVMO, a Baeyer-Villager monooxygenase from *Cupriavidus basilensis*. Using a whole-cell biocatalytic system of *E. coli* cells expressing *Cb*BVMO, the authors achieved 99% enantiomeric excess (ee) and 100% conversion of the starting material. Compared to Raju et al.'s procedure, the biocatalytic synthesis of dexlansoprazole has a much-reduced environmental impact. Liu et al.'s synthesis generates less waste because it does not require removal of the unwanted enantiomer, which also explains the higher yield. The biocatalytic approach also requires only one synthetic step, involves relatively inexpensive and safe reagents, and can be completed at 30 °C.

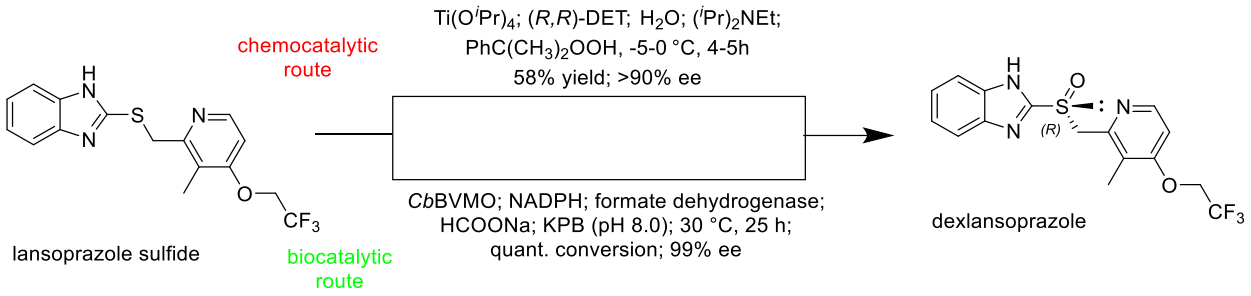

Figure 2. Comparison of the chemocatalytic route[8] to dexlansoprazole synthesis (top) with the more efficient biocatalytic route[9] (bottom). Adapted from Rossino et al.[1]

Similarly, the biocatalytic synthesis of Pregabalin is more efficient and environmentally friendly than the first-generation synthesis (Figure 3), which used (*S*)-mandelic acid resolution and recrystallization as the final steps to obtain the desired (*S*) enantiomer.[1] Martinez et al.'s[10] biocatalytic synthesis employs a commercial Lipolase enzyme that reacts only with the (*S*) enantiomer of the starting material, allowing the stereocenter to be set in the first step of the synthesis. The undesired (*R*) enantiomer can then be recycled to improve the yield. Compared to the first-generation synthesis, the biocatalytic synthesis uses a lower amount of chemicals and solvents, doubles the yield, and reduces the environmental factor (E factor) from 86 to 17. Pregabalin is also obtained with 99.5% purity and 99.75% ee. These syntheses illuminate the immense power of biocatalysis in terms of achieving enantioselectivity, improving yield, and minimizing environmental impact.

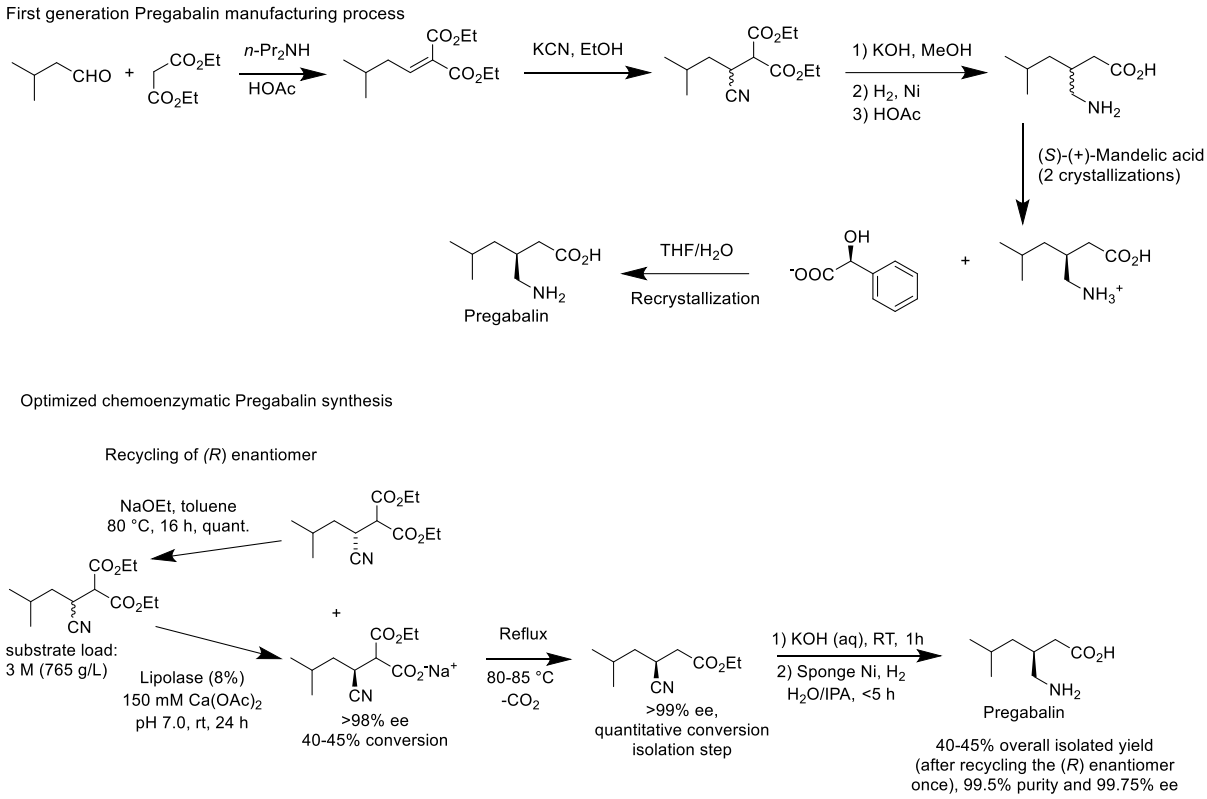

Figure 3. Comparison of the first-generation route to Pregabalin synthesis with the more efficient biocatalytic route. Adapted from Martinez et al.[10]

Protein engineering and directed evolution offer an opportunity to optimize catalytic efficiency and expand the scope of organic reactions suitable for biocatalysis. These techniques allow scientists to overcome common problems associated with biocatalysis, such as narrow or promiscuous substrate specificity, environmental tolerance, and high substrate loading.[2] One example of successful enzyme engineering is the use of the *Arthrobacter* transaminase ATA-117 to synthesize the antidiabetic drug sitagliptin.[11] Wild-type ATA-117 exhibits a limited substrate specificity, and its binding pocket cannot accommodate prositagliptin ketone. Using site-directed mutagenesis, molecular docking, and directed evolution, Savile et al.[11] produced an ATA-117 variant with vastly improved activity toward prositagliptin. Further protein engineering produced

a variant that could tolerate the environmental conditions required for the large-scale manufacturing of sitagliptin, such as high temperature and substrate loading. The most effective ATA-117 variant produced sitagliptin with >99.95% ee and a 92% yield, demonstrating improvements over the previous rhodium-catalyzed process in terms of yield, waste production, and cost. Thus, protein engineering allows researchers to maximize the potential of enzymes for stereospecific pharmaceutical synthesis.

The Enzymatic Mechanism of Rate Enhancement

In order to optimize the biocatalytic potential of enzymes, it is essential to first understand how they function. Enzymes increase the rate of a reaction by facilitating the formation of the transition state, which is the highest-energy structure between reactants and products.[12] Achieving the transition state requires an input of free energy known as the activation energy, or $\Delta G^{\ddagger}$ (Figure 4). The activation energy determines the rate of a chemical reaction; higher activation energies require a greater input of free energy, leading to a slower rate of reaction.

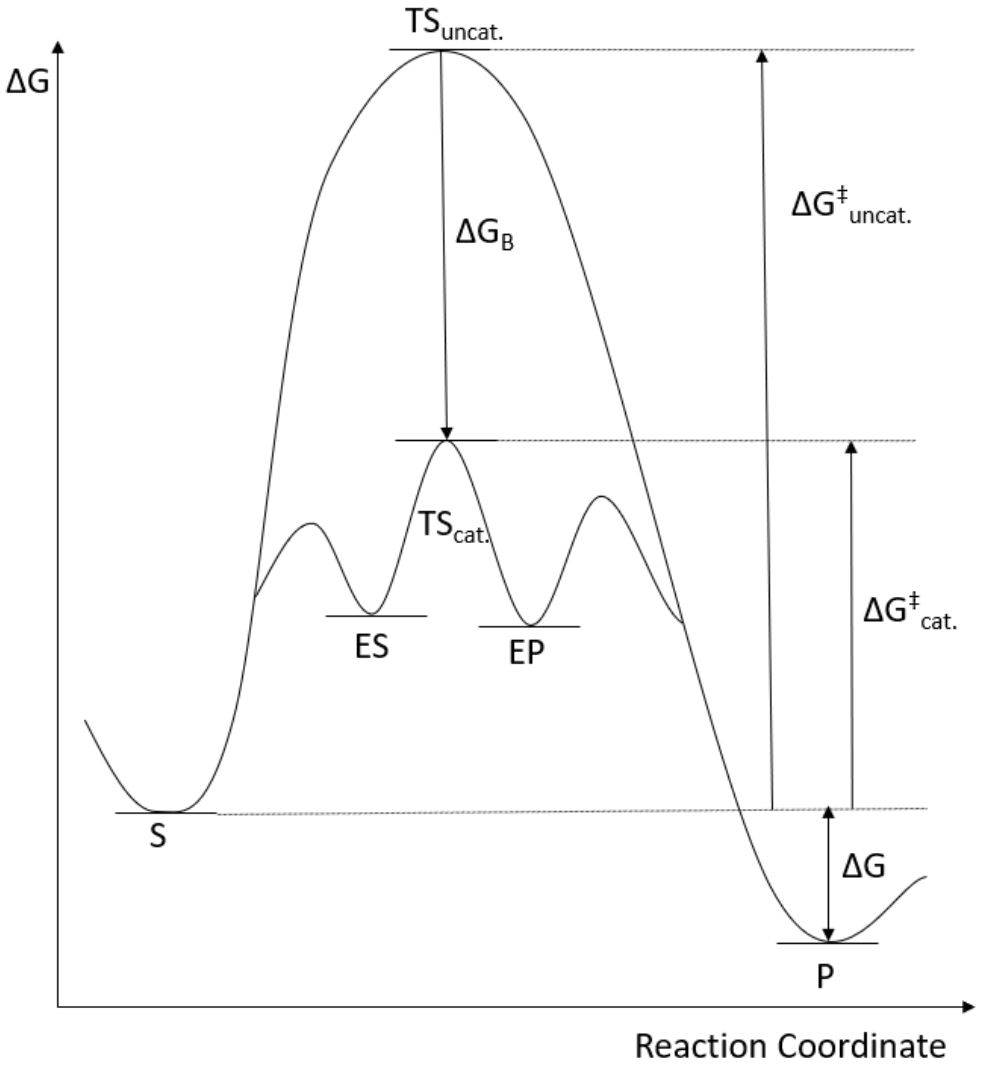

Figure 4. Reaction coordinate diagrams for uncatalyzed (top) and enzyme-catalyzed (bottom) reactions. S = substrate, ES = enzyme-substrate complex, TS = transition state, EP = enzyme-product complex, $\Delta G^{\ddagger}$ = activation energy, and ΔG_B = binding energy. Adapted from Scholey[13].

An enzyme's ability to lower a reaction's activation energy relates to the formation of the enzyme-substrate complex. This occurs when a substrate binds to an enzyme's active site, which is a three-dimensional cleft with high affinity for the substrate.[12] Noncovalent interactions

between the enzyme and substrate lead to a release of free energy known as the binding energy (ΔG_B). The enzyme has the greatest affinity for the transition state; in other words, the active site exhibits the greatest number of noncovalent interactions with the transition state. Thus, when the transition state is achieved, the maximum binding energy is released. Through this mechanism, the enzyme stabilizes the transition state and makes its formation more energetically favorable,[14] lowering the reaction's activation energy and increasing the rate of the reaction.

Enzymatic rate enhancement has significant consequences for biology. While the half-lives of uncatalyzed biochemical reactions can range up to millions of years, enzymes generally catalyze reactions with k_{cat} values of 100-1000 s^{-1}, equating to half-lives of less than a second.[15] In the absence of enzymes, these reactions would not occur at sufficiently fast rates to sustain life.

It is important to note that enzymes do not affect the overall equilibrium of a reaction (ΔG). In other words, enzymes do not affect the equilibrium concentrations of the substrate and product or the free energy difference between them.[14] Instead, enzymes increase the rate at which the reaction proceeds toward equilibrium.

Michaelis-Menten Kinetics

The study of enzyme kinetics allows researchers to quantify the speed of enzyme-catalyzed reactions, investigate substrate preference, and optimize conditions for biocatalysis.[12] The Michaelis-Menten model (Figure 5), first derived experimentally by Leonor Michaelis and Maud Menten in 1913,[16] describes the most common type of enzymatic kinetic behavior. In this model, reaction velocity initially increases in a linear fashion as substrate concentration

increases. Eventually, all enzyme active sites become saturated with substrate, and increases in substrate concentration no longer affect the reaction velocity, causing it to plateau. Enzymes that follow Michaelis-Menten kinetics produce a hyperbolic velocity vs substrate concentration curve, as shown in Figure 5.

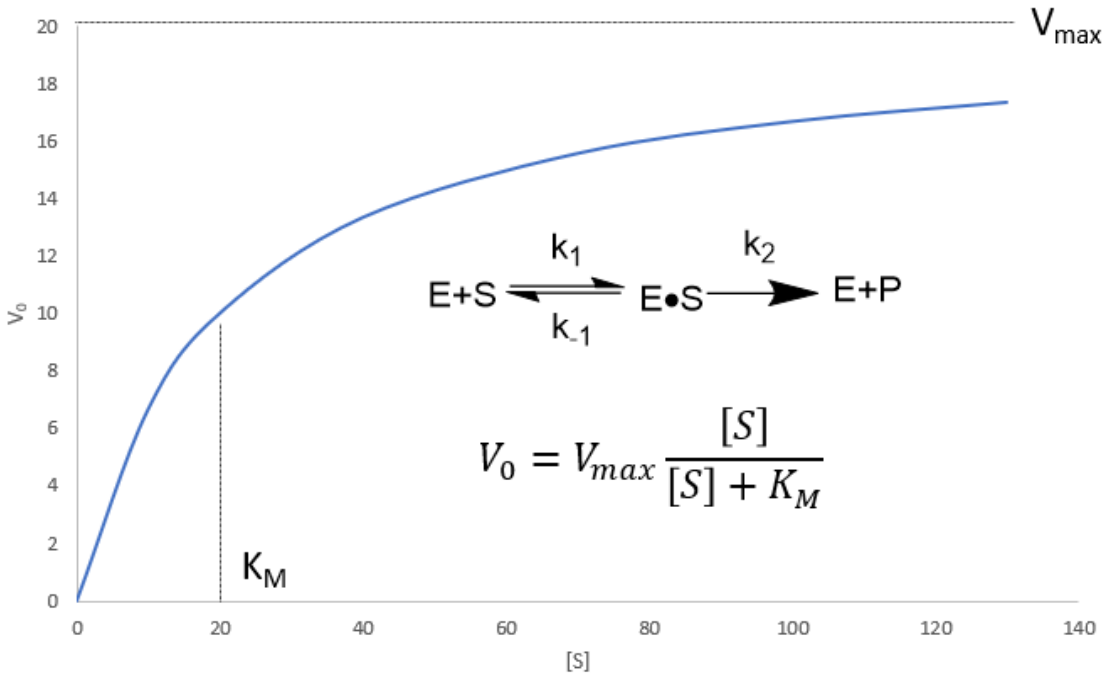

Figure 5. Reaction velocity vs concentration plot for an enzyme that exhibits Michaelis-Menten kinetics. The V_{max} and K_M for this reaction are labeled. The Michaelis-Menten reaction mechanism (top) and the Michaelis-Menten equation (bottom) are also shown. Because the Michaelis-Menten model only considers initial reaction velocities, k_{-2} was omitted from the mechanism.

The Michaelis-Menten model incorporates several key assumptions: 1) the enzyme and substrate form an enzyme-substrate (ES) complex that dissociates to enzyme and substrate or proceeds to product, 2) velocities are measured at the initial stage of the reaction, before the

reverse reaction becomes consequential, 3) the rate of the enzyme-catalyzed reaction is proportional to the concentration of the ES complex, 4) the substrate concentration is much larger than the enzyme concentration, and 5) the rate of change of the ES complex concentration is negligible compared to the rate of change of the substrate and product concentrations. A mechanism that satisfies the first two assumptions is shown in Figure 5. From these five assumptions, one can derive the Michaelis-Menten equation, which is also shown in Figure 5. A full derivation of the Michaelis-Menten equation is presented in the Appendix.

In the Michaelis-Menten equation, [S] represents the substrate concentration, V_0 represents the initial reaction velocity (dependent on substrate concentration), and V_{max} represents the reaction velocity when the enzyme is saturated with substrate. Dividing V_{max} by the enzyme concentration yields k_{cat}, or the enzyme's turnover number, which is equivalent to the rate constant k_2 for product formation. k_{cat} is a measure of an enzyme's catalytic power, where higher values indicate faster catalysis.

K_M is defined as follows:

$$K_M = \frac{k_{-1} + k_2}{k_1}$$

K_M can also be defined as the substrate concentration necessary to achieve a reaction velocity equivalent to half of V_{max}. Under this definition, K_M can be used to approximate an enzyme's affinity for a substrate, particularly if the catalytic step is slower than dissociation of the enzyme-substrate complex. A lower K_M indicates that a lower substrate concentration is necessary to achieve ½ V_{max}, which indicates higher affinity for the substrate. Dividing k_{cat} by

K_M yields the catalytic efficiency, which reflects an enzyme's preference for a particular substrate. Higher efficiency values indicate greater preference for a substrate.

Non-Michaelis Menten Kinetics

Most enzymes obey Michaelis-Menten kinetics, but it is not the only type of enzymatic kinetic behavior. The most common deviation from Michaelis-Menten kinetics is substrate inhibition,[17] where the enzyme is inhibited by its own substrate. In this model, the velocity curve reaches a maximum and then decreases with increasing substrate concentration (Figure 6). Substrate inhibition is commonly attributed to a second substrate molecule binding to the ES complex, forming a dead-end SES complex that cannot proceed to catalysis,[17,18] as shown in the mechanism in Figure 6. However, binding of the inhibitory substrate to the enzyme-product complex has been demonstrated as well.[17] The equation for substrate inhibition is shown in Figure 6. In this equation, K_i represents the inhibitory constant, or the substrate concentration at which 50% of the enzyme molecules are inhibited.

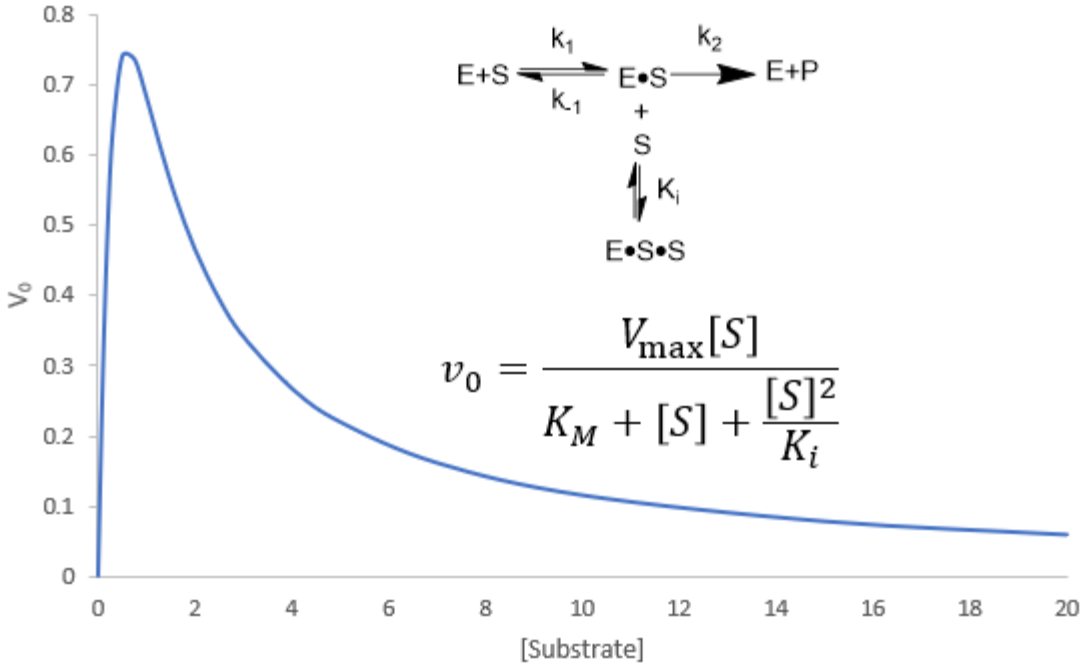

Figure 6. Reaction velocity vs concentration plot for an enzyme that exhibits substrate inhibition. The reaction velocity approaches zero as substrate concentration increases. The mechanism for substrate inhibition (top) and the substrate inhibition equation (bottom) are also shown.

Substrate inhibition occurs in 25% of known enzymes,[17] suggesting that it serves a biological purpose. In fact, there are several examples of the biological relevance of substrate inhibition, which are summarized by Reed et al.[19] For example, the glycolytic enzyme phosphofructokinase is inhibited by high concentrations of its substrate ATP. This phenomenon is logical in the context of glycolysis; further production of ATP is unnecessary if the cell's ATP requirements are met. Additionally, acetylcholinesterase displays inhibition by its substrate acetylcholine, ensuring that acetylcholine is only degraded after post-synaptic receptor binding, when concentrations in the synapse are low. Finally, tyrosine hydroxylase is inhibited by its

substrate tyrosine, ensuring that dopamine synthesis remains constant despite fluctuations in tyrosine concentration in the brain before and after meals.

Cooperativity is another example of deviation from Michaelis-Menten kinetics. This behavior is most commonly observed with oligomeric enzymes that contain multiple active sites. In the concerted model of cooperative behavior, an enzyme exists in an equilibrium between two forms: the T state, which has low affinity for substrate, and the R state, which has high affinity for substrate.[20] At low substrate concentrations, most of the enzyme molecules are in the T state. As the substrate concentration increases, substrate binding to the T state causes conformational changes that convert all subunits to the R state, reflected by E* in the mechanism shown in Figure 7. In this process, each active site acquires higher affinity for the substrate. Binding of substrate to the R state reduces the number of unbound enzyme molecules in the R state, which results in increased conversion of the T state to the R state to maintain equilibrium. Consequently, the proportion of enzyme molecules in the R state increases as substrate concentration increases, producing a characteristic sigmoidal binding curve that displays an exponential increase in reaction velocity (Figure 7).

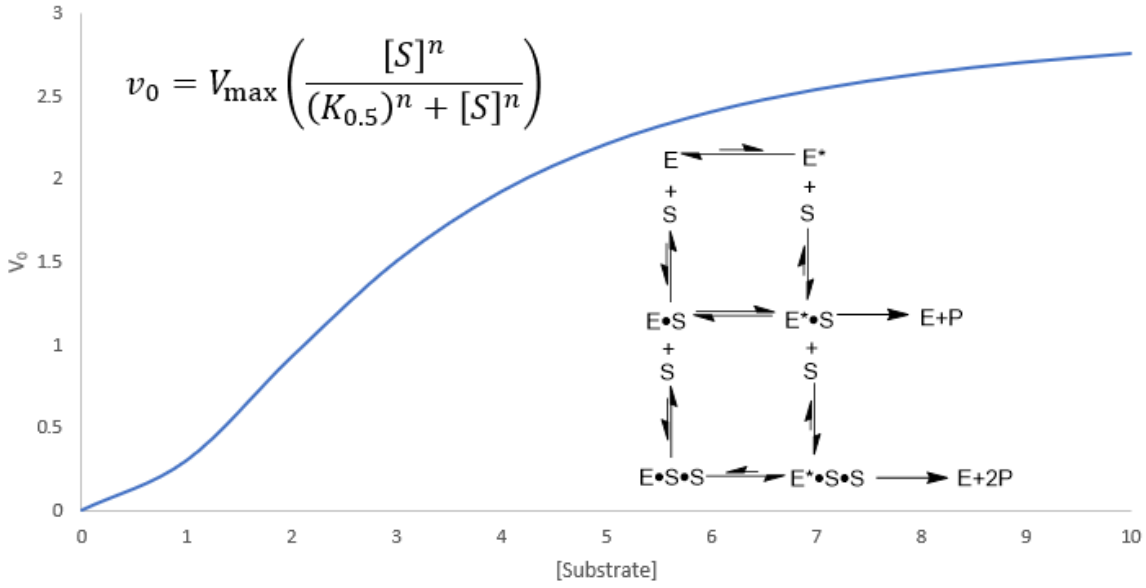

Figure 7. Reaction velocity vs substrate concentration plot for an enzyme that exhibits cooperative behavior. The velocity curve is sigmoidal, which is characteristic of cooperative behavior. The mechanism for cooperative behavior for a dimeric enzyme is shown in the bottom right, with E representing the T state and E* representing the R state. The Hill equation is shown in the upper left.

The Hill equation for cooperative behavior is shown in Figure 7. In this equation, $K_{0.5}$ represents the substrate concentration at which 50% of the enzyme molecules are bound by substrate, and n represents the Hill coefficient, which reflects the number of substrate binding sites.

Cooperative behavior is a useful concept in analyzing the effects of allosteric regulators, which bind outside the active site and control metabolic pathways. For cooperative enzymes, an allosteric inhibitor stabilizes the T state, reducing the enzyme's affinity for substrate, while an allosteric activator stabilizes the R state, increasing the enzyme's affinity for substrate.[20] Aspartate transcarbamoylase, which catalyzes the first step of pyrimidine nucleotide biosynthesis

by producing *N*-carbamoyl-L-aspartate from carbamoyl phosphate and aspartate, represents one example of this mechanism of allosteric regulation.[21] The substrate aspartate produces conformational changes that weaken the interactions stabilizing the T state, shifting the equilibrium toward the R state and promoting cooperative behavior. CTP, the end product of pyrimidine nucleotide biosynthesis, acts as an allosteric inhibitor that stabilizes the T state of aspartate transcarbamoylase. ATP, a precursor to carbamoyl phosphate, acts an allosteric activator that stabilizes the R state of aspartate transcarbamoylase. Through allosteric effects that modulate aspartate transcarbamoylase's cooperative behavior, CTP and ATP facilitate feedback and feedforward regulation of pyrimidine nucleotide biosynthesis, respectively, depending on the cell's needs.

Oxidoreductases and the Production of Chiral Alcohols

There are six major classes of enzymes: oxidoreductases, transferases, hydrolases, lyases, isomerases, and ligases.[14] While hydrolases are the most commonly used industrial enzymes,[2,14] oxidoreductases also play a significant role in biocatalysis. As the name suggests, oxidoreductases catalyze oxidation-reduction reactions, using a cofactor as an electron donor or acceptor.[22] About 80% of oxidoreductases use the closely related molecules NAD(H) and NADP(H) as cofactors.[2] Other cofactors include cytochrome, molecular oxygen, hydrogen peroxide, iron-sulfur proteins, and flavin.[22] The class of oxidoreductases encompasses dehydrogenases, monooxygenases, dioxygenases, oxidases, and peroxides. Biocatalytic applications of these enzymes include the oxidation of alcohols to aldehydes, asymmetric epoxidation of alkenes, sulfur oxidation, reduction of ketones and aldehydes to alcohols, reductive amination of aldehydes and ketones, carboxylic acid reduction to aldehydes, and

asymmetric hydrogenation.[2] One limitation of oxidoreductases is the requirement for a stoichiometric amount of NAD(P)(H).[22] This is often addressed by coupling the reaction to an enzymatic regeneration system that recycles the cofactor, such as glucose dehydrogenase (GDH).

Oxidoreductase-catalyzed reduction reactions are especially useful because they often yield chiral products. There is particular interest in using oxidoreductases to reduce ketones and aldehydes to chiral alcohols, which represent important functional groups and intermediates of many pharmaceuticals.[23] Alcohol dehydrogenases and aldo-keto reductases (AKRs) are the major superfamilies of oxidoreductases that catalyze these reactions.[2] Due to their broad substrate specificity, high enantioselectivity, and preference for reduction over oxidation,[24] AKRs are becoming increasingly prevalent in the biocatalytic production of chiral alcohols.[25] The remainder of this thesis will focus on the characteristics of AKRs as well as their biocatalytic applications.

Aldo-Keto Reductases: An Overview

AKRs are a superfamily of mostly monomeric, mainly NADP(H)-dependent oxidoreductases that catalyze the reduction of aldehydes and ketones to alcohols.[3] More than 190 AKRs had been identified as of 2015. AKRs are divided into 16 families, which are further divided into subfamilies based on shared sequence identity. These enzymes are expressed in all organisms, and they have a wide substrate specificity that includes sugars, lipid aldehydes, and ketosteroids as well as carcinogens like aflatoxin. While AKRs exhibit a strong preference for NADPH over NADH,[24] some AKRs exhibit dual NADPH/NADH specificity[26] or rely

exclusively on NADH[27]. Many AKRs share common features in their structure, catalytic mechanism, kinetic mechanism, and biological function, which are described below.

AKR Structure

AKRs share a common scaffold and cofactor binding site, but they exhibit some differences in active site construction and structural loops that contribute to substrate specificity. Aldose reductase, or AKR1B1, serves as a representative example of AKR structure (Figure 8). All AKRs adopt an identical $(\alpha/\beta)_8$-barrel fold, also known as a triose-phosphate isomerase (TIM) barrel.[28] The TIM barrel consists of eight central parallel β-strands alternating with α-helices, which form the outer layer and run antiparallel to the β-strands.[29] The amino terminus adopts a short antiparallel β-hairpin at the bottom of the TIM barrel.[28] AKRs also contain a variety of extraneous helices and loops that differ between subfamilies, contributing to variations in cofactor binding and substrate specificity.[24]

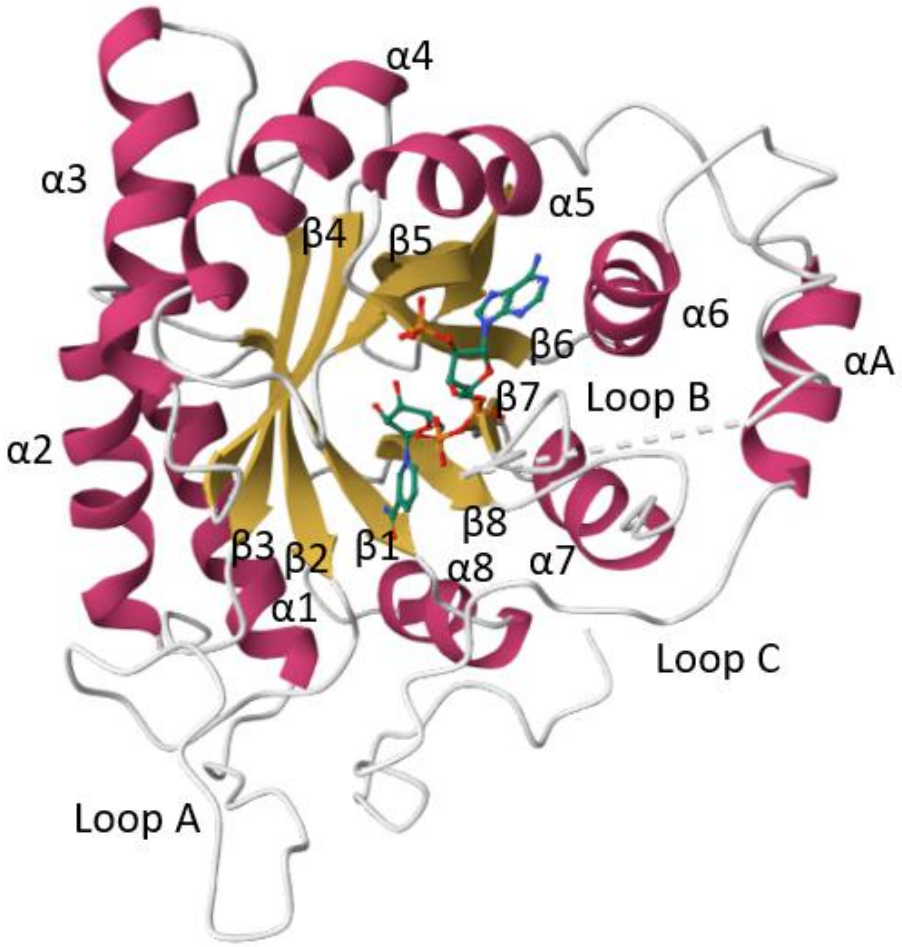

Figure 8. Crystal structure of NADPH-bound aldose reductase. This enzyme exhibits the TIM barrel and three large loops near the active site that are characteristic of AKRs. α-helices are shown in magenta, β-sheets are shown in yellow, and loops are shown in white. NADPH is shown in ball-and-stick form. This crystal structure was obtained from RCSB Protein Data Bank with identifier 1ABN and solved by Borhani et al.[30] Labeling of the loops was derived from Campbell et al.[31]

NADPH-binding residues are conserved across all AKRs, and the mechanism of cofactor binding is nearly identical. NADPH is bound in an extended conformation on the C-terminal side of the TIM barrel, with the nicotinamide ring situated in the β-sheet core and the pyrophosphate

bridge situated in the outer lip between the β-sheets and α-helices.[29] Upon NADPH binding, AKRs undergo a conformational change.[28] In rat liver 3α-hydroxysteroid dehydrogenase (3α-HSD, or AKR1C9), this conformational change occurs when Arg-276 forms a salt bridge with the adenine 2'-phosphate of NADPH, anchoring the cofactor in place.[32] Arg-276 is highly conserved across AKRs, implying that this binding mechanism is conserved as well.[29] In addition, some AKRs, such as aldehyde reductase (AKR1A1) and aldose reductase (AKR1B1), contain residues that form a salt-bridge "safety belt" over the pyrophosphate bridge, locking NADPH in place.[28] In AKR1B1, loop B represents the "safety belt" (Figure 8).[30] This "safety belt" contributes to increased affinity for the cofactor as well as the rate-limiting step of cofactor release,[28] which will be discussed in more detail later. NADPH binding also establishes the stereospecificity of AKRs. Due to aromatic π-stacking interactions between the nicotinamide ring and a Tyr or Trp residue, NADPH is always bound in the *anti* conformation.[28] As a result, the 4-*pro*-R hydrogen is always transferred from C4 of the nicotinamide ring to the substrate carbonyl.

While portions of the AKR active site are conserved, there are also regions of variation that account for substrate specificity. The substrate-binding site forms a cleft at the C-terminal end of the TIM barrel and consists of the oxyanion binding site (conserved Tyr and His residues and C-4 of the nicotinamide ring), residues at the edge of the active site, and three loops that form the sides of the cleft (loops A, B, and C in Figure 8).[29] Residues in the substrate-binding cleft are less conserved compared to residues that bind NADPH, and the size of the substrate-binding cleft is also highly variable.[28] Residues at the edge of the active site and in the three loops are particularly prone to variation, indicating that these regions determine substrate specificity.[28] For example, the residues at positions 54 and 118 at the edge of the active site vary

between aldose reductases and hydroxysteroid dehydrogenases, indicating that these residues discriminate between sugar and steroid substrates.[29] Thus, residues in these regions are excellent targets for protein engineering to alter substrate specificity for biocatalysis.

The Catalytic Tetrad

AKR active sites contain four conserved residues: Tyr-55, His-117, Lys-84, and Asp-50 (AKR1C9 numbering).[28] Because these four residues are critical for hydride transfer, they are referred to as the catalytic tetrad. In order for hydride transfer to occur, one of these conserved residues must act as a proton donor in the reduction reaction and as a proton acceptor in the oxidation reaction. Site-directed mutagenesis experiments showed that the catalytic tyrosine residue fulfills this role.[26,33,34]

Based on work with AKR1C9, Schlegel et al.[34] proposed a "push-pull" catalytic mechanism that incorporates Tyr-55 as the general acid/base and assigns catalytic roles to His-117, Lys-84, and Asp-50. The "push-pull" mechanism proceeds counterclockwise through Figure 9. The reduction direction begins with step 1 and ends with step 3. In step 2, a hydride is transferred from NADPH to the carbonyl, and Tyr-55 donates a proton to the carbonyl, generating the alcohol product and oxidizing NADPH to $NADP^+$. Additionally, His-117 protonates Tyr-55's hydroxyl group, enhancing Tyr-55's ability to act as a general acid. The oxidation direction begins with step 3 and ends with step 1. In step 4, Tyr-55 abstracts a proton from the alcohol, and a hydride is transferred from the alcohol to $NADP^+$, generating the carbonyl product and reducing $NADP^+$ to NADPH. Additionally, Lys-84 deprotonates Tyr-55's hydroxyl group, enhancing Tyr-55's ability to act as a general base. Asp-50's negatively charged

carboxyl group stabilizes the positive charge that forms on Lys-84 during this process. Thus, via proton shuttling, His-117 facilitates proton donation in the reduction direction, and Lys-84 facilitates proton removal in the oxidation direction. However, this mechanism of proton shuttling may not be universally applicable to all AKRs.[28] Kratzer et al.,[26] for example, concluded that Lys-80 and His-113 do not assist directly in catalytic proton transfer for xylose reductase.

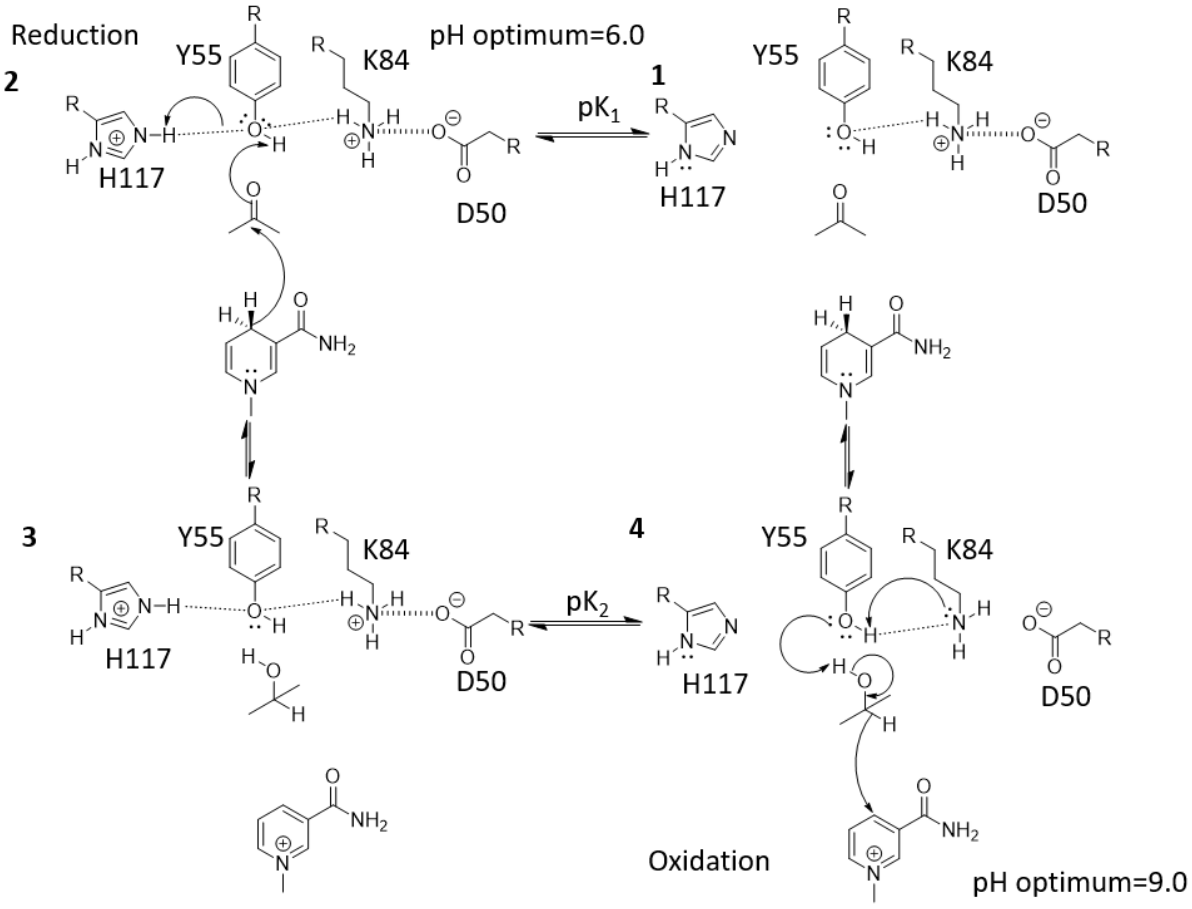

Figure 9. The "push-pull" mechanism of AKR catalysis. In the reduction reaction, His-117 protonates Tyr-55, facilitating proton donation. In the oxidation reaction, Lys-84 deprotonates Tyr-55, facilitating proton removal. Adapted from Schlegel et al.[34]

Residues in the catalytic tetrad also play indirect roles in catalysis. Bohren et al.[33] found that His-110 assists in substrate binding and determines substrate stereospecificity for AKR1B1, as mutation of His-110 prevented AKR1B1 from distinguishing between D-xylose and L-xylose. Kratzer et al.[26] also proposed that His-113 in xylose reductase positions the carbonyl substrate for hydride transfer. In xylose reductase, Lys-80 activates the electrophilic carbonyl group for hydride transfer. It also stabilizes partial negative charges on the carbonyl oxygen and Tyr-51's phenolic oxygen, contributing to an overall neutral charge in the active site. Finally, there is evidence that the catalytic Tyr may also function in substrate binding via hydrogen bonding to the carbonyl oxygen.[28]

The Kinetic Mechanism of AKRs

In addition to characterizing the catalytic mechanism of AKRs, it is of interest to determine their kinetic mechanism, or the order in which cofactor and substrate are bound to and released from the enzyme and the rates associated with each binding step. All AKRs follow an ordered bi-bi kinetic mechanism in both the reduction and oxidation directions,[3] as exemplified by pioneering studies on AKR1B1[35] and AKR1C9[36]. This kinetic mechanism is illustrated in Figure 10. The first step of an ordered bi-bi mechanism is the binding of cofactor to the enzyme. The enzyme then undergoes conformational changes (E to E*) such as cofactor anchoring[32] and "safety belt" formation[28] to achieve tighter cofactor binding, as described previously. Following the conformational change, the substrate binds to the enzyme, forming a ternary complex. Hydride transfer occurs, and the product is released from the enzyme-$NADP^+$ complex. The enzyme then undergoes another conformational change (E* to E), and $NADP^+$ is released.

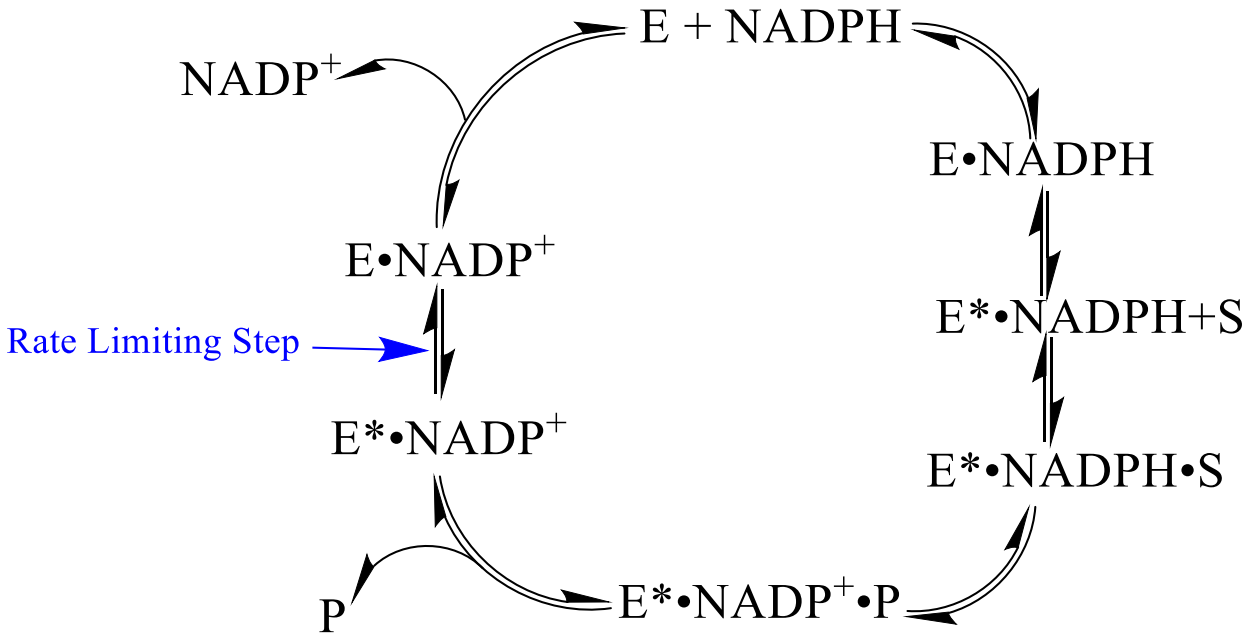

Figure 10. The ordered bi-bi kinetic mechanism for AKR-catalyzed reactions, where cofactor binding precedes substrate binding and cofactor release follows product release. E represents enzyme, S represents substrate, P represents product, and E* represents a conformational change. Figure from 2023 ACS Spring Meeting presentation by Akbary et al.[37]

When characterizing the kinetic mechanism of AKRs, it is also important to determine the rate-limiting step, or the slowest step of the reaction that determines the overall reaction rate. In the reduction direction, the rate-limiting step is typically the change from E* to E that precedes $NADP^+$ release, as the strong interactions between enzyme and cofactor facilitated by conformational changes like "safety belt" formation need to be broken.[28] Consistent with this prediction, the conformational change preceding $NADP^+$ release is the rate-limiting step in the reduction direction for both AKR1B1[35] and AKR2B5[26], as well as many other AKRs. However, exceptions do occur, such as AKR1C9[32,36].

Microbial AKRs

Microbial AKRs, or AKRs derived from bacteria, yeast, and fungi, represent the most common source of enzymes for biocatalysis. In general, microbial enzymes are easier to obtain and purify compared to plant and animal sources, and microorganisms exhibit greater availability, generate less waste, and display higher stability under the conditions necessary for industrial reactions, making microbial enzymes more cost-effective overall.[14] The use of microorganisms also permits simple genetic manipulation via plasmid insertion, allowing researchers to easily produce novel or mutated enzymes with new biocatalytic applications.[14]

Understanding the physiological function of microbial AKRs is also important, as it can provide clues to substrate specificity as well as insight into the function of homologous human AKRs. One common finding is that microbial AKRs serve a crucial role in stress responses, similar to their human counterparts. For example, upregulation of the *AKR* gene was observed in *Candida glabrata* isolates that were resistant to the antifungal drugs fluconazole and itraconazole,[38] suggesting that this AKR protein is important in detoxification. *Saccharomyces cerevisiae* also produces several AKRs involved in stress responses. Triple mutation of the *YPR1*, *GRE3*, and *GCY1* increased the susceptibility of *S. cerevisiae* cells to heat shock.[39] In addition, triple and pentuple deletion of *S. cerevisiae* AKRs produced several markers of oxidative stress, including decreased glutathione levels, nuclear localization of the transcription factor Yap1, and upregulation of oxidative stress regulatory genes.[40] These mutants also displayed defects in transcription, as evidenced by their dependence on inositol supplementation.[40] Significantly, Ypr1, Gre3, and Gcy1 display considerable homology with AKR1B1,[41] and transformation of the triple-null *S. cerevisiae* mutant with AKR1B1 partially rescues heat shock sensitivity[39]. Thus,

microbial AKRs are important not only in biocatalysis but also in advancing our understanding of human AKRs.

AKRs in Biocatalysis

AKRs are of great interest in the pharmaceutical and fine chemical industries for the stereospecific synthesis of chiral alcohols. In many cases, the AKR-catalyzed reactions are greener and more efficient than chemocatalytic or even other biocatalytic alternatives. Like other enzymes utilized in biocatalysis, AKRs are often engineered for improved substrate specificity and environmental tolerance.

One example of an AKR-catalyzed large-scale industrial process is the synthesis of an intermediate of the asthma and allergy drug Montelukast (Figure 11a).[42] Previously, scientists used the chemical catalyst (-)-DIP-Cl to set montelukast's single stereocenter. However, this catalyst exhibits several problems, such as corrosivity, poor atom economy, complicated workup procedures, and large amounts of waste. In order to develop a biocatalytic alternative, Liang et al.[42] selected AKRs from Codexis' collection that reduced the montelukast intermediate and then performed directed evolution to obtain variants with improved activity, thermal stability, and organic solvent tolerance. The most optimal engineered AKR exhibited 3000-fold higher activity and produced the chiral alcohol with greater than 95% yield and greater than 99% ee. Compared to the (-)-DIP-Cl synthesis, use of an AKR reduced the process mass intensity (PMI) by 30%.

AKRs have also been utilized in the industrial production of (*R*)-2-methylpentanol (Figure 9b), an intermediate for several pharmaceuticals and liquid crystals.[43] Previous chemocatalytic and chemoenzymatic kinetic resolution procedures for racemic 2-

methylvaleraldehyde reduction displayed low enantioselectivity, requiring additional steps or high pressure to achieve high ee. Gooding et al.[43] performed directed evolution of a *Lactobacillus kefir* AKR under desired process conditions, successively improving the enantioselectivity, activity, and thermal stability of the AKR variants. The final AKR variant met the process goals, achieving 45% conversion in 28 hours with 99.93% product purity and 98.22% ee in a one-step reaction.

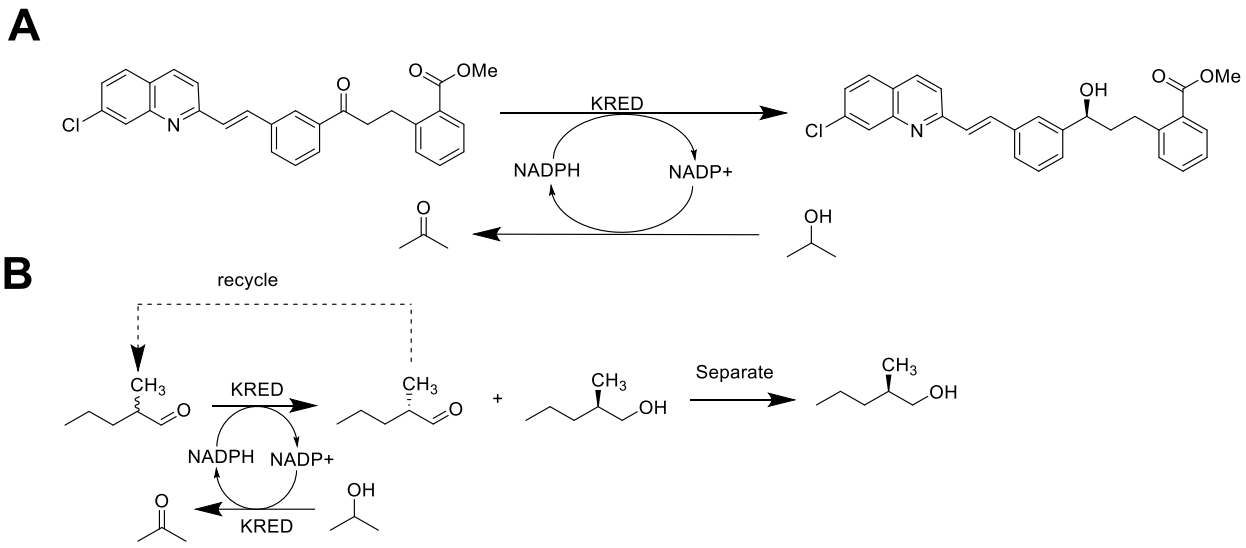

Figure 11. Use of engineered AKRs for the enantioselective, biocatalytic production of montelukast[42] (a) and (*R*)-2-methylpentanol[43] (b). KRED = keto-reductase.

Human AKRs

Human AKRs represent another important area of AKR research. These enzymes are some of the most well-characterized AKRs in terms of their structure, function, and substrate specificity, and they exhibit some similarities with microbial AKRs. Furthermore, certain human AKRs represent disease targets and serve as the primary metabolizing enzymes of various drugs.

The human AKRs exhibit a variety of physiological functions. One of their most important functions is detoxification of lipid aldehyde electrophiles produced under oxidative stress, which are linked to atherosclerotic plaques and neurodegenerative diseases.[44] AKR1C1 reduces one such lipid aldehyde, 4-hydroxy-2-nonenal, with high catalytic efficiency, and it is induced under conditions of oxidative stress.[45] In addition, human AKRs function in steroid metabolism. For example, AKR1C1 converts progesterone to the inactive form 20α-hydroxyprogesterone, and AKR1C3 converts estrone to estradiol, the active form of estrogen.[46] As a result, these enzymes regulate access of estrogens and progestins to their receptors, altering the biological response produced by these hormones. Finally, human AKRs function in the metabolism of retinoic acid, which binds to peroxisome proliferator-activated receptor γ (PPARγ) and exhibits anti-proliferative effects.[44] AKR1B1 and AKR1B10 reduce retinal to retinol,[47] preventing retinal from being oxidized to retinoic acid and thus inhibiting retinoic acid signaling.

In addition to their physiological substrates, human AKRs metabolize a number of xenobiotic substrates. This includes the tobacco carcinogen 4-methylnitrosamino-1-(3-pyridyl)-1-butanone (NNK)[48] and the liver carcinogen aflatoxin.[49] Human AKRs also metabolize various pharmaceuticals.[24] For example, the AKR1C enzymes reduce the anticancer drug oracin,[50] the opioid overdose medication naloxone, and the beta blocker befunolol.[51] Aldehyde reductase contributes to metabolism of the anticancer drug daunorubicin, and it is the primary enzyme that reduces the diabetes drug acetohexamide in the liver.[51]

Several human AKRs are implicated in disease and represent important drug targets. For example, AKR1B1 is linked to diabetic complications like neuropathy and nephropathy because it converts excess glucose to the hyperosmotic sugar sorbitol.[3] In addition, AKR1B10 is

overexpressed in smokers' non-small cell lung carcinoma.[52] AKR1B10's role in inhibiting the retinoic acid pathway, which exerts anti-proliferative effects and promotes tumor cell differentiation, may explain its link to cancer.[3,47] Abnormal expression of AKR1C1 and AKR1C3 has also been observed in endometrial cancer, which may contribute to the dysregulation of progesterone and estradiol levels that is characteristic of this type of cancer.[46] Inhibition of these AKRs represents an attractive strategy to treat cancer and diabetes, and a number of AKR inhibitors are in preclinical and clinical development.[3] For example, diabetes patients treated with the AKR1B1 inhibitor fidarestat displayed improvement in several symptoms of diabetic peripheral neuropathy compared to the placebo group.[53] Additionally, the AKR1B10 inhibitor oleanolic acid inhibits the growth of cancer cells overexpressing AKR1B10.[54] Overall, the study of human AKRs is important from both a functional and pharmacological perspective.

Screening Approaches

In order to design a large-scale biocatalytic process that incorporates AKRs, it is essential to first identify AKRs with some activity toward the desired carbonyl. Once an initial AKR has been identified, protein engineering and optimization can occur. Thus, the first step in biocatalysis often involves screening various AKRs for activity toward the desired substrate, which can be cumbersome due to the large number of AKRs and microbial sources. One alternative is to consult previous studies in which AKRs were screened against broad categories of substrates. While these studies may include industrially important chemicals or pharmaceutical precursors, their major focus is on establishing AKR substrate specificity or identifying AKRs that are particularly useful for reduction of certain carbonyls. For instance, Kaluzna et al.[55,56] characterized the activities of 18 purified *S. cerevisiae* AKRs toward various α-

and β-keto esters. These researchers also determined the stereoselectivity of each reduction reaction, a particularly helpful metric for biocatalysis. In another example, Ni et al.[57] screened 11 *E. coli* strains overexpressing *Bacillus* oxidoreductases, and they selected YtbE for further analysis on the basis of 2-chloroacetophenone reduction. Ni et al. characterized YtbE's activity and enantioselectivity with 20 aromatic ketones and keto esters, including the important pharmaceutical intermediate ethyl 4,4,4-trifluoroacetoacetate. Finally, Liang et al.[58] utilized a gene mining approach to identify five microbial AKRs with high catalytic activity toward bulky ketones, which are characteristic pharmaceutical intermediates. All of these AKRs reduced the bulky ketones with almost 100% ee, demonstrating their potential utility in biocatalysis.

While many screening approaches utilize AKRs from established microbial strains like *S. cerevisiae*, there is also the potential to consider novel sources of AKRs. One example is ancestral microbial strains, which may possess distinct ketoreductase activity compared to their modern-day counterparts. Pursuing this line of investigation, Zarina Akbary examined the ketoreductase activity of *S. cerevisiae* strain SC108, which was isolated from 45-million-year-old amber.[4] Her work forms the basis of the experiments described in this thesis.

The AKRs of SC108

Initial Studies of the SC108 AKRs

Akbary observed whole-cell ketoreductase activity in SC108, which catalyzed the reduction of ethyl pyruvate (EP), ethyl acetoacetate (EAA), and E4ClAA.[4] She then identified eight putative AKR gene sequences of interest from SC108, and she successfully cloned five of these sequences into *E. coli*. The recombinant *E. coli* cells reduced EP, EAA, and E4ClAA,

indicating that these AKRs contribute to the ketoreductase activity observed in SC108. Akbary also determined the chiral configuration of products from some of the cell extracts, confirming stereospecific reduction for all AKRs except AKR 169. Thus, these enzymes are potentially useful in biocatalysis.

AKR 163 and the Discovery of Substrate Inhibition

The researchers continuing Akbary's work sought to evaluate the kinetic behavior, substrate specificity, and biocatalytic applications of the SC108 AKRs. To do this, they isolated the SC108 AKRs from *E. coli* and purified them for *in vitro* analysis. Because AKR 163 exhibited the highest purity based on SDS-PAGE, it was selected for further study.[5]

AKR 163 shares 98.7% of its amino acid residues with the α-amide ketoreductase Ydl124w,[59] which has been used previously in biocatalysis. For example, a Ydl124w/GDH-coupled system displayed stereospecific reduction of E4ClAA to the statin side chain intermediate (*S*)-4-chloro-3-hydroxybutanoate in both *in vitro* and whole-cell conditions.[60] Ydl124w was also incorporated into an enantiospecific synthesis of the Taxol side chain, reducing an α-chloro-β-keto ester precursor via whole-cell biocatalysis with 98% ee.[61] Therefore, the study of AKR 163 has important industrial implications, as AKR 163 could be utilized in these syntheses or for novel applications depending on its substrate specificity.

Kinetic investigations of AKR 163 revealed surprising results. AKR 163 displayed typical Michaelis-Menten kinetics with EAA as well as ethyl propionyl acetate (EPA) and ethyl-2-methylacetoacetate (E2MAA), which are EAA analogues that contain alkyl groups (Figure 12a).[5] On the other hand, AKR 163 was found to exhibit substrate inhibition with EAA analogues that

contain an electron-withdrawing group proximal to the reduced carbonyl, such as E4ClAA, ethyl-2-fluoroacetoacetate (E2FAA), and EP (Figure 12b).[5]

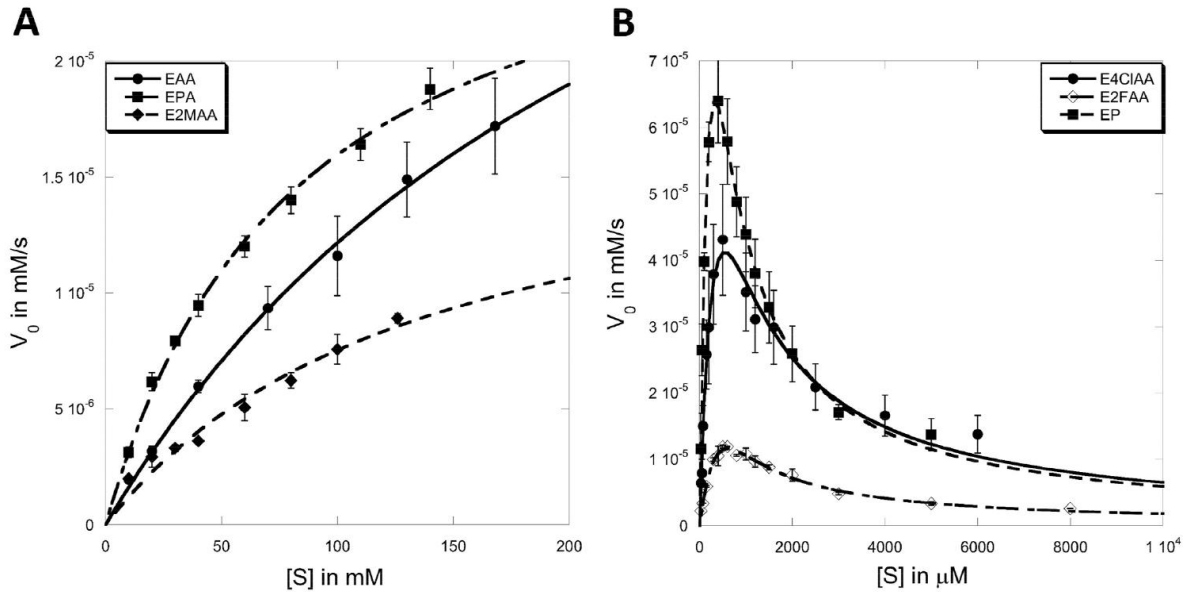

Figure 12. AKR 163 displays Michaelis-Menten behavior with EAA analogues containing alkyl groups (a) and substrate inhibition behavior with EAA analogues containing electron-withdrawing groups (b). Figure from Akbary et al.[5]

Substrate inhibition is rare among AKRs, and it has not been reported for Ydl124w. However, there are a few examples of substrate inhibition in AKRs, including AKR1B1[62], AKR1D1[63], and the *Bombyx mori* enzyme AKR2E4[64]. In the latter two cases, substrate inhibition was observed with a physiological substrate. In addition, a *Sporobolomyces salmonicolor* oxidoreductase from a different superfamily exhibited substrate inhibition with E4ClAA,[65] similar to AKR 163. Thus, studying substrate inhibition in AKR 163 can provide insight into inhibition in other AKRs and improve the scientific understanding of these enzymes.

Substrate inhibition is detrimental to biocatalysis, in which high substrate loadings are common.[66,67] In the case of AKR 163, low concentrations of electron-withdrawing substrates would be required in order to avoid inhibition, limiting the amount of product that can be produced. Therefore, it is critical to identify the causes of AKR 163's substrate inhibition as well as approaches to ameliorate this behavior. Understanding AKR 163's substrate inhibition is also useful for future biocatalytic approaches that aim to utilize AKRs exhibiting substrate inhibition.

After characterizing AKR 163's kinetic behavior, Akbary et al.[5] proposed a model for this enzyme's substrate inhibition that incorporates AKRs' ordered bi-bi kinetic mechanism (Figure 13). In this model, electron-withdrawing groups increase the electrophilicity of the carbonyl carbon by withdrawing electron density, making the carbonyl carbon more reactive and leading to a more rapid hydride transfer. This hypothesis is supported by the low K_M values for substrates containing electron-withdrawing groups compared to EAA analogues with alkyl groups. Assuming that the conformational change preceding $NADP^+$ release is the rate-limiting step, the more rapid hydride transfer leaves most of the enzyme in the form of the enzyme-$NADP^+$ complex. A second substrate molecule can then bind to the enzyme-$NADP^+$ complex, preventing $NADP^+$ dissociation and thus hindering catalysis.

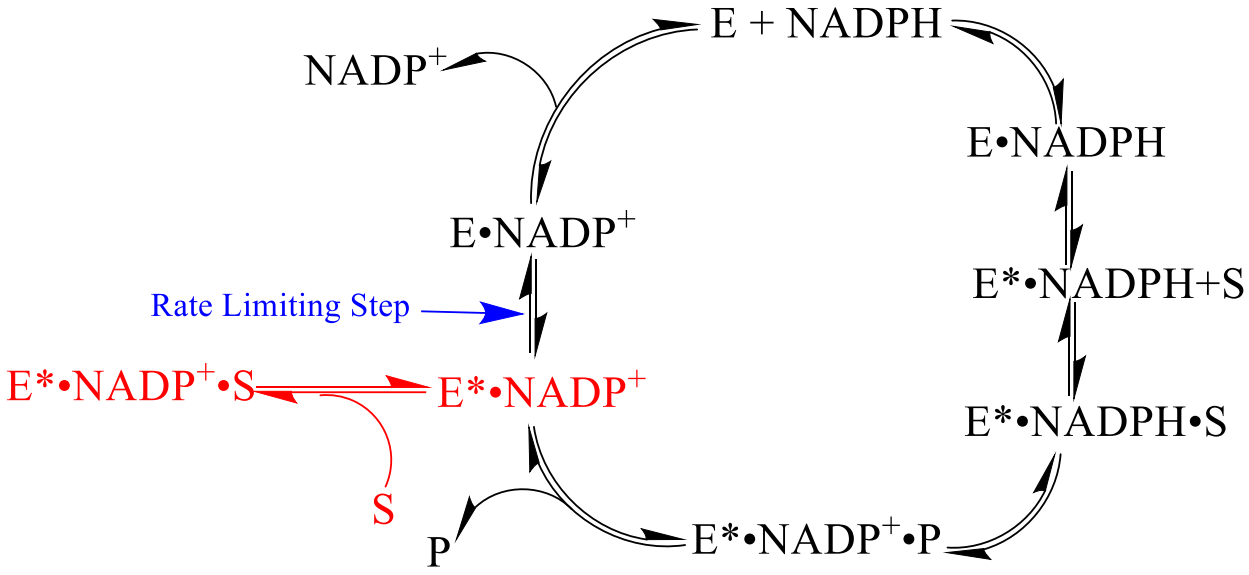

Figure 13. The mechanism of AKR 163's substrate inhibition proposed by Akbary et al.[5] Electron-withdrawing groups adjacent to the reactive carbonyl increase the rate of hydride transfer, leaving most of the enzyme in the form of the enzyme-$NADP^+$ complex. This allows a second substrate molecule to bind to the enzyme-$NADP^+$ complex and block $NADP^+$ dissociation. Figure from 2023 ACS Spring Meeting presentation by Akbary et al.[37]

While this proposed model is logical in the context of AKR 163's kinetic behavior, it has not been experimentally validated. Previous attempts to determine a precise mechanism for AKR 163's substrate inhibition have so far been unsuccessful. For example, enzyme-catalyzed dead-end adduct formation between the substrate and $NADP^+$, which was previously observed to facilitate substrate inhibition in aldose reductase,[68] did not appear to contribute to the substrate inhibition of AKR 163 (Goldman and Cassano, unpublished data). In addition, the glutathione-*S*-transferase (GST) tag fused to AKR 163 to facilitate its purification does not appear to cause substrate inhibition, as an AKR sample procured after removing the GST tag displayed the same substrate inhibition activity (Nazari and Cassano, unpublished data). One unexplored possibility is that substrate inhibition occurs solely due to the substrate binding to the enzyme-$NADP^+$ complex, so substrate inhibition with EAA analogues with electron-withdrawing groups may be

a general feature of AKRs. Therefore, attention has turned to purifying the other AKRs cloned from SC108 in order to compare their kinetic behavior to AKR 163.

AKR 308/Ara1: A Literature Review

AKR 308 became the next enzyme of interest due to its increased solubility compared to the other three cloned AKRs, allowing larger yields from enzyme preparations.[4] AKR 308 is nearly identical to the *S. cerevisiae* S288C enzyme D-arabinose dehydrogenase (Ara1), which reduces the toxic α,β-dicarbonyls 2,3-pentanedione (2,3-PD), diacetyl, and methylglyoxal with K_M values below 20 mM and k_{cat} values between 4 s^{-1} and 7 s^{-1}.[69] *ara1* knockout decreased the growth rate of yeast cells exposed to diacetyl,[69] and overexpression of *ara1* in *S. cerevisiae* led to a fivefold increase in whole-cell diacetyl reductase activity[70]. In addition to reducing diacetyl to acetoin, Ara1 can also reduce acetoin asymmetrically to 2,3-butanediol, with opposite stereoselectivity to butanediol dehydrogenase.[71,72]

Ara1 plays a protective role *in vivo* because it helps attenuate the stressful conditions generated by methylglyoxal, diacetyl, and 2,3-pentanedione. α,β-dicarbonyls are toxic because they react with amines via the Maillard reaction to form imines known as advanced glycation end products.[73] This imine formation inhibits enzymes, triggers DNA mutagenesis, and generates redox cycling, which increases reactive carbonyl species formation and induces oxidative stress.[73] The expression of *ara1* also increases about twofold in response to oxidative stress induced by H_2O_2, providing further evidence for Ara1's protective role.[74]

Ara1's wide substrate range and stereospecificity make AKR 308 well-suited for a variety of biocatalytic applications. For example, Ara1 reduces α,β-dicarbonyls to (*S)*-α-hydroxyketones

with greater than 96% ee.[72] Interestingly, Ara1 produces alcohols with the opposite stereochemistry from Ydl124w, which favors the *R* enantiomer.[72] Ara1 also reduces a wide variety of α- and β-keto esters[55] as well as α-chloro-β-keto esters,[56] demonstrating its versatility. Therefore, it is of interest to analyze AKR 308's kinetic behavior in order to determine the optimal conditions for biocatalysis and assess whether this enzyme exhibits substrate inhibition, which would pose potential problems for biocatalytic applications.

In addition to kinetic studies, an exploration of Ara1's structure allows for a deeper understanding of AKR 308's catalytic behavior, potential substrate inhibition, and utility in biocatalysis. Unlike the monomeric Ydl124w,[59] Ara1 exists as a homodimer composed of two 40 kDa subunits.[69] Several studies have also noted a 39 kDa band on SDS-PAGE,[72,75,76] which initially led to the conclusion that Ara1 was a heterodimer.[75] However, the smaller subunit was eventually identified as degraded Ara1, which has been observed in both *E. coli* and *S. cerevisiae*.[76] Ara1 was confirmed to be a homodimer based on the crystal structure of the apoenzyme (4IJC) and its complex with NADPH (4IJR).[77] The 4ijr crystal structure is shown in Figure 14. Subunit interactions occur between strand βA, strand βB, the loop Met-15-Tyr-24, and the loop Lys-91-Leu-96. Based on sequence alignment, Ara1's catalytic tetrad consists of Asp-66, Tyr-71, Lys-100, and His-131. Hu et al.[77] also docked diacetyl and 2,3-PD into the Ara1 active site. Ara1's published crystal structure provides mechanistic insights into AKR 308's kinetic behavior, and the dimeric nature of this enzyme creates a possibility for more unique behaviors like cooperative binding.

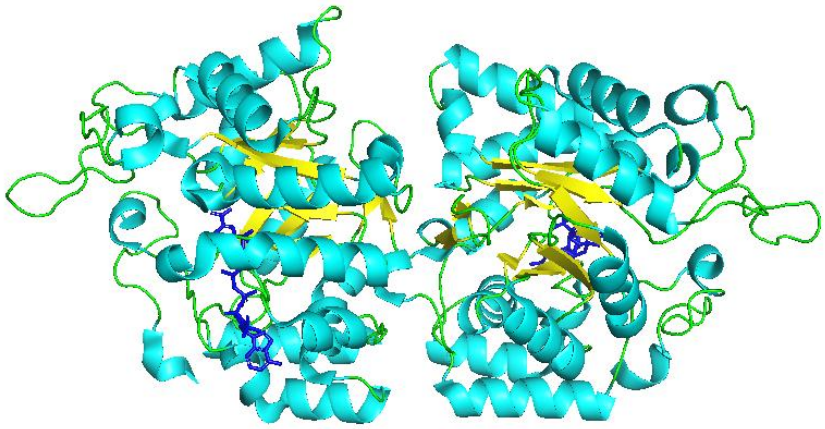

Figure 14. Crystal structure of Ara1 in complex with NADPH. α helices are shown in light blue, β sheets are shown in yellow, loops are shown in green, and NADPH is shown in dark blue. This crystal structure was obtained from RCSB Protein Data Bank with identifier 4IJR, and it was solved by Hu et al.[77]

Present Study

This thesis describes a broad investigation of AKR 308's kinetic behavior, substrate specificity, substrate inhibition patterns, and structural properties in relation to AKR 163. GST-tagged AKR 308 was isolated from *E. coli* and purified via glutathione affinity chromatography. Then, AKR 308's properties were examined in a series of experiments within three categories: kinetics, fluorescence, and substrate docking. Kinetic experiments were performed to establish AKR 308's substrate specificity in comparison to AKR 163 and to screen for substrate inhibition behavior. Fluorescence emission spectroscopy experiments were conducted to determine K_D values for cofactor and substrate binding, which more accurately reflect binding affinity compared to K_M values. Computational substrate docking with the Ara1 crystal structure was performed to predict catalytic and nonproductive binding poses of substrates, identify allosteric

sites that could contribute to AKR 308's cooperativity, and assess potential structural mechanisms of substrate inhibition.

AKR 308 was found to exhibit different substrate inhibition behavior compared to AKR 163. For AKR 308, substrate inhibition was not general across substrates with electron-withdrawing groups. However, AKR 308 did exhibit substrate inhibition and cooperativity with the substrate ethyl pyruvate. Fluorescence emission spectroscopy experiments revealed that AKR 308 has a slightly lower binding affinity for $NADP^+$ compared to AKR 163. Substrate docking studies predicted nonproductive poses of EP in the active site that were more energetically favorable compared to the catalytic pose, which was not the case for E4ClAA and 2,3-PD. Taken together, these findings suggest that AKR 308's substrate inhibition may be mediated by the formation of nonproductive substrate poses rather than substrate binding to the enzyme-$NADP^+$ complex.

Methods

Purification

Isolation and purification of AKR 308 were performed as described in Akbary et al.[5] Briefly, AKR 308 was overexpressed via IPTG induction in *E. coli* containing a fused AKR 308-GST plasmid construct. Cultures were grown at either 28 °C or 30 °C with similar yield. AKR 308 was purified via glutathione affinity chromatography after lysis of the bacterial pellet. The concentration of each affinity chromatography fraction was assessed using a Bradford assay, and the activity of each affinity chromatography fraction was determined based on the reduction of 2 mM E4ClAA. After removal of glutathione, the concentration of AKR 308 was determined based

on absorbance at 280 nm and an extinction coefficient of 87210 $Abs \cdot M^{-1} \cdot cm^{-1}$ calculated from the number of tryptophan and tyrosine residues in AKR 308's sequence.[78]

SDS-PAGE was performed to confirm purification of AKR 308. Samples contained either 10 µg of lysate; 5 µg of column flowthrough, the first wash buffer fraction (WB1), or the second wash buffer fraction (WB2); or 2 µg of the second eluting buffer fraction (EB2), the third eluting buffer fraction (EB3), concentrated AKR 308, or concentrated AKR 163. These samples were combined with SDS-denaturing buffer (0.125 M Tris-HCl, pH 6.8, 4% SDS, 20% glycerol, 10% β-mercaptoethanol, 0.002% bromophenol blue), heated to 95 °C for 5 minutes to ensure denaturation, and loaded into a 12% Bis-Tris PAGE plate in Tris-glycine buffer (0.025 M Tris, pH 8.3, 0.192 M glycine, 0.1% SDS) along with a Precision Plus Protein Dual Color Standard ladder. The gel was run at 200 V for approximately 30 minutes, stained in Coomassie Brilliant Blue R solution, and destained in a 40% methanol, 7% acetic acid solution.

Kinetics

Kinetic experiments with AKR 308 were performed as described in Akbary et al.[5] with some modifications. Reactions were conducted in 25 mM Tris buffer (pH 8) using 100 µM NADPH. The structures and concentration ranges of the substrates used in kinetic experiments are shown in Table 1. An AKR 308 concentration of 87 nM was used for the majority of trials, and an AKR 308 concentration of 43.5 nM was used for EP and certain trials of E2MAA and E2EAA to conserve enzyme. Kinetic data for the AKR 163-catalyzed reduction of EAA, E4ClAA, E2FAA, and EP was obtained from Akbary et al.[5], and the present study explored the AKR 163-catalyzed reduction of 2,3-PD, 2,4-PD, and E2EAA. In most cases, the concentration

of AKR 163 was 84 nM. The AKR 163 concentration was doubled for 2,4-PD and E2EAA. Due to solubility concerns with 2,3-PD, the maximum DMSO concentration for reactions with this substrate was increased to 3%. For all other experiments, the maximum DMSO concentration was maintained at 2%. Reactions were monitored by a Cary60 UV-Vis spectrophotometer based on the decrease in absorbance at 340 nm as NADPH is oxidized to $NADP^+$. The extinction coefficient for NADPH is 6.22 $Abs \cdot mM^{-1} \cdot s^{-1}$. Absorbance data was taken every 15 seconds for a total time of 3 minutes with an average scan time of 1 second.

Table 1. Names, abbreviations, structures, and concentration ranges of substrates used in kinetic experiments.

Substrate	Structure	Concentration Range (mM)
Ethyl acetoacetate (EAA)	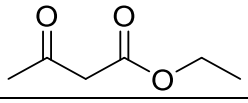	10-158
Ethyl 4-chloroacetoacetate (E4ClAA)	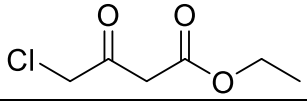	1-35
Ethyl 2-fluoroacetoacetate (E2FAA)	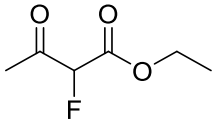	1-158
Ethyl pyruvate (EP)	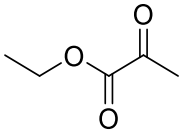	1-30
2,3-pentanedione (2,3-PD)	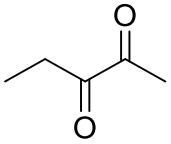	0.25-15
2,4-pentanedione (2,4-PD)	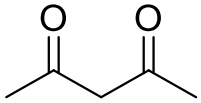	1-158
1,1,1-trifluoro-2,4-pentanedione (TF-2,4-PD)	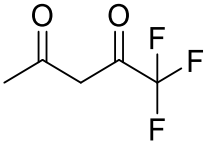	1-164
Ethyl-2-methylacetoacetate (E2MAA)	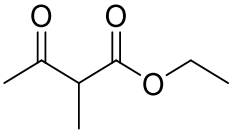	10-126
Ethyl-2-ethylacetoacetate (E2EAA)	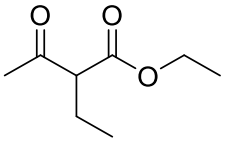	10-124

Data analysis was conducted using the general procedure outlined in Akbary et al.[5] Reaction rates in Abs/s were calculated in Excel and converted to velocities in mM/s. Velocities were plotted in Kaleidagraph and fit to either Equation 1, 2, 3, or 4. For substrates displaying Michaelis-Menten kinetics, velocity data was fit to Equation 1:

$$v_0 = \frac{V_{max}[S]}{K_M+[S]} \qquad (1)$$

For substrates displaying substrate inhibition, velocity data was fit to Equation 2:

$$v_0 = \frac{V_{\max}[S]}{K_M+[S]+\frac{[S]^2}{K_i}} \qquad (2)$$

For substrates displaying cooperative binding, velocity data was fit to the Hill equation (Equation 3):

$$v_0 = V_{\max}\left(\frac{[S]^n}{(K_{0.5})^n+[S]^n}\right) \qquad (3)$$

For substrates displaying both cooperative binding and inhibition, velocity data was fit to a model combining the Hill equation and substrate inhibition equation (Equation 4):

$$v_0 = \frac{V_{max}[S]^n}{(K_{0.5})^n+[S]^n+\frac{[S]^{(n+1)}}{K_i}} \qquad (4)$$

V_{max} represents the reaction velocity at enzyme saturation, K_M represents the Michaelis constant, K_i represents the inhibitory constant, $K_{0.5}$ represents the substrate concentration at which 50% of the enzyme binding sites are occupied, and n represents the Hill coefficient.

Fluorescence

Fluorescence titrations of AKR 308 with either $NADP^+$ or substrate were conducted to determine K_D values. Fluorescence measurements were taken on a FluoroMax 3 fluorimeter, with excitation occurring at 290 nm and emission spectra taken from 310 nm to 450 nm. The solution used for fluorescence measurements contained 25 mM Tris buffer (pH 8) and 0.5 μM AKR 308 at a total volume of 2.5 mL. Before taking fluorescence measurements with enzyme, the fluorimeter was first blanked on an equivalent solution with purification buffer (125 mM Tris, 150 mM NaCl, pH 8) replacing the volume of AKR 308. To determine the K_D value for cofactor, $NADP^+$ was added incrementally to produce a range of concentrations from 0.1 μM to 3.5 μM. The total volume of $NADP^+$ added did not exceed 1% of the total solution volume. When determining K_D values for substrates, 15 μM $NADP^+$ was added beforehand to saturate the enzyme and ensure that the expected decrease in fluorescence occurred. Substrate was then added incrementally.

The fluorescence data were analyzed using Excel. Fluorescence values for the blank solution at each wavelength were subtracted from the other scans, and the fluorescence values were plotted as a function of wavelength for each $NADP^+$ or substrate concentration. To determine ΔF values for each $NADP^+$ concentration, the fluorescence of AKR 308 alone at 341 nm (generally corresponding to the maximum fluorescence) was subtracted from the fluorescence of the AKR 308-$NADP^+$ complex at 341 nm. ΔF values for substrates were determined using a similar approach, except that the fluorescence of the AKR 308-$NADP^+$ complex was used for normalization instead of AKR 308 alone.

ΔF values were plotted against $NADP^+$ or substrate concentration in Kaleidagraph in order to calculate K_D values. For substrates, K_D values were calculated using Equation 5:

$$\Delta F = \frac{\Delta F_{max}[S]}{K_D + [S]} \quad (5)$$

For $NADP^+$, the Michaelis-Menten assumption that the substrate concentration is much greater than the enzyme concentration is not true, so Equation 5 could not be used. Instead, Equation 6 was derived from the definition of K_D:

$$\Delta F = -\Delta F_{max}([E] + [NADP^+] + K_D - \sqrt{([E] + [NADP^+] + K_D)^2 + 4[E][NADP^+]}) \quad (6)$$

The absorbance of EP, EAA, E4ClAA, and 2,4-PD was measured at 290 nm using a Cary60 UV-vis spectrophotometer in order to assess confounding substrate absorbance effects at the excitation wavelength. Absorbance measurements were taken at the maximum substrate concentration used in fluorescence experiments. The transmittance of E4ClAA at 290 nm was measured as well in an attempt to correct the fluorescence values and account for substrate absorbance.

Substrate Docking

Substrate docking was conducted using Cresset Flare software[79] and the Normal mode of the LeadFinder algorithm.[80] The docking process is based on a genetic algorithm in which an initial pool of optimized poses is generated, the population is divided into geometry-based clusters, and the most ideal poses in each cluster are selected for further optimization.[81] The LeadFinder algorithm generates three scores for each pose: the Rank Score, the dG Score, and the virtual screening score (VSscore). Each score is based on energy contributions that include

van der Waals interactions, metal interactions, electrostatic interactions, ligand desolvation, hydrogen bonding, nonpolar solvation due to hydrophobic contacts, ligand internal energy and entropic losses, and torsion energy. Different weights are applied to the energy contributions for each score. The Rank Score reflects the accuracy of the docked pose, where higher scores correspond to poses that are most likely to be observed experimentally. The dG Score reflects the free energy of ligand binding in kcal/mol. Because the VSscore is intended for virtual screening of large compound libraries, it was not examined in this study.

Docking was conducted with 4IJR, the AKR 308-$NADP^+$ crystal structure determined by Hu et al.[77] The "active site" was defined using the substrate binding residues identified by Hu et al.: Y71, H131, A41, A70, W102, W132, K150, T151, Y240, H246, I321, E323, and F325. The energy grid surrounding the active site was selected so that steric clashes with NADPH would be minimized and the substrate would be positioned near Y71, the catalytic tyrosine.

All substrates tested in kinetic experiments were docked into the active site. Each substrate yielded five to ten poses. In some poses, the substrate overlapped with NADPH. These poses were immediately rejected. "Catalytic" poses were chosen based on adherence to the following criteria: 1) orientation of the reactive carbonyl toward Y71, 2) a hydrogen bonding distance between the reactive carbonyl and NADPH that is less than or equal to 4.1 Å, and 3) a hydrogen bonding distance between the reactive carbonyl and Y71 that is less than or equal to 4.1 Å.

In addition to Rank Scores and dG Scores from the LeadFinder algorithm, findings from other Flare features were recorded for each pose. Flare's Interaction Map feature was used to

identify residues that interact with the substrate via hydrogen bonding and van der Waals forces as well as steric clashes. Distances to hydrogen bond donors were determined using Flare's Measurement tool. Hydrogen bond distances from the reactive carbonyl to Y71 and NADPH were also measured for catalytic poses.

Potential allosteric sites were identified using the Ensemble mode of the PASSer algorithm.[82] Pockets with the three highest allostery probabilities were selected for docking, and the pocket residues were designated in Flare. EP, E4ClAA, and 2,3-PD were docked into the allosteric sites using the LeadFinder algorithm, with the energy grids defined by the pocket residues. The poses with the five highest Rank Scores were selected for further analysis as described above (except for evaluating catalytic potential).

Results

AKR 308 was overexpressed in *E. coli* and purified via glutathione affinity chromatography. Kinetic behavior and substrate specificity were assessed using UV-vis spectroscopy, and cofactor and substrate binding were assessed using fluorescence emission spectroscopy. Computational substrate docking was performed to predict substrate binding poses, identify potential structural explanations for substrate specificity and substrate inhibition, and examine potential allosteric sites.

Purification

AKR 308 was successfully purified by glutathione affinity chromatography. Specific activity data for a sample purification is shown in Figure 15. The specific activities of EB2 and EB3 were approximately two times greater than the specific activity of the lysate, demonstrating

elution of pure AKR 308 from the column. Unwanted proteins were removed in WB1 and WB2, which have much lower specific activities than the lysate and elution buffer fractions.

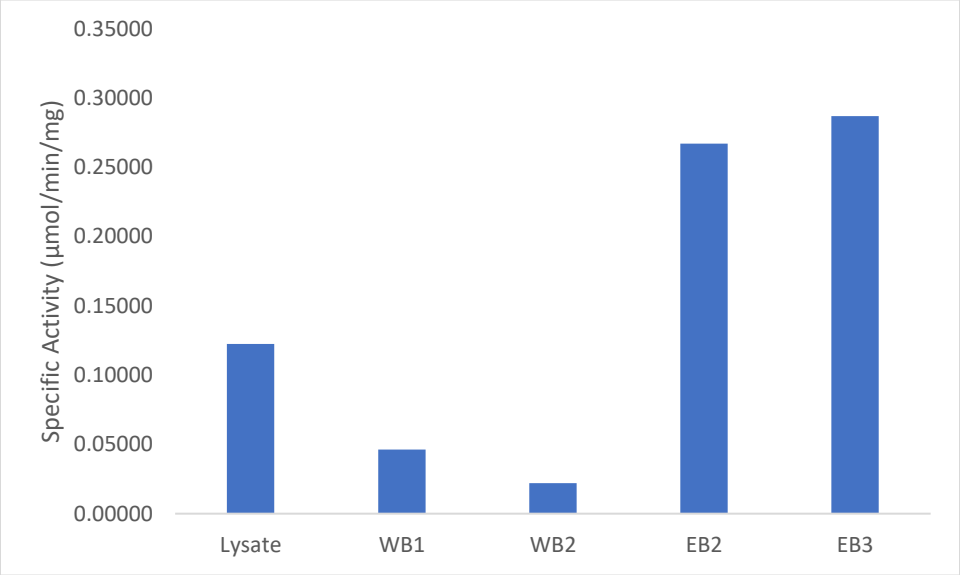

Figure 15. Specific activity of the lysate, wash buffer fraction 1 (WB1), wash buffer fraction 2 (WB2), elution buffer fraction 2 (EB2), and elution buffer fraction 3 (EB3).

SDS-PAGE confirmed that the protein obtained in the elution buffer fractions is AKR 308 (Figure 16). While the lysate, flowthrough, WB1, and WB2 contain multiple bands, EB2 and EB3 contain a single band between 50 and 75 kDa in weight, suggesting that AKR 308 is present in these fractions without any contaminating proteins. Concentrated AKR 308 and AKR 163 produced darker bands than what was observed for EB2 and EB3. Both concentrated AKR 308 and concentrated AKR 163 produced a band between 50 and 75 kDa in weight. The band that AKR 308 produced in this range is slightly higher than the band for AKR 163, indicating that AKR 308 has a greater molecular weight than AKR 163. These observations are consistent with GST-tagged AKR 308's molecular weight of 68 kDa and GST-tagged AKR 163's molecular weight of 64 kDa. Both concentrated AKR 308 and concentrated AKR 163 also produced a band

between 25 kDa and 37 kDa in size and a band between 37 kDa and 50 kDa in size. The bands that AKR 308 produced in these regions were darker than for AKR 163. However, these contaminating bands are fainter than the full-length AKR 308 and AKR 163 proteins, indicating satisfactory purification.

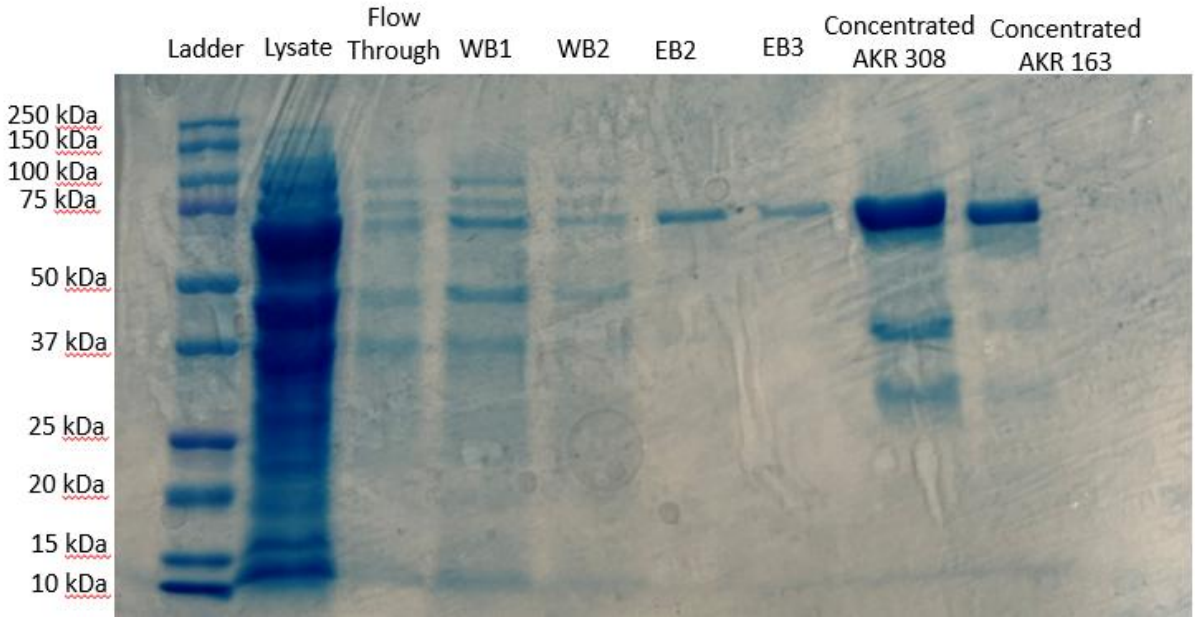

Figure 16. SDS-PAGE performed on purification fractions. The ladder was Precision Plus Protein Dual Color Standard. The lysate was overloaded with 10 µg of protein due to concerns about underestimating the concentration in the Bradford assay. The flowthrough, wash buffer fraction 1 (WB1), and wash buffer fraction 2 (WB2) contained 5 µg of protein. Elution buffer fraction 2 (EB2), elution buffer fraction 3 (EB3), concentrated AKR 308, and concentrated AKR 163 contained 2 µg of protein. Concentrated AKR 308 and concentrated AKR 163 represent samples taken after the removal of glutathione.

Kinetics

The kinetic data for AKR 308 is summarized in Table 2 and compared to kinetic parameters for AKR 163. Kinetic plots are presented below, and kinetic data is discussed in turn from the plots.

Table 2. Kinetic parameters for AKR 163-catalyzed and AKR 308-catalyzed reduction of various substrates.

	AKR 163				AKR 308		
	k_{cat} (s^{-1})	K_M (mM)	k_{cat}/K_M (s^{-1} mM^{-1})	K_i (mM)	k_{cat} (s^{-1})	K_M (mM)	k_{cat}/K_M (s^{-1} mM^{-1})
EAA	0.52±0.07[a]	260±50[a]	0.002[a]	N/A	0.8±0.4[a]	800±300[a]	0.001[a]
E2MAA	0.22±0.05[a]	140±50[a]	0.0015[a]	N/A	Inconclusive	Inconclusive	Inconclusive
E2EAA	N.R.	N.R.	N.R.	N.R.	4.5±0.5[a]	170±30[a]	0.026[a]
E4ClAA	1.8±0.4[b]	0.5±0.2[b]	3.6[b]	0.6±0.2[b]	2.4±0.2[a]	10.±2[a]	0.24[a]
E2FAA	0.6±0.1[b]	0.9±0.3[b]	0.7[b]	0.4±0.1[b]	1.8±0.4[a]	50±20[a]	0.04[a]
EP	2.5±0.3[b]	0.38±0.06[b]	6.6[b]	0.29±0.05[b]	1.5±0.2[c]	6.7±0.4[c]	0.22[c]
2,3-PD	0.99±0.08[a]	4.4±0.9[a]	0.23[a]	Inconclusive	7±2[a]	80±30[a]	0.08[a]
2,4-PD	N.R.	N.R.	N.R.	N.R.	N.R.	N.R.	N.R.
TF24PD	N.D.	N.D.	N.D.	N.D.	N.R.	N.R.	N.R.

N.R., no reaction; N.D., not determined.
[a] Determined from Equation 1
[b] Determined from Equation 2
[c] Determined from Equation 3

Kinetic Analysis of Substrates Without Electron-Withdrawing Groups

Both AKR 308 and AKR 163 followed Michaelis-Menten kinetics with respect to EAA (Figure 17). AKR 308 displays a slightly higher k_{cat} value for EAA, but its K_M value for this substrate is three times higher than that of AKR 163 (Table 2). As a result, AKR 308-catalyzed reduction of EAA is about half as efficient as AKR 163-catalyzed reduction of this substrate.

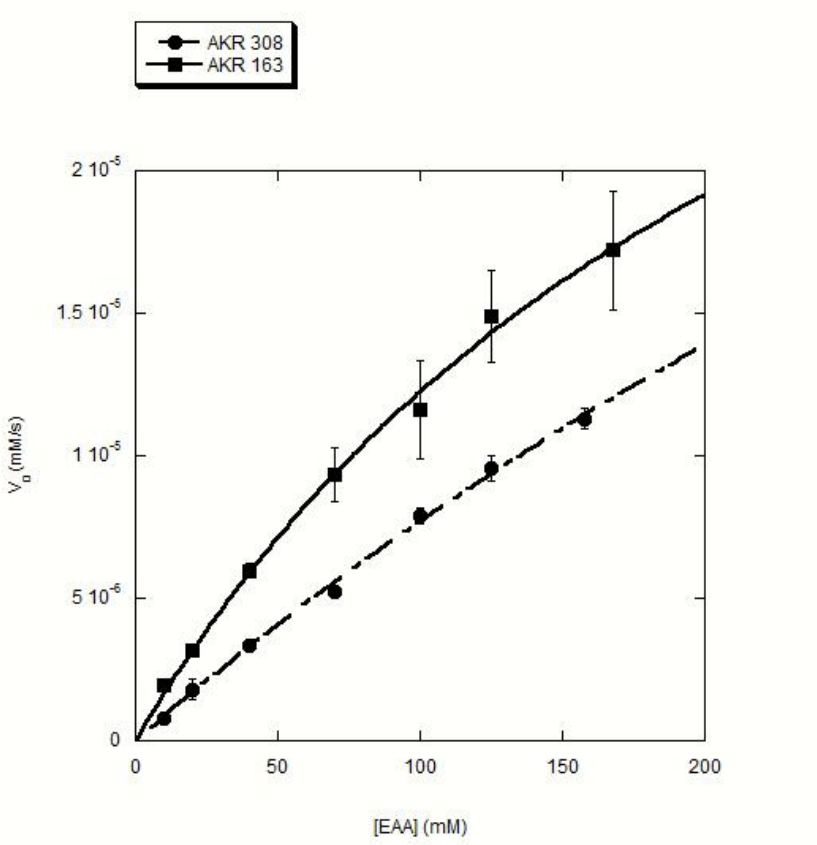

Figure 17. Comparison of the AKR 163-catalyzed and AKR 308-catalyzed reduction of EAA. AKR 308 is represented by circles, and AKR 163 is represented by squares. All velocities represent the average of three trials, and error bars represent the standard error. EAA follows Michaelis-Menten kinetics for both enzymes, so both plots are fit to Equation 1. Data for AKR 163 was obtained from Akbary et al.[5] AKR 308's and AKR 163's kinetic parameters for EAA are shown in Table 2.

One question of interest with regard to substrates without electron-withdrawing groups is the impact of steric bulk. E2MAA and E2EAA were chosen to investigate this question. E2MAA and E2EAA consist of EAA with methyl and ethyl groups attached to the carbon in the 2-position, respectively. Akbary et al.[5] previously found that AKR 163 exhibits a lower k_{cat}, K_M, and efficiency with E2MAA compared to EAA, indicating that AKR 163's catalytic power and efficiency decrease with increasing steric bulk, but its substrate binding affinity increases. The

AKR 308-catalyzed reduction of E2MAA was examined to determine if AKR 308 exhibits a similar trend. To further investigate the effect of steric bulk, AKR 163's and AKR 308's activities with E2EAA were examined as well.

AKR 308 displayed markedly higher reaction velocities with E2MAA compared to AKR 163 (Figure 18). Because the Michaelis-Menten fit was too linear over the concentration range tested, kinetic parameters could not be calculated for AKR 308. However, one can infer from Figure 18 that AKR 308 displays a higher k_{cat} for E2MAA compared to AKR 163.

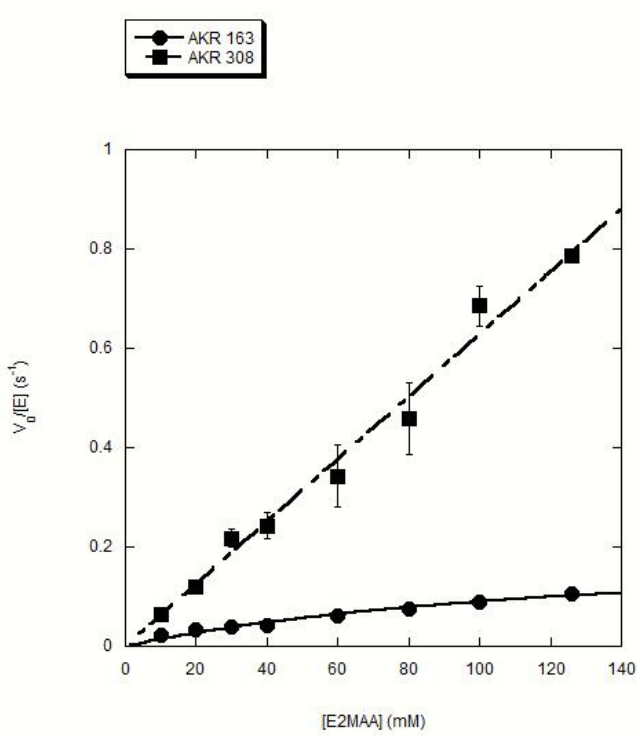

Figure 18. Comparison of the AKR 163-catalyzed and AKR 308-catalyzed reduction of E2MAA. AKR 308 is represented by squares, and AKR 163 is represented by circles. All velocities represent the average of three trials, and error bars represent the standard error. E2MAA follows Michaelis-Menten kinetics for both enzymes, so both plots are fit to Equation 1. Data for AKR 163 was obtained from Akbary et al.[5] AKR 308's and AKR 163's kinetic parameters for E2MAA are shown in Table 2.

AKR 308's reaction velocity with E2EAA is even greater than its reaction velocity with E2MAA at identical substrate concentrations (Figure 19). At about 125 mM, AKR 308's reaction velocity with E2EAA is more than twice its reaction velocity with E2MAA. AKR 308-catalyzed E2EAA reduction has a k_{cat} value that is more than five times larger than that of EAA, a K_M value that is more than four times smaller than that of EAA, and an efficiency value that is more than twice as large than that of EAA (Table 2). Thus, AKR 308 has greater catalytic power and substrate binding affinity with E2EAA, leading to a greater catalytic efficiency compared to EAA. Overall, AKR 308's activity with substrates without electron-withdrawing groups appears to improve with increased steric bulk.

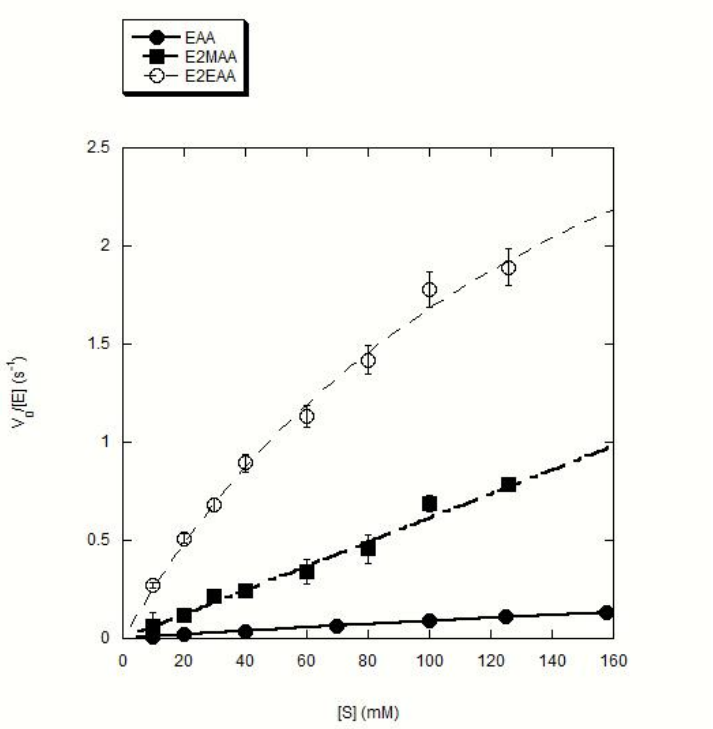

Figure 19. Comparison of the AKR 308-catalyzed reduction of EAA, E2MAA, and E2EAA. EAA is represented by closed circles, E2MAA is represented by squares, and E2EAA is represented by open circles. All velocities represent the average of three trials, and error bars represent standard error. EAA, E2MAA, and E2EAA follow Michaelis-Menten kinetics for AKR 308, so all of these plots are fit to Equation 1. AKR 308's and AKR 163's kinetic parameters for these substrates are shown in Table 2.

AKR 163 did not appear to react with E2EAA (data not shown). V_0/[E] values did not exceed 0.14 s^{-1}, and reaction velocities did not increase in a concentration-dependent manner. This is consistent with a trend where AKR 163's catalytic power and efficiency decrease with increasing steric bulk, which is opposite to the trend exhibited by AKR 308.

Kinetic Analysis of Substrates with Electron-Withdrawing Groups

AKR 308's kinetic behavior with respect to E4ClAA (Figure 20) and E2FAA (Figure 21) is strikingly different from AKR 163. While E4ClAA and E2FAA exhibited substrate inhibition

with AKR 163, these substrates followed Michaelis-Menten kinetics with AKR 308. Similar to EAA, AKR 308 displays higher k_{cat} and K_M values and lower efficiency values for these substrates compared to AKR 163 (Table 2). Interestingly, AKR 308 displays markedly different binding affinities for E4ClAA and E2FAA. AKR 308's K_M value for E2FAA is fivefold higher than its K_M value for E4ClAA (Table 2). In contrast, AKR 163's K_M value for E2FAA is only two times higher than its K_M value for E4ClAA.

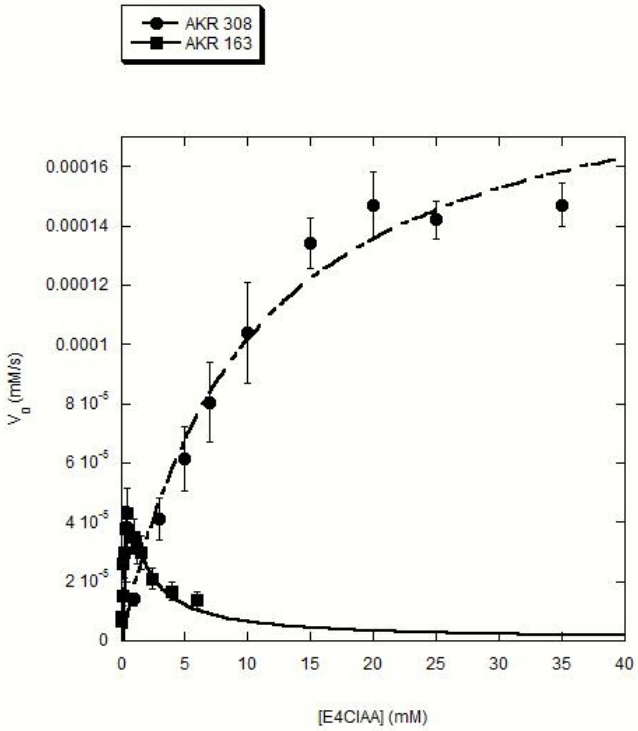

Figure 20. Comparison of the AKR 163-catalyzed and AKR 308-catalyzed reduction of E4ClAA. AKR 308 is represented by circles, and AKR 163 is represented by squares. Velocities for AKR 163 represent the average of six trials. For AKR 308, the velocity for 35 mM E4ClAA represents the average of two trials, and all other velocities represent the average of three trials. Error bars represent standard error. E4ClAA exhibits substrate inhibition for AKR 163, so this plot is fit to Equation 2. E4ClAA follows Michaelis-Menten kinetics for AKR 308, so this plot is fit to Equation 1. Data for AKR 163 was obtained from Akbary et al.[5] AKR 308's and AKR 163's kinetic parameters for E4ClAA are shown in Table 2.

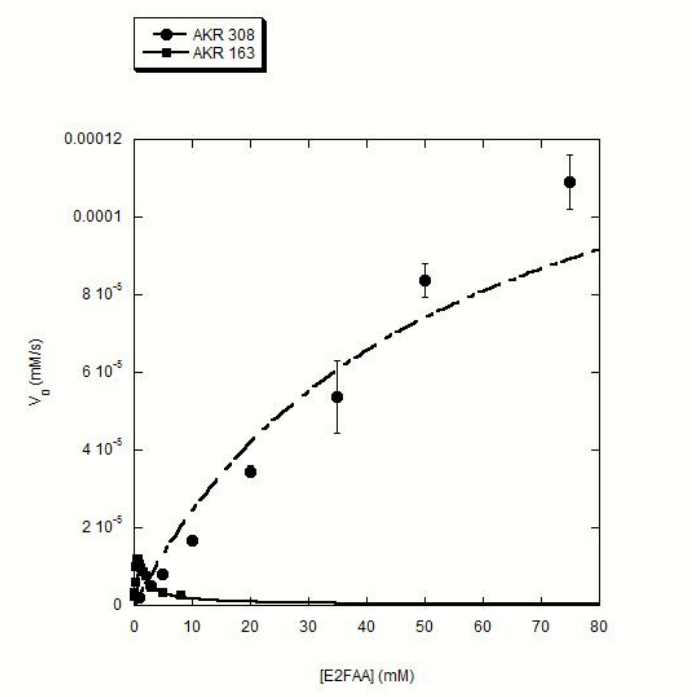

Figure 21. Comparison of the AKR 163-catalyzed and AKR 308-catalyzed reduction of E2FAA. AKR 308 is represented by circles, and AKR 163 is represented by squares. AKR 308's reaction velocity with 158 mM E2FAA was included in the curve fit but is not shown in the graph. Velocities for AKR 163 represent the average of two trials. For AKR 308, the velocities for 1 mM E2FAA and 158 mM E2FAA represent the average of two trials, and the velocity for 75 mM E2FAA represents the average of four trials. All other velocities for E2FAA represent the average of three trials. Error bars represent range for AKR 163 and standard error for AKR 308. E2FAA exhibits substrate inhibition for AKR 163, so this plot is fit to Equation 2. E2FAA follows Michaelis-Menten kinetics for AKR 308, so this plot is fit to Equation 1. Data for AKR 163 was obtained from Akbary et al.[5] AKR 308's and AKR 163's kinetic parameters for E2FAA are shown in Table 2.

EP displayed more unique kinetic behaviors with AKR 308 compared to EAA, E4ClAA, and E2FAA. In contrast to the other electron-withdrawing substrates E4ClAA and E2FAA, EP exhibited substrate inhibition with AKR 308 as well as AKR 163 (Figure 22). Surprisingly, EP also exhibited cooperative binding with AKR 308. Cooperative binding is evident from Figure 22; for AKR 308, the initial increase in velocity is sigmoidal, whereas for AKR 163, the initial increase in velocity is linear. While Equation 4 produced a curve that fit the velocities for EP, the

kinetic parameters could not be determined due to this equation's complexity. Therefore, to estimate k_{cat}, K_M, and the Hill coefficient, the velocities for EP concentrations below 10 mM were fit to Equation 3, which excludes substrate inhibition (Figure 23). As a result of this procedure, the K_i for EP could not be determined. The Hill coefficient for EP was estimated as 3.9±0.6.

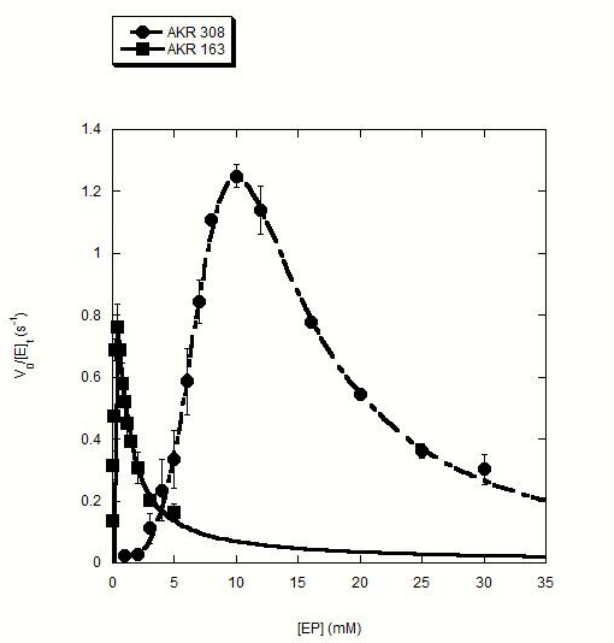

Figure 22. Comparison of the AKR 163-catalyzed and AKR 308-catalyzed reduction of EP. AKR 308 is represented by circles, and AKR 163 is represented by squares. All velocities represent the average of three trials, and error bars represent standard error. EP exhibits substrate inhibition for AKR 163, so this plot is fit to Equation 2. EP exhibits both cooperative binding and substrate inhibition for AKR 308, so this plot is fit to Equation 4. Data for AKR 163 was obtained from Akbary et al.[5] AKR 163's kinetic parameters for EP are shown in Table 2. The kinetic parameters for AKR 308-catalyzed EP reduction could not be determined using this model.

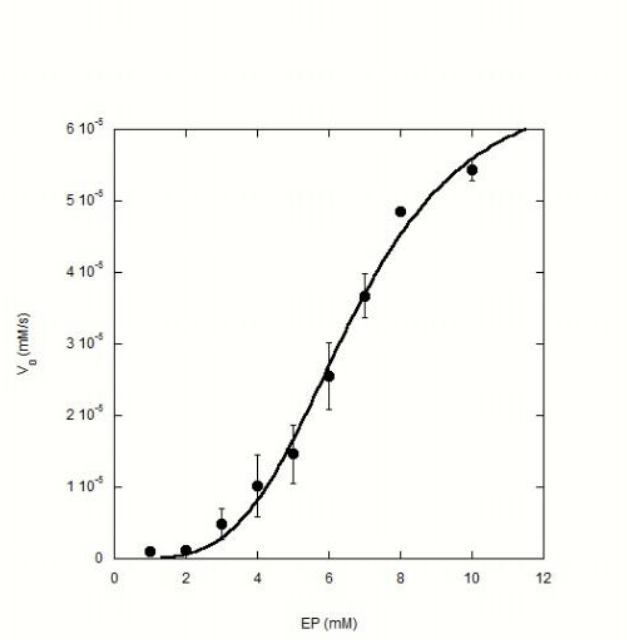

Figure 23. AKR 308-catalyzed reduction of EP fit to Equation 3. Concentrations above 10 mM EP are excluded. Each velocity represents the average of three trials, and error bars represent standard error. AKR 308's kinetic parameters for EP are shown in Table 2.

The kinetic parameters of AKR 308-catalyzed EP reduction differ from other AKR 308 substrates as well as AKR 163-catalyzed EP reduction. As is the case for EAA, E4ClAA, and E2FAA, AKR 308 displays a higher K_M and lower efficiency for EP compared to AKR 163 (Table 2). However, unlike the other substrates, AKR 308 displays a lower k_{cat} for EP compared to AKR 163. Substrate inhibition of AKR 163 by EP occurs at a much lower EP concentration compared to AKR 308. To illustrate, the sigmoidal portion of AKR 308's EP velocity plot begins to increase exponentially at an EP concentration at which AKR 163 is almost completely inhibited (Figure 22). AKR 308 also displays lower K_M and k_{cat} values for EP than for E4ClAA (Table 2). However, these substrates have similar efficiency values (Table 2).

Because E4ClAA and E2FAA did not induce substrate inhibition or cooperativity in AKR 308, it was already clear that these phenomena were not functions of electron-withdrawing groups. However, it was plausible that these behaviors were functions of 2,3-dicarbonyls, a category that describes EP and Ara1's physiological substrate 2,3-PD. Thus, AKR 308's kinetic behavior with 2,3-PD was examined. In contrast to EP, 2,3-PD appears to exhibit Michaelis-Menten kinetics with AKR 308 (Figure 24). 2,3-PD exhibited a higher k_{cat} and K_M compared to EP, and reduction of EP was more efficient than reduction of 2,3-PD (Table 2). Because the background absorbance of 20 mM 2,3-PD exceeded 2, the highest 2,3-PD concentration was limited to 15 mM, which meant that saturation of AKR 308 with 2,3-PD could not be achieved and a Michaelis-Menten model could not be confirmed. However, based on the current data, substrate inhibition of AKR 308 with 2,3-PD does not appear to occur.

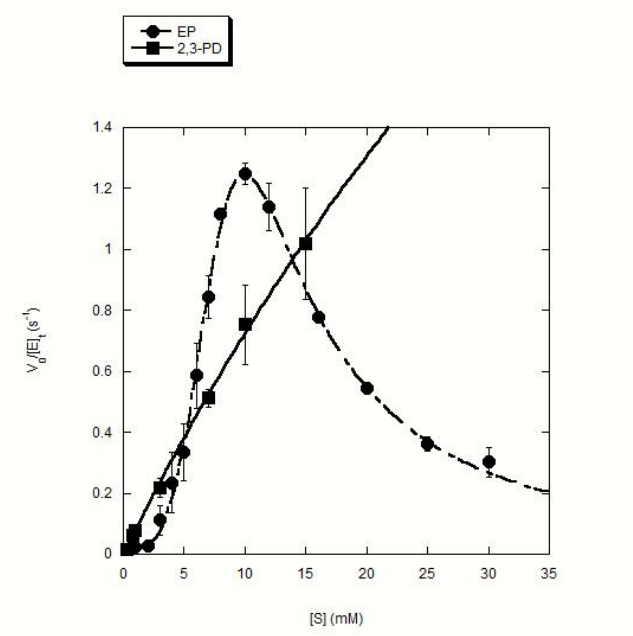

Figure 24. Comparison of the AKR 308-catalyzed reduction of EP and 2,3-PD. EP is represented by circles, and 2,3-PD is represented by squares. All velocities represent the average of three trials, and error bars represent standard error. 2,3-PD follows Michaelis-Menten kinetics, so this plot is fit to Equation 1. EP exhibits both cooperative binding and substrate inhibition, so this plot is fit to Equation 4. AKR 308's kinetic parameters for EP and 2,3-PD are shown in Table 2. Kinetic parameters for EP were calculated from Equation 3.

The AKR 163-catalyzed reduction of 2,3-PD was also investigated for the first time to determine if electron withdrawing group-dependent inhibition of this enzyme also applies to 2,3-dicarbonyls. AKR 163's behavior with 2,3-PD appears to be Michaelis-Menten. However, it is important to note that a decrease in velocity was observed between 12 mM and 15 mM 2,3-PD, suggesting that AKR 163 may exhibit substrate inhibition with 2,3-PD. Thus, the velocities for AKR 163-catalyzed 2,3-PD reduction can be fit to either a Michaelis-Menten model or a substrate inhibition model (Figure 25). In order to definitively exclude the possibility of substrate inhibition, one would need to examine 2,3-PD concentrations above 15 mM, which was not

undertaken in this study due to the high background absorbance rates. A Michaelis-Menten model was assumed for the purpose of comparison with AKR 308 (Figure 26). AKR 163 exhibits a higher k_{cat}, a lower K_M, and a higher efficiency for 2,3-PD compared to AKR 308 (Table 2). Compared to other electron-withdrawing substrates, the AKR 163-catalyzed reduction of 2,3-PD exhibits a higher K_M, a lower efficiency, and a similar k_{cat} (Table 2). Compared to the AKR 163-catalyzed reduction of EAA, 2,3-PD reduction exhibits a higher k_{cat}, a lower K_M, and a greater efficiency (Table 2).

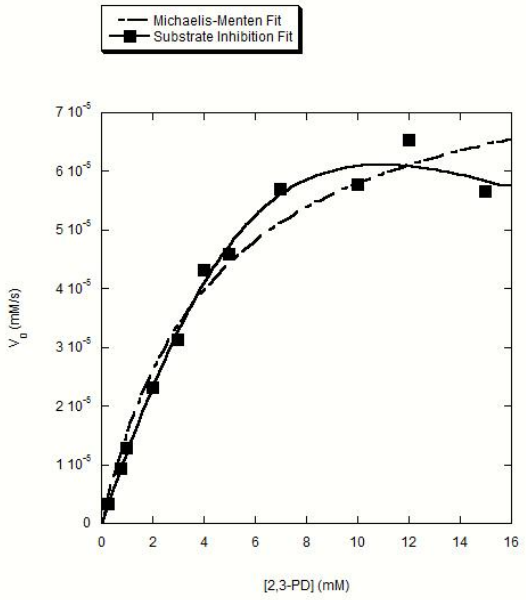

Figure 25. Michaelis-Menten fit (dashed line) and substrate inhibition fit (solid line) for the AKR 163-catalyzed reduction of 2,3-PD. The Michaelis-Menten curve is fit to Equation 1, and the substrate inhibition curve is fit to Equation 2.

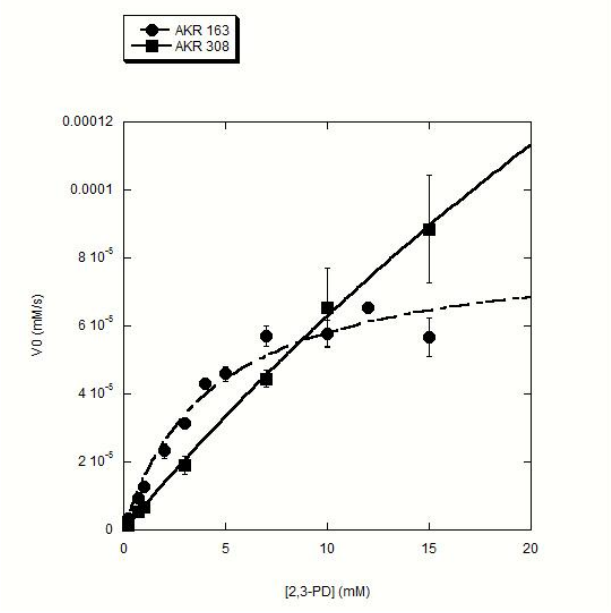

Figure 26. Comparison of the AKR 163-catalyzed and AKR 308-catalyzed reduction of 2,3-PD. AKR 163 is represented by circles, and AKR 308 is represented by squares. All velocities represent the average of three trials, and error bars represent standard error. The velocities for both AKR 163 and AKR 308 are fit to Equation 1. AKR 308's and AKR 163's kinetic parameters for 2,3-PD are shown in Table 2.

Kinetic Analysis of β-Diketones

Findings with 2,3-PD inspired another research direction—an examination of β-diketones. The substrates selected for investigation were 2,4-PD and TF-2,4-PD. 2,4-PD differs from 2,3-PD in that the carbonyls are two carbons apart rather than adjacent to each other. As a result, 2,4-PD lacks an electron-withdrawing group adjacent to the reactive carbonyl. This means that AKR 308-catalyzed reduction of 2,4-PD would be predicted to be less efficient than AKR 308-catalyzed reduction of 2,3-PD. It is also of value to compare 2,4-PD to EAA, which also lacks an electron-withdrawing group adjacent to the reactive carbonyl but does have an additional electron-withdrawing ester functionality. TF-2,4-PD resembles 2,4-PD but contains three fluorine atoms adjacent to one of the carbonyls. These fluorine atoms are electron-

withdrawing and would be expected to increase the reaction rate. TF-2,4-PD was also of interest because it is a dicarbonyl with an additional electron-withdrawing group, similar to EP. If TF-2,4-PD were to exhibit substrate inhibition or cooperativity with AKR 308, it could indicate that these behaviors are properties of dicarbonyls with additional electron-withdrawing groups.

AKR 308's reaction velocities with 2,4-PD and TF-2,4-PD did not exceed 4.79×10^{-6} mM/s or 1.22×10^{-5} mM/s, respectively, and the reaction velocities were not concentration-dependent (data not shown), suggesting that AKR 308 does not catalyze the reduction of these substrates. Supporting this hypothesis, the enzyme-catalyzed reaction rates for TF-2,4-PD were similar in magnitude to the uncatalyzed reaction rates (data not shown). Notably, AKR 163-catalyzed 2,4-PD reduction also failed to achieve velocities greater than 2.54×10^{-6} mM/s even at double the enzyme concentration (data not shown), indicating that 2,4-PD is also a poor substrate for AKR 163.

AKR 308's reaction rates with 2,4-PD and TF-2,4-PD were strikingly different from the rates with 2,3-PD (Figure 27). At a concentration of 15 mM, 2,3-PD's reaction rate was about five times greater than TF-2,4-PD's rate and about 13 times greater than 2,4-PD's rate. While TF-2,4-PD's reaction rate is comparable to EAA, 2,4-PD's reaction rate is less than half that of EAA's. The R^2 values for each substrate are also insightful. 2,3-PD and EAA have R^2 values greater than 0.99, indicating a strong linear regression fit that reflects an actual reaction. In contrast, 2,4-PD and TF-2,4-PD have R^2 values below 0.95, indicating that the decrease in absorbance is nonuniform and may not reflect an actual reaction. While TF-2,4-PD's reaction rate is close in magnitude to EAA's, the difference in R^2 values suggests that this is not a valid

comparison. Overall, β-diketones appear to be poorer substrates than β-keto esters and α-diketones.

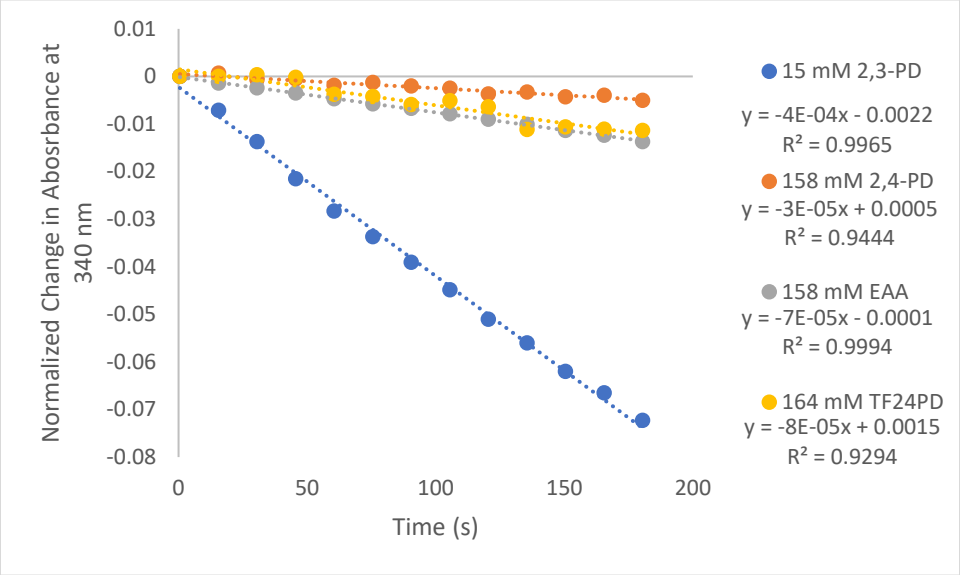

Figure 27. Absorbance changes over time for AKR 308-catalyzed reduction of EAA (gray), 2,3-PD (blue), 2,4-PD (orange), and TF-2,4-PD (yellow) at the maximum substrate concentrations tested. Absorbance changes were normalized by subtracting the absorbance at the initial scan. Linear regression equations and R^2 values for each substrate are noted under the legend entries. The slope of the linear regression equation corresponds to the reaction rate in Abs/s.

Fluorescence

Fluorescence titration of AKR 308 with $NADP^+$ generated a decrease in fluorescence across most of the emission spectrum as $NADP^+$ concentration increased (Figure 28). This is consistent with a transfer of energy from a tryptophan residue to $NADP^+$ that quenches the tryptophan residue's fluorescence.[83] Fitting the ΔF vs [$NADP^+$] plot to Equation 6 (Figure 29) yielded a ΔF_{max} value of $4.0 \times 10^5 \pm 2 \times 10^4$ cps and a K_D value of 1.2 ± 0.2 μM for $NADP^+$ binding to AKR 308.

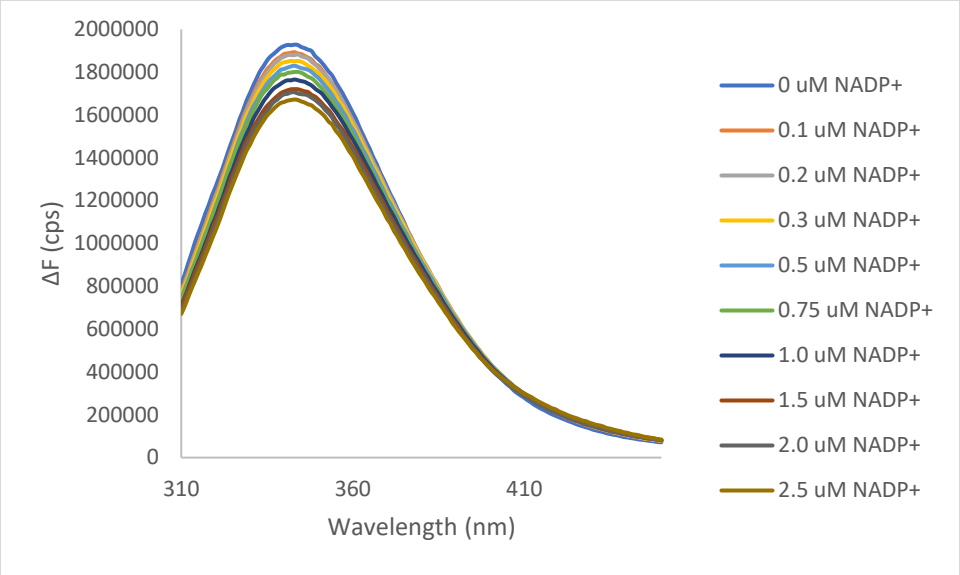

Figure 28. Representative emission spectra for a fluorescence titration of 0.5 µM AKR 308 with 0.1 to 2.5 µM $NADP^+$.

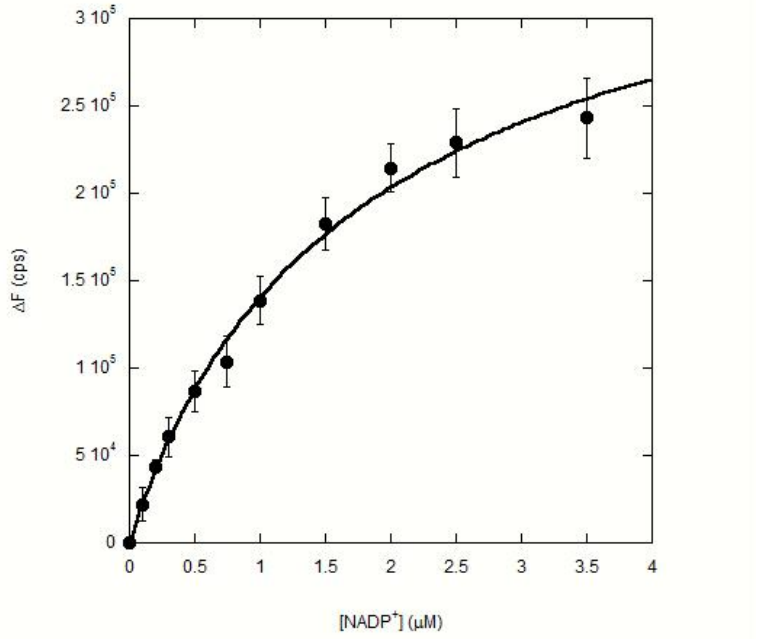

Figure 29. ΔF vs [$NADP^+$] plot fit to Equation 6. ΔF values represent the average of three trials for all $NADP^+$ concentrations except 3.5 µM (average of two trials), and error bars represent SEM.

Fluorescence titrations were attempted with EP, E4ClAA, EAA, and 2,4-PD. However, the K_D values for E4ClAA and EAA were much lower than what was expected based on the K_M values. In addition, fluorescence was almost completely quenched at 3.5 mM E4ClAA (Figure 30), and fluorescence was immediately quenched upon addition of 3 mM 2,4-PD. Therefore, the absorbance of these substrates in the excitation range was measured to identify potential confounding substrate absorbance effects.

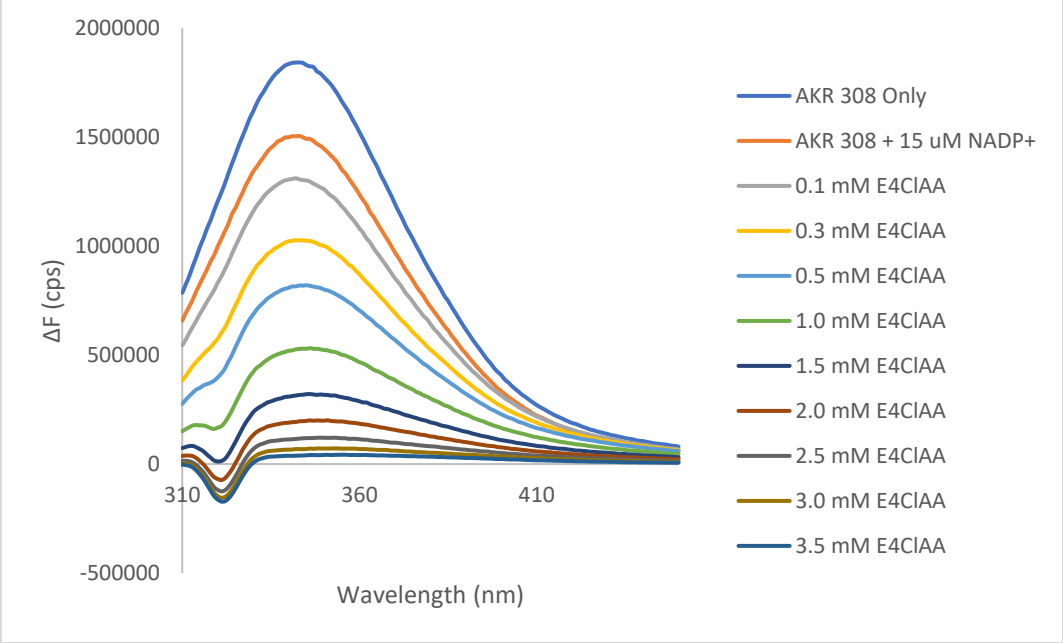

Figure 30. Representative emission spectra for a fluorescence titration of 0.5 µM AKR 308 with 0.1 to 3.5 mM E4ClAA. The "dip" in emission at 325 nm is caused by subtraction of the blank.

3.5 mM E4ClAA and 50 mM 2,4-PD exhibited absorbance values of about 3 at 290 nm (Figure 31). This strong substrate absorbance is likely responsible for the significant quenching of fluorescence. 50 mM EAA's absorbance at 290 nm is about 1.25, and 20 mM EP's absorbance

at 290 nm is about 1. This is less extreme than E4ClAA and 2,4-PD's absorbance values, but it is still a cause for concern.

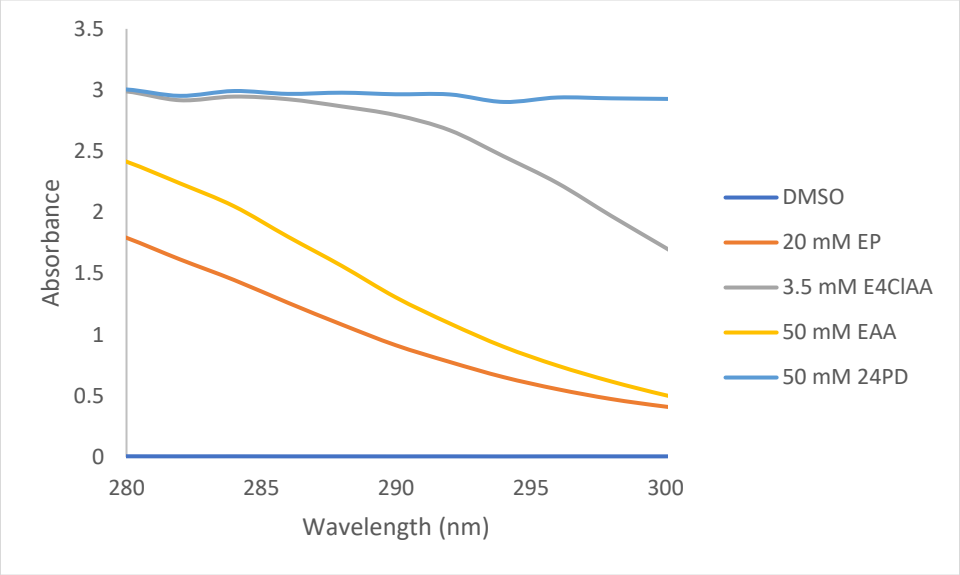

Figure 31. Absorbance of EP (orange), E4ClAA (gray), EAA (yellow), and 2,4-PD (light blue) between 280 and 300 nm. The substrate concentration corresponded to the maximum concentration used in fluorescence titrations. DMSO (dark blue) was included as a negative control.

The significant substrate absorbance at 290 nm limits the interpretability of the emission spectra and K_D values. In an attempt to correct for confounding substrate absorbance effects, the transmittance of E4ClAA at 290 nm was measured. Transmittance values were obtained for each E4ClAA concentration tested in fluorescence experiments, and then the fluorescence values for each E4ClAA concentration were divided by the transmittance value in decimal form. However, because the transmittance values were very low, this corrective method was unsuccessful (data not shown). Therefore, fluorescence experiments with substrates were not pursued further.

Substrate Docking

Catalytic Poses

Catalytic poses were identified for EP, E4ClAA, EAA, 2,3-PD, E2EAA, 2,4-PD, and TF-2,4-PD. Docking scores and notable interactions for each catalytic pose are listed in Table 3, and visual representations of the catalytic poses are shown in subsequent figures. Multiple catalytic poses were identified for 2,3-PD and TF-2,4-PD. The catalytic pose of 2,3-PD discussed in this section has the most optimal hydrogen bonding distances to NADPH and Y71, and the catalytic pose of TF-2,4-PD discussed in this section has the fewest steric clashes. For E2FAA and E2MAA, all poses were at least 5.0 Å from Y71, which is outside of hydrogen bonding range. Therefore, poses of E2FAA and E2MAA were not analyzed further. Selection of a different energy grid or different docking parameters could have produced catalytic poses of these substrates, but this was beyond the scope of the docking study.

Table 3. Docking scores and interactions for catalytic poses.

Substrate	Pose	Rank Score	dG (kcal/mol)	Distance to NADPH (Å)	Distance to Y71 (Å)	Hydrogen-Bonding Contacts (Distance in Å)	Van der Waals Contacts (Number of Interactions)	Steric Clashes (Distance in Å)
EP	6/7	-1.041	-2.541	3.2	3.4	H131 (2.1)	F325, W102, W132	
E4ClAA	3/10	-1.267	-3.475	3.3	3.2	W132 (2.0), H131 (2.0)		
EAA	7/8	-0.833	-2.773	1.9	3.3	H131 (2.1)	W102, A70, Y71	
23PD	3/6	-1.281	-2.582	3.1	3.0	H131 (2.6, 2.0), W132 (2.7)	W102 (2), Y71 (2), W132, F325	
E2EAA	3/10	-1.196	-3.484	3.1	3.6	W132 (2.2), H131 (2.0)	F325, W102 (4), Y71 (4), A70	
24PD	5/5	-1.362	-2.744	1.9	3.2	W132 (2.1), H131 (2.1)	W102 (2), Y71	W102 (3.0)
TF24PD	1/7	-1.969	-2.657	4.1	3.8	W132 (1.8)	W132	

The catalytic poses share some common features. Distances from the substrate to the NADPH hydride transfer site and to the Y71 hydroxyl group typically range from 3 to 4 Å. The exceptions are EAA and 2,4-PD, where the distance to the NADPH hydride transfer site is 1.9 Å, and TF-2,4-PD, where the distance to the NADPH hydride transfer site is 4.1 Å. In the catalytic pose, substrates hydrogen bond with H131 and/or W132, and van der Waals contacts occur with F325, W102, A70, Y71, and/or W132. H131 is one member of the catalytic tetrad,[77] and W102

aligns with AKR1C9 residue W86, which was quenched by NADPH binding in fluorescence experiments.[83]

EP's catalytic pose (Figure 32) has the lowest binding energy out of all seven substrates, and its Rank Score is lower than E4ClAA's and 2,3-PD's (Table 3). EP's shape is planar and horizontal; its proximal carbonyls may produce strong carbon-carbon double bond character that restricts rotation.

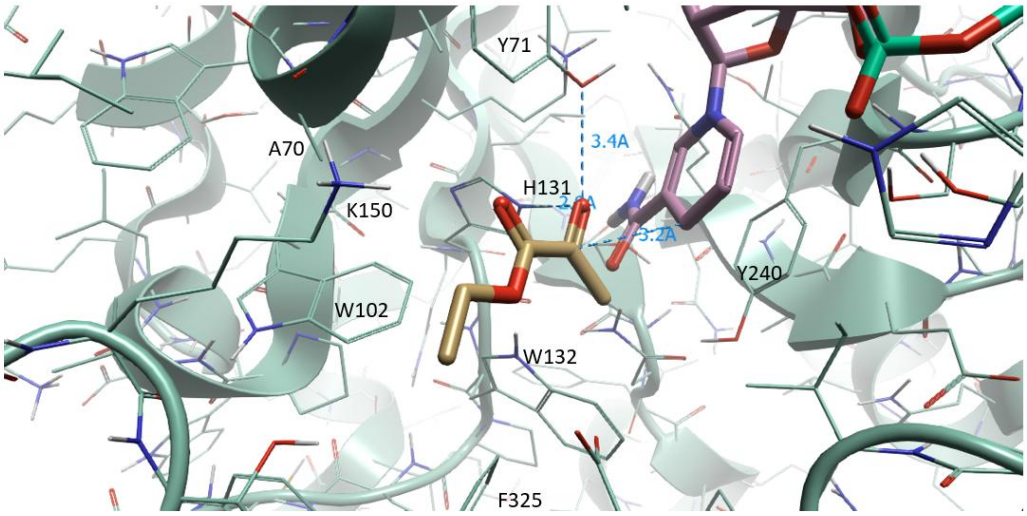

Figure 32. Catalytic pose of EP docked into the active site. Residues are shown in cartoon form, secondary structures are shown in ribbon form, and EP and NADPH are shown in ball and stick form. The residues that typically interact with substrates are labeled. Measurements (blue dashes) indicate the distances from EP to Y71 and NADPH as well as hydrogen bonds with other residues. Carbon atoms in residues are shown in green, oxygen atoms are shown in red, nitrogen atoms are shown in blue, and hydrogen atoms are shown in white.

E4ClAA's catalytic pose (Figure 33) has the second-highest binding energy out of all seven substrates (Table 3). Interestingly, E4ClAA's catalytic pose is the only one that lacks van

der Waals contacts, which could explain its high binding energy. Unlike EP, E4ClAA twists so that the ester functionality hydrogen bonds with W132.

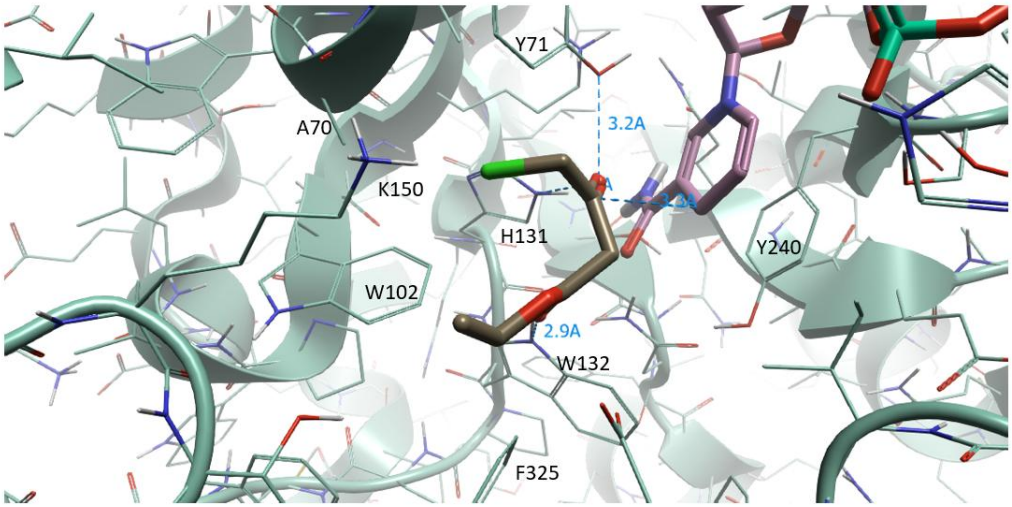

Figure 33. Catalytic pose of E4ClAA docked into the active site.

The diketones—2,3-PD, 2,4-PD, and TF-2,4-PD—are very similar in terms of Rank Score and binding affinity, but there are some notable differences in other aspects. 2,3-PD's catalytic pose (Figure 34) was one of four catalytic poses obtained from docking. The Rank Score of this pose is similar to E4ClAA's (Table 3). 2,3-PD is oriented vertically, with C3 serving as the reactive carbonyl that points toward Y71, C2 oriented toward NADPH and hydrogen bonding with W132, and C4 and C5 pointing toward K150. Like EP, 2,3-PD is mostly linear, with C4 and C5 rotated inward. Again, the planar character may be related to the proximal carbonyls.

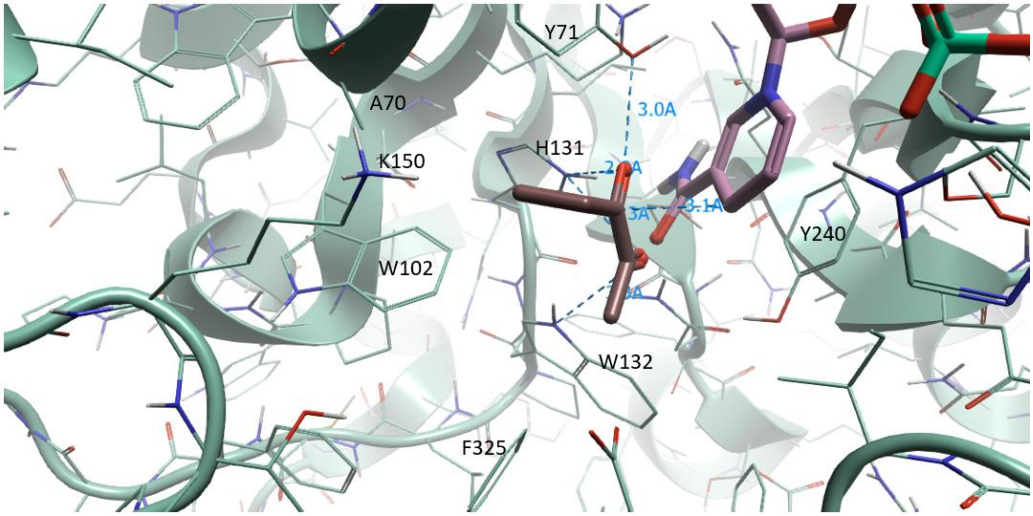

Figure 34. Catalytic pose of 2,3-PD docked into the active site.

2,4-PD's catalytic pose (Figure 35) is much closer to NADPH than the other diketones, and it has a steric clash with W102 (Table 3). These steric clashes could contribute to AKR 308's lack of reactivity with 2,4-PD. This substrate is oriented horizontally and twisted so that the nonreactive carbonyl hydrogen bonds with W132.

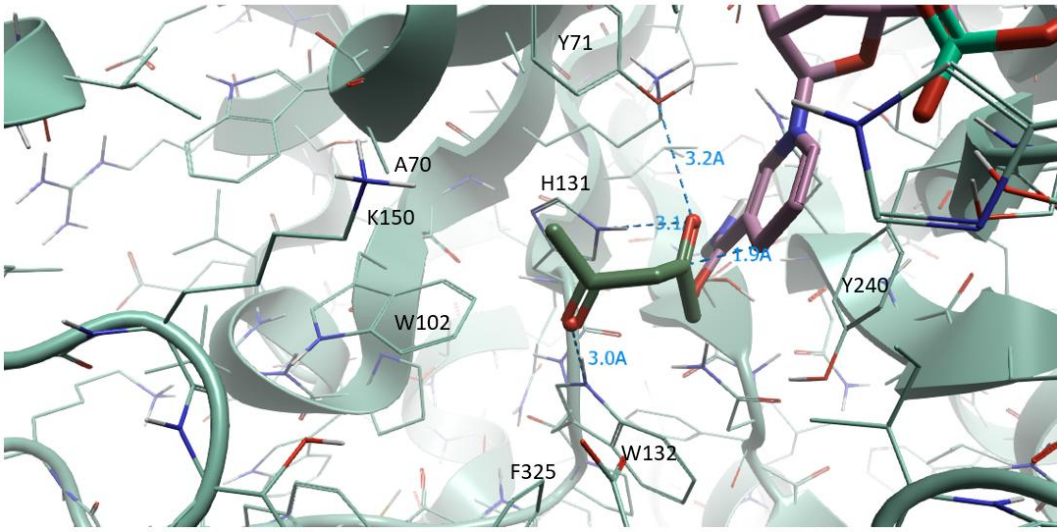

Figure 35. Catalytic pose of 2,4-PD docked into the active site.

TF-2,4-PD's only meaningful interactions occur with W132 (Table 3). The reactive carbonyl is next to the three fluorine atoms and points toward Y71, while the nonreactive carbonyl points down and hydrogen bonds with W132 (Figure 36). Interestingly, the nonreactive carbonyl is closer to NADPH than the reactive carbonyl. As a result, the reactive carbonyl is farthest from NADPH compared to the other substrates.

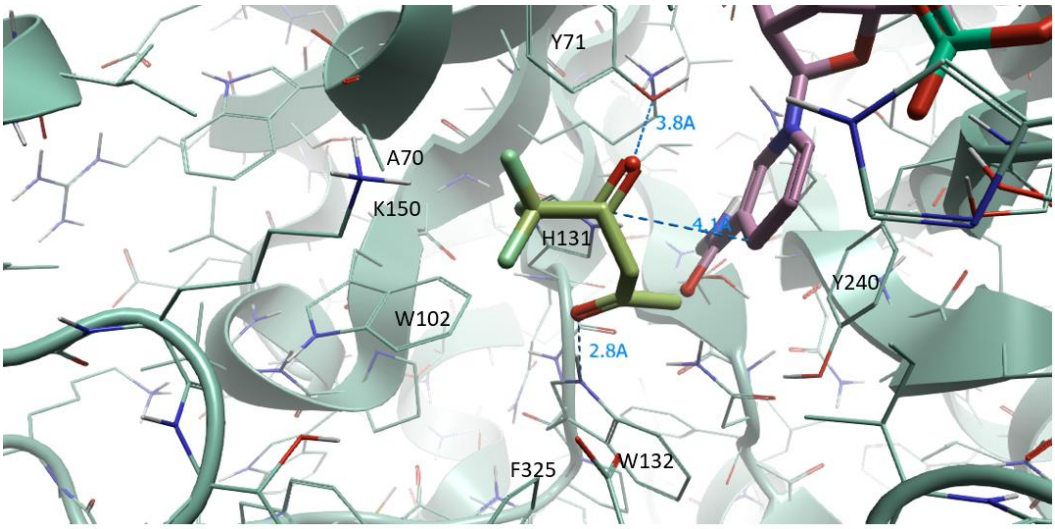

Figure 36. Catalytic pose of TF-2,4-PD docked into the active site.

The docking results for EAA and E2EAA provide some insight into AKR 308's preference for greater steric bulk among the β-keto esters that lack electron-withdrawing substituents. EAA's Rank Score is the lowest out of all nine substrates (Table 3). It is also closer to NADPH than the other substrates, which could produce steric clashes. EAA is mostly planar and horizontal, with the exception of the ethyl group next to the ester, which is rotated toward A70 (Figure 37). EAA's reactive carbonyl is pointed directly toward Y71's hydroxyl group, and the ester does not hydrogen bond with W132.

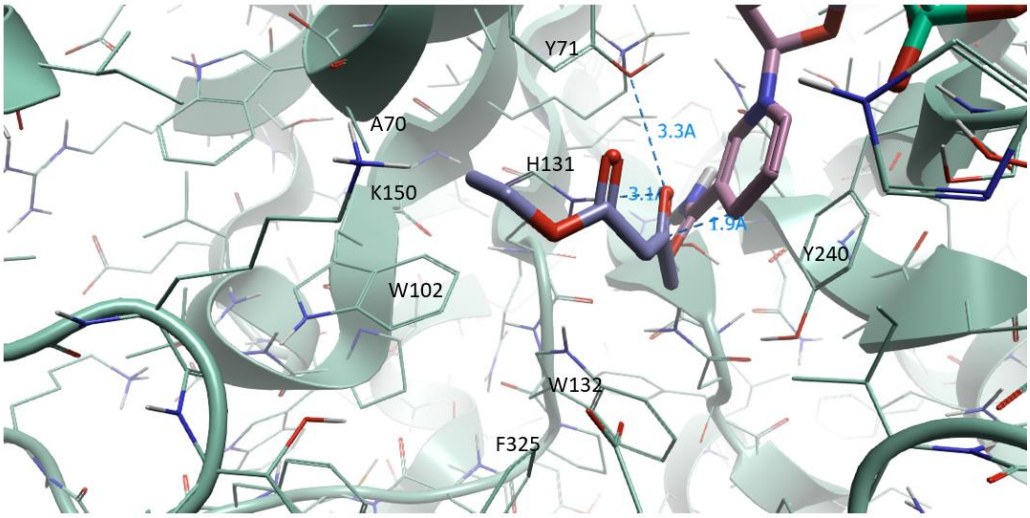

Figure 37. Catalytic pose of EAA docked into the active site.

E2EAA has a greater binding energy than EAA as well as a higher Rank Score (Table 3). Notably, E2EAA's binding affinity is the greatest out of all nine substrates, even though E2EAA lacks electron-withdrawing substituents. Compared to EAA, E2EAA exhibits more van der Waals interactions with Ara1's residues. This is likely due to the increased number of nonpolar substituents in E2EAA, and it could explain the difference in binding affinity. E2EAA's reactive carbonyl lies flat beneath Y71's hydroxyl group, and the ester hydrogen bonds with W132 (Figure 38). The carbon next to the reactive carbonyl points outward, the ethyl substituent points toward A70, and the ethyl group next to the ester points toward W102, permitting more van der Waals contacts compared to EAA.

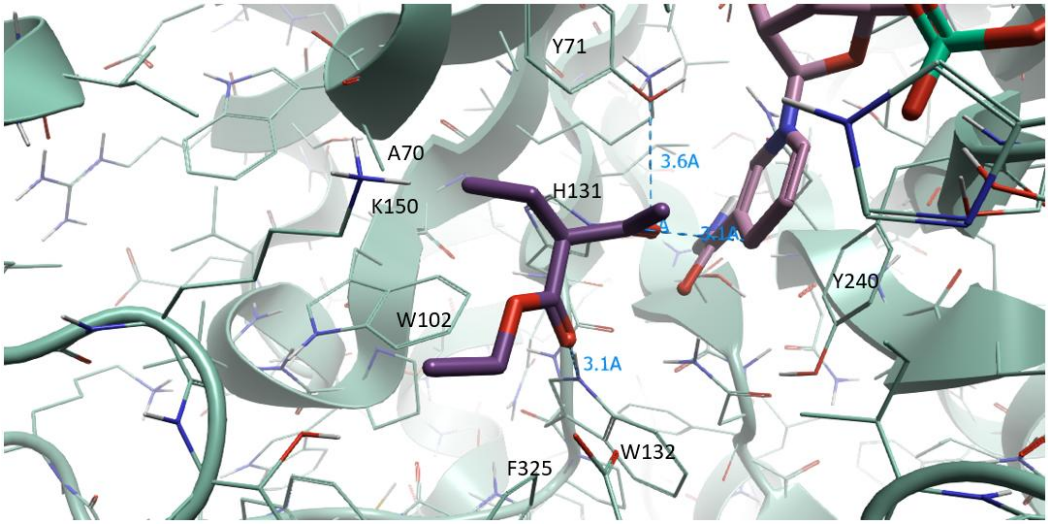

Figure 38. Catalytic pose of E2EAA docked into the active site.

Influence of Noncatalytic and Additional Catalytic Poses

In addition to examining the catalytic poses described above, it is also of interest to analyze noncatalytic (or nonproductive) poses that the substrates can adopt. Noncatalytic poses typically meet one of the following criteria: the reactive carbonyl is pointed down and away from Y71, the ester is facing Y71, the substrate is oriented sideways, or the substrate is too far away from or too close to NADPH or Y71. In some noncatalytic poses, the substrates exhibit hydrogen bonds with K150 and/or van der Waals contacts with Y240, which were not observed for any of the catalytic poses. Poses that overlapped with NADPH are not included within the noncatalytic poses.

EP exhibits two nonproductive poses of note: pose 3 (Figure 39a) and pose 5 (Figure 39b). As shown in Table 4, these poses have higher free energies and Rank Scores than pose 6 (the catalytic pose). In other words, poses 3 and 5 are more likely to be observed experimentally compared to the catalytic pose, and they have higher binding affinities than the catalytic pose.

Pose 3 is oriented so that the carbonyls point outward, and it is rotated 90 degrees relative to the catalytic pose. The reactive carbonyl hydrogen bonds with K150, and the ester is aligned with Y71's hydroxyl group but points away from it, hydrogen bonding with W132. In pose 5, the ester points toward Y71, while the reactive carbonyl points down and hydrogen bonds with W132.

Table 4. Scores, interactions, and catalytic potential of EP's docking poses.

Pose	Rank Score	dG (kcal/mol)	Hydrogen-Bonding Contacts (distance in Å)	Van der Waals Contacts (Number of Interactions)	Evaluation of Catalytic Potential
3	-1.294	-2.826	W132 (2.8), K150 (2.1)	W132, W102 (2), A70, Y71	Noncatalytic. Ester facing Y71.
5	-1.183	-2.829	W132 (2.3), H131 (2.2)	Y71 (2), W102 (2), A70, W132	Noncatalytic. Reactive carbonyl pointing down.
6	-1.041	-2.541	H131 (2.1)	F325, W102, W132	Catalytic

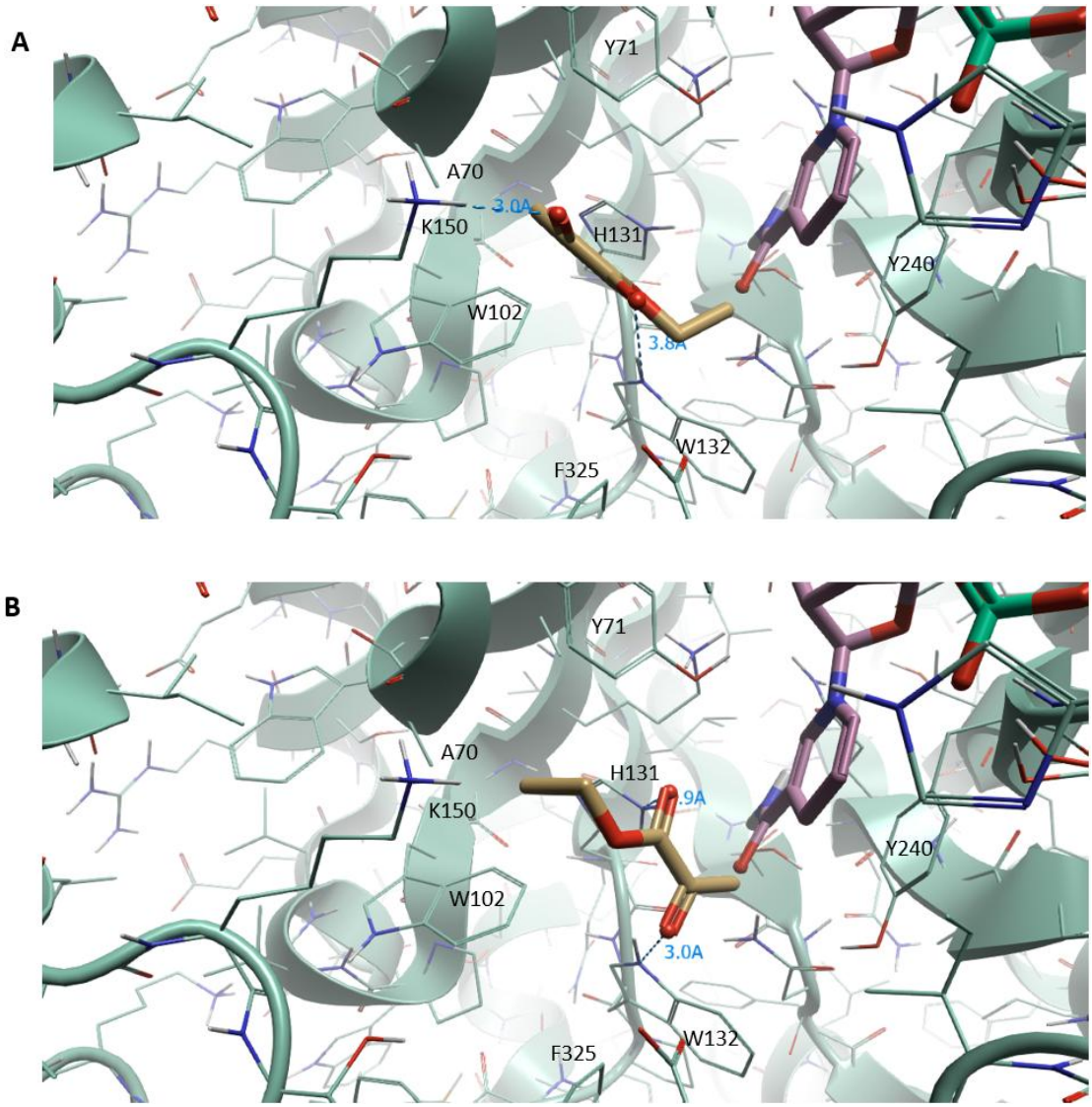

Figure 39. EP poses 3 (a) and 5 (b) docked into the active site.

Poses 2 (Figure 40a), 4 (Figure 40b), and 6 (Figure 40c) of E4ClAA have similar binding energies and Rank Scores and slightly higher binding energies compared to pose 3 (the catalytic pose). These poses are compared in Table 5. In pose 2, the reactive carbonyl points down toward W132, the ester hydrogen bonds with K150, and the chlorine atom is located near NADPH. The ester is aligned with Y71 in both poses 4 and 6, with the reactive carbonyl hydrogen bonding

with K150. In pose 4, the ester points toward Y71, and in pose 6, the ester points outward. Pose 6 also exhibits a halogen bond between the chlorine atom and T151. Poses 2, 4, and 6 are much closer to NADPH than pose 3.

Table 5. Scores, interactions, and catalytic potential of E4ClAA's docking poses.

Pose	Rank Score	dG (kcal/mol)	Hydrogen-Bonding Contacts (distance in Å)	Van der Waals Contacts (Number of Interactions)	Evaluation of Catalytic Potential
2	-1.345	-3.447	K150 (2.0), W132 (1.9), H131 (2.8)	W102 (3), F325, Y71	Noncatalytic. Reactive carbonyl pointing down.
3	-1.267	-3.475	W132 (2.0), H131 (2.0)		Catalytic
4	-1.148	-3.489	K150 (2.0)	W132	Noncatalytic. Ester facing Y71
6	-1.003	-3.499	W132 (2.5), H131 (2.2), K150 (2.1)	W102 (2)	Noncatalytic. Ester facing Y71

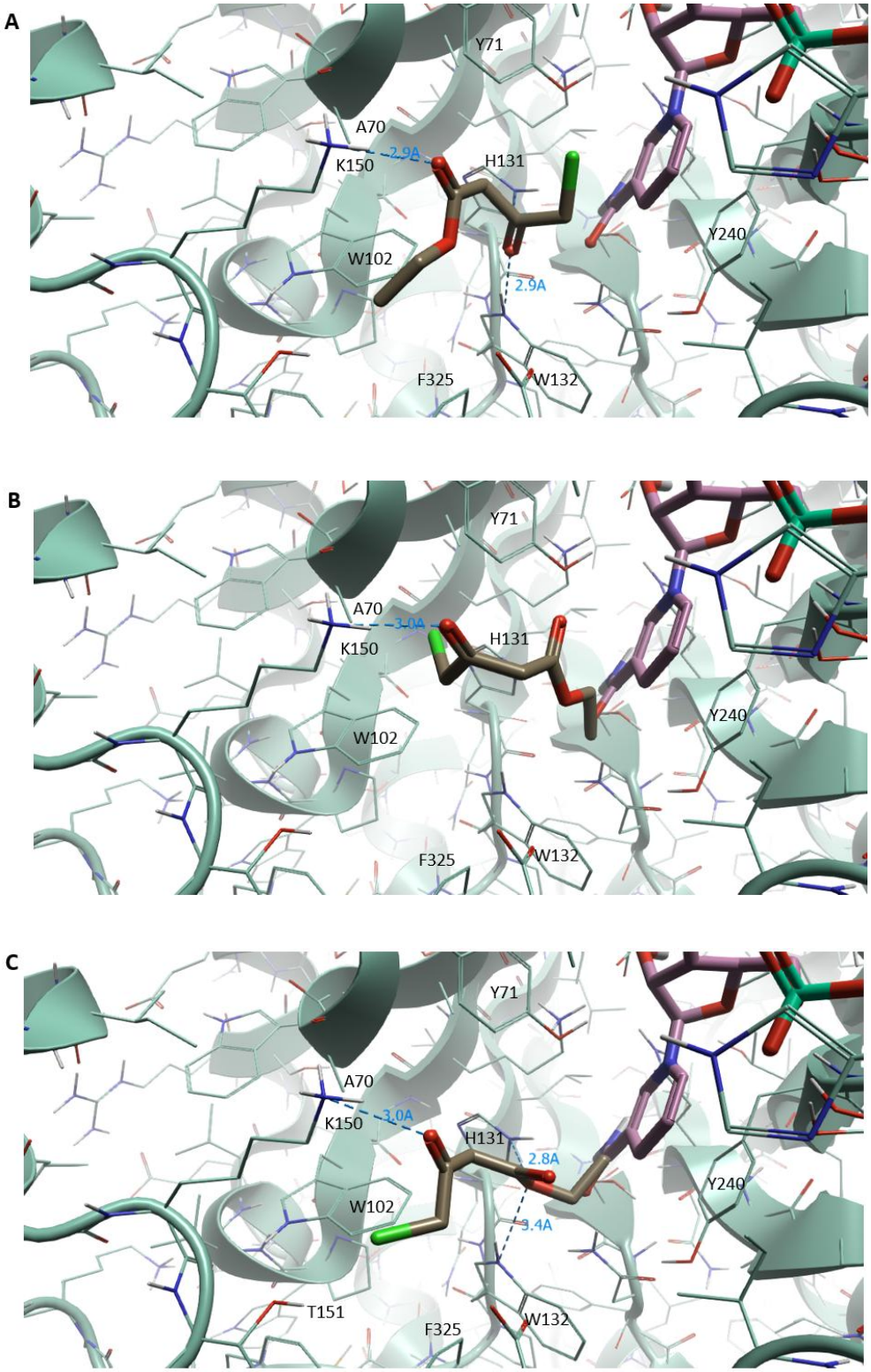

Figure 40. E4ClAA poses 2 (a), 4 (b), and 6 (c) docked into the active site.

There are four poses of EAA ranked above the catalytic pose in terms of Rank Score and binding energy. Of these poses, pose 2 (Figure 41) has the fewest steric clashes with NADPH and is therefore most likely to be observed experimentally. Poses 2 and 7 (the catalytic pose) are compared in Table 6. In pose 2, the reactive carbonyl points down and hydrogen bonds with W132, and the ester hydrogen bonds with K150. The ethyl group next to the ester points toward W102, allowing for more van der Waals contacts relative to the catalytic pose. The catalytic pose is also more linear compared to pose 2.

Table 6. Scores, interactions, and catalytic potential of EAA's docking poses.

Pose	Rank Score	dG (kcal/mol)	Hydrogen-Bonding Contacts (distance in Å)	Van der Waals Contacts (Number of Interactions)	Evaluation of Catalytic Potential
2	-1.549	-3.175	K150 (2.0), W132 (1.8)	F325, W102 (4), Y71	Noncatalytic. Carbonyl pointing down
7	-0.833	-2.773	H131 (2.1)	W102, A70, Y71	Catalytic

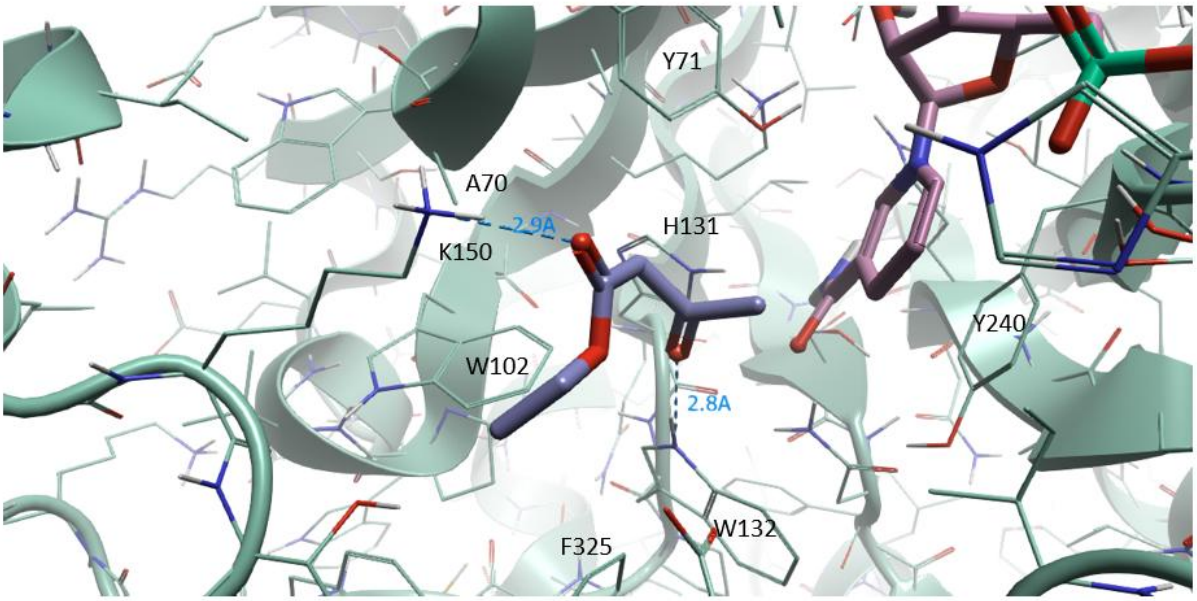

Figure 41. EAA pose 2 docked into the active site.

Unlike EP, E4ClAA, and EAA, the majority of 2,3-PD's poses are catalytic. Data for these poses is shown in Table 7. 2,3-PD also exhibits one noncatalytic pose that is not shown in Table 7. Pose 1 (Figure 42a) is 2.9 Å from NADPH and 3.9 Å from Y71. Both carbonyls point down, but the distance between the reactive carbonyl and Y71 is comparable to other catalytic poses. C2 is the reactive carbonyl, and C4 and C5 generate a steric clash with W102. Pose 3 (Figure 34) is vertical, with C2 and C3 facing in the same direction. Pose 3 was selected to compare with the other substrates' catalytic poses due to the short distances to NADPH and Y71 (3.1 Å and 3.0 Å, respectively). C3 points toward Y71, and C2 hydrogen bonds with W132. Pose 4 (Figure 42b) is 3.7 Å from both NADPH and Y71. It is oriented vertically, with C3 parallel with Y71 and C2 pointing in the opposite direction and hydrogen bonding with W132. Pose 6 (Figure 42c) is 3.2 Å from NADPH and 3.4 Å from Y71. It is oriented horizontally, with C2

pointing toward Y71 and C3 pointing outward. In pose 6, 2,3-PD does not hydrogen bond with W132.

Table 7. Scores and interactions of 2,3-PD's docking poses

Pose	Rank Score	dG (kcal/mol)	Hydrogen-Bonding Contacts (Distance in Å)	Van der Waals Contacts (Number of Interactions)	Steric Clashes (Distance in Å)
1	-1.533	-2.714	H131 (2.1), W132 (2.0)	Y71 (3), A70, W102 (2)	W102 (3.0)
3	-1.281	-2.582	H131 (2.6, 2.0), W132 (2.7)	W102 (2), Y71 (2), W132, F325	
4	-1.212	-2.626	W132 (1.8)	W132, W102 (2), Y71 (2)	
6	-0.907	-2.366	H131 (2.0)	Y71 (4), W132	

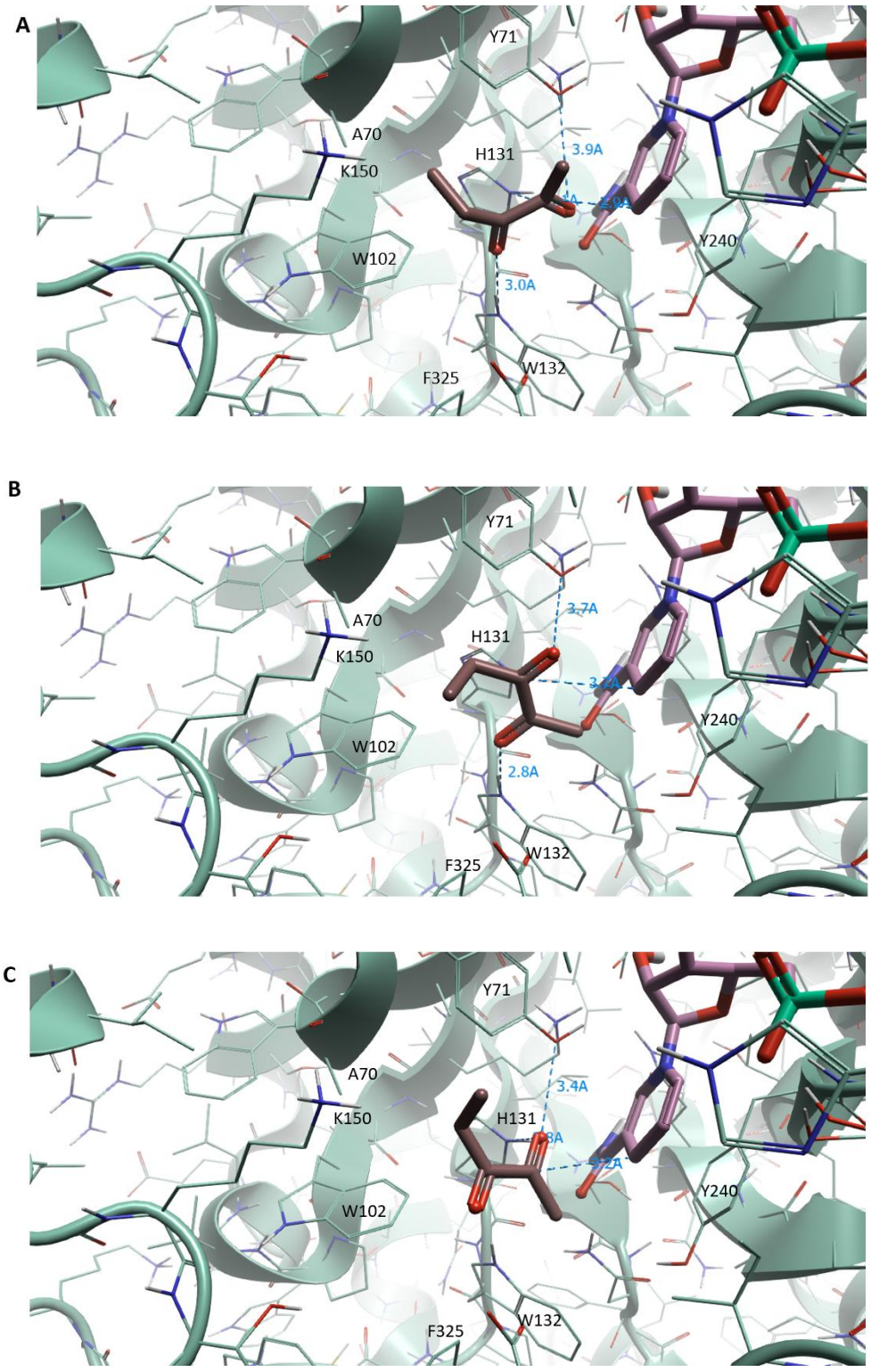

Figure 42. 2,3-PD docking poses 1 (a), 4 (b), and 6 (c).

2,3-PD's poses can be compared to an experimental analysis by Calam et al.[72] as well as the docking results obtained by Hu et al.[77] Based on Calam et al.'s gas chromatography analysis, Ara1 reduces C2 in 2,3-PD to form (*S*)-2-hydroxy-3-pentanone. This would be consistent with poses 1 and 6, where C2 forms a hydrogen bond with Y71. However, poses 1 and 6 are less optimal than poses 3 and 4, where C3 is reduced. In pose 1, 2,3-PD is outside the typical hydrogen bonding range, and there is a steric clash with W102. Pose 6 has the lowest Rank Score and binding energy out of the catalytic poses. Hu et al. also docked 2,3-PD into Ara1's active site with C3 facing Y71, which does not align with Calam et al.'s findings. In Hu et al.'s pose, C2 is parallel with W132, and C4 and C5 are located between W132 and NADPH. This type of pose was not obtained in this docking study. The hydrogen bonding distance between the reactive carbonyl and Y71 is 3.3 Å, which is most similar to pose 6.

Allosteric Sites

In addition to examining poses in the active site, another goal of substrate docking was to determine whether Ara1 has any allosteric sites that could explain AKR 308's cooperative behavior with EP. Table 8 shows the amino acid sequences of the pockets generated by PASSer's ensemble model with the highest probability of being allosteric sites. The letters after the amino acid codes correspond to one of Ara1's two monomeric chains, which are marked as A and C. The pockets are shown graphically in the context of Ara1's crystal structure in Figure 43. Pocket 1 is located at the top of chain A and branches into the dimeric interface. Pocket 2 spans the middle of the dimeric interface and occupies a portion of chain C. Pocket 3 is located at the bottom of chain C.

Table 8. Probabilities and amino acid sequences for allosteric sites generated by PASSer.

Pocket Number	Probability	Residues
1	40.58%	K228A, F298C, R277A, E297C, L16C, M15C, S300A, N310A, M224A, Q278A, V265C, F321A, P222A, R227A, T302A, K262C, Y263C, L306A, K303A, N264C
2	34.68%	Y263A, L306C, K228C, Q278C, M224C, M15A, N264A, E297A, Y263C, K303C, L16A, T302C, S300C, F231C, K262C, K262A, T302A, V265A, F298A, R227C, R277C, E225C
3	30.79%	Q169C, K172C, Q173C, D180C, D183C, R185C, V109C, R111C, E108C, I177C, D107C, K176C, D110C

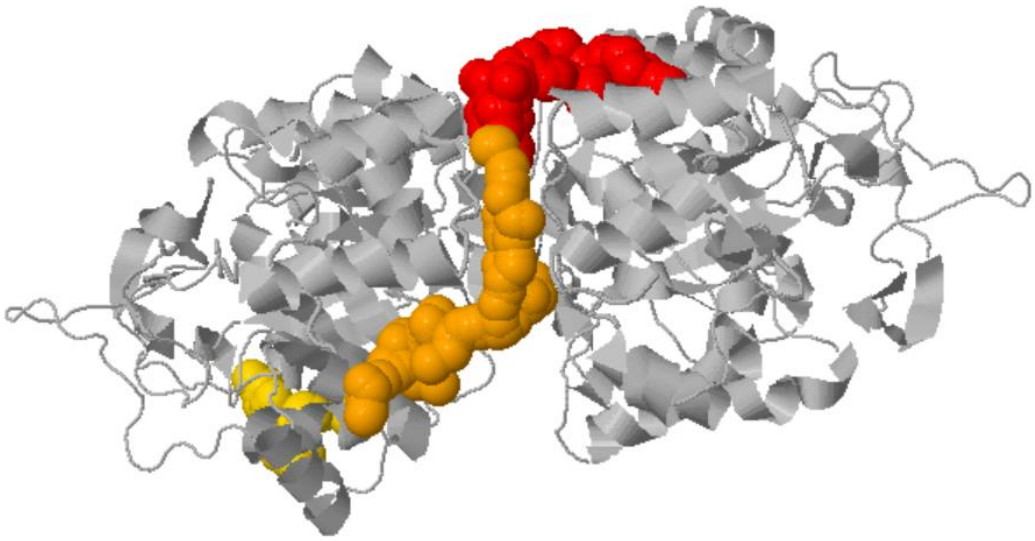

Figure 43. JSmol image output from PASSer highlighting the allosteric pockets in the Ara1 crystal structure. Pocket 1 is shown in red, pocket 2 is shown in orange, and pocket 3 is shown in yellow. Chain C is located to the left, and chain A is located to the right.

EP, E4ClAA, and 2,3-PD were docked into each pocket. E4ClAA and 2,3-PD were docked for the purpose of comparison with EP. 2,3-PD is a 2,3-dicarbonyl that is most similar in structure to EP, and both 2,3-PD and E4ClAA are examples of electron-withdrawing substrates that produced Michaelis-Menten kinetics, in contrast to AKR 308's more unique kinetic

behaviors with EP. Ideally, E4ClAA and 2,3-PD would have lower binding energies, fewer favorable interactions with amino acids, and/or a larger number of steric clashes in an allosteric pocket compared to EP.

With the exception of one pose of 2,3-PD, the substrates docked into an identical location in pocket 1 (Figure 44). The substrates bound near the dimeric interface, hydrogen bonding with the R group of R227A and the backbone amine of L237A, which is part of a β-sheet that extends to the active site. Van der Waals interactions occur with R227A, L237A, L236A, and F231A. Like L237A, L236A is a component of the β-sheet. R227A and F231A were included among the pocket 1 residues identified by PASSer, while the two leucine residues were not.

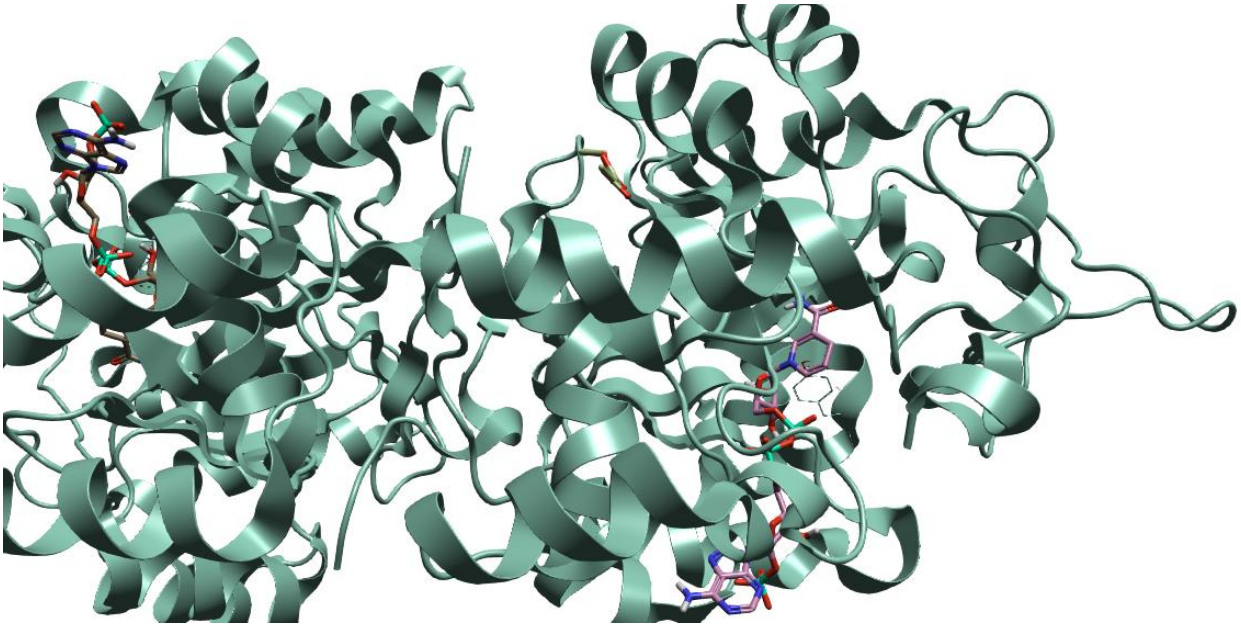

Figure 44. Ara1 crystal structure with EP docked into pocket 1. Secondary structures are shown in cartoon form. EP and NADPH are shown in ball and stick form. Y71 is shown in stick form to mark the active site.

EP's binding energies for pocket 1 are about 1 kcal/mol greater than EP's binding energies in the active site (Table 9). This pattern, where binding energies in the allosteric pocket exceed binding energies in the active site, was commonly observed across different pockets and substrates. EP's Rank Scores are also greater than those produced in active site docking. However, it is important to note that the docking grid for allosteric sites was much larger than the grid for the active site, potentially allowing for poses with higher Rank Scores and binding energies. Hydrogen bonds were more common with L237A than with R227A. Interestingly, EP does not exhibit steric clashes in pocket 1. EP is completely linear in two poses, and three poses only feature rotation of the ethyl group next to the ester, indicating minimal conformational adjustments to bind pocket 1. A representative pose of EP in pocket 1 is shown in Figure 45.

Table 9. Scores and interactions for EP's docking poses in pocket 1.

Pose	Rank Score	dG (kcal/mol)	Hydrogen-Bonding Contacts (Distance in Å)	Van der Waals Contacts (Number of Interactions)
1	-2.714	-3.721	R227A (2.4), L237A (2.0)	F231A, R227A, L236A
2	-2.081	-3.585	R227A (2.6), L237A (2.0)	F231A
3	-2.041	-3.527	R227A (2.0)	L236A
4	-1.938	-3.615	L237A (2.0)	L236A, R227A (2)
5	-1.813	-3.515	L237A (2.0)	L236A, R227A (2)

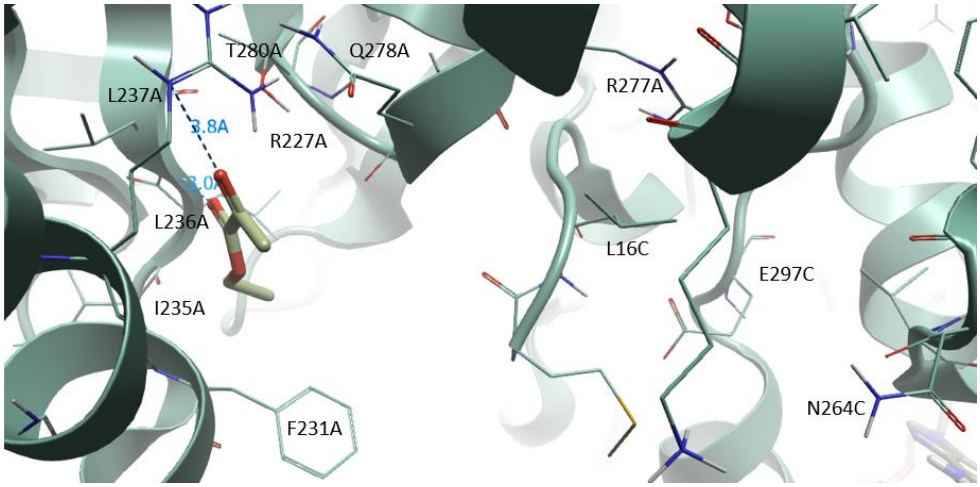

Figure 45. EP pose 1 docked into pocket 1.

E4ClAA's binding energies are among the highest observed in the entire docking study, but its Rank Scores are generally lower than EP's poses in pocket 1 (Table 12 in the Appendix). Strikingly, every pose in pocket 1 exhibits at least one steric clash. This scenario did not occur for any other combination of substrate and pocket. E4ClAA's poses are also more contorted than EP's, with rotation along several single bonds often necessary to achieve the desired pose. With the exception of pose 1, E4ClAA favors hydrogen bonds with L237A over R227A, similar to what was observed with EP. A representative pose of E4ClAA in pocket 1 is shown in Figure 53 in the Appendix.

Data for 2,3-PD's docking into pocket 1 is shown in Table 13 in the Appendix. Like EP, 2,3-PD's binding energies are about 1 kcal/mol higher than the binding energies for the active site, and the Rank Scores are greater than those for the active site (Table 13 in the Appendix). Three of 2,3-PD's poses exhibit a steric clash. Unlike the other substrates and 2,3-PD's other poses, pose 2 (Figure 54 in the Appendix) is located in a different region of pocket 1. Pose 2 is

located in the dimeric interface, hydrogen bonding with R277A and exhibiting van der Waals contacts with L16C and N264C. This binding site is more similar to those observed in pocket 2. Pose 2 has the second-lowest binding energy among 2,3-PD's five poses along with a steric clash. 2,3-PD's poses in pocket 2 are more similar to EP's and are not as contorted as E4ClAA's. C4 and C5 often exhibit significant rotation. Like EP and E4ClAA, hydrogen bonds are more common with L237A than with R227A. Pose 1 is also unique in hydrogen bonding with T280A.

The substrates docked into three different locations in pocket 2, which spans the dimeric interface and branches into chain C. These three binding sites likely arise from the large energy grid that encapsulates pocket 2. The first binding site (binding site 1) occurs within the dimeric interface (Figure 46a). In this binding location, substrates typically hydrogen bond with R277A and N264C while forming van der Waals contacts with residues like L16C and Y263C. 2,3-PD pose 2 also docked into this binding location. The second binding site (binding site 2) is located within chain C (Figure 46b), which mirrors the most common binding location in pocket 1. Here, the substrates typically hydrogen bond with R227C, which is located within an α-helix, and they form van der Waals contacts with K228C, F231C, and L237C. The third binding site (binding site 3) is located at the edge of the dimeric interface, near several loop structures (Figure 46c). In this binding site, the substrates typically form hydrogen bonds with R277C, N264A, and K303C as well as van der Waals contacts with M15A, E297A, L16A, and V265A. Poses in the second binding location typically have lower binding energies than poses in the first and third binding locations.

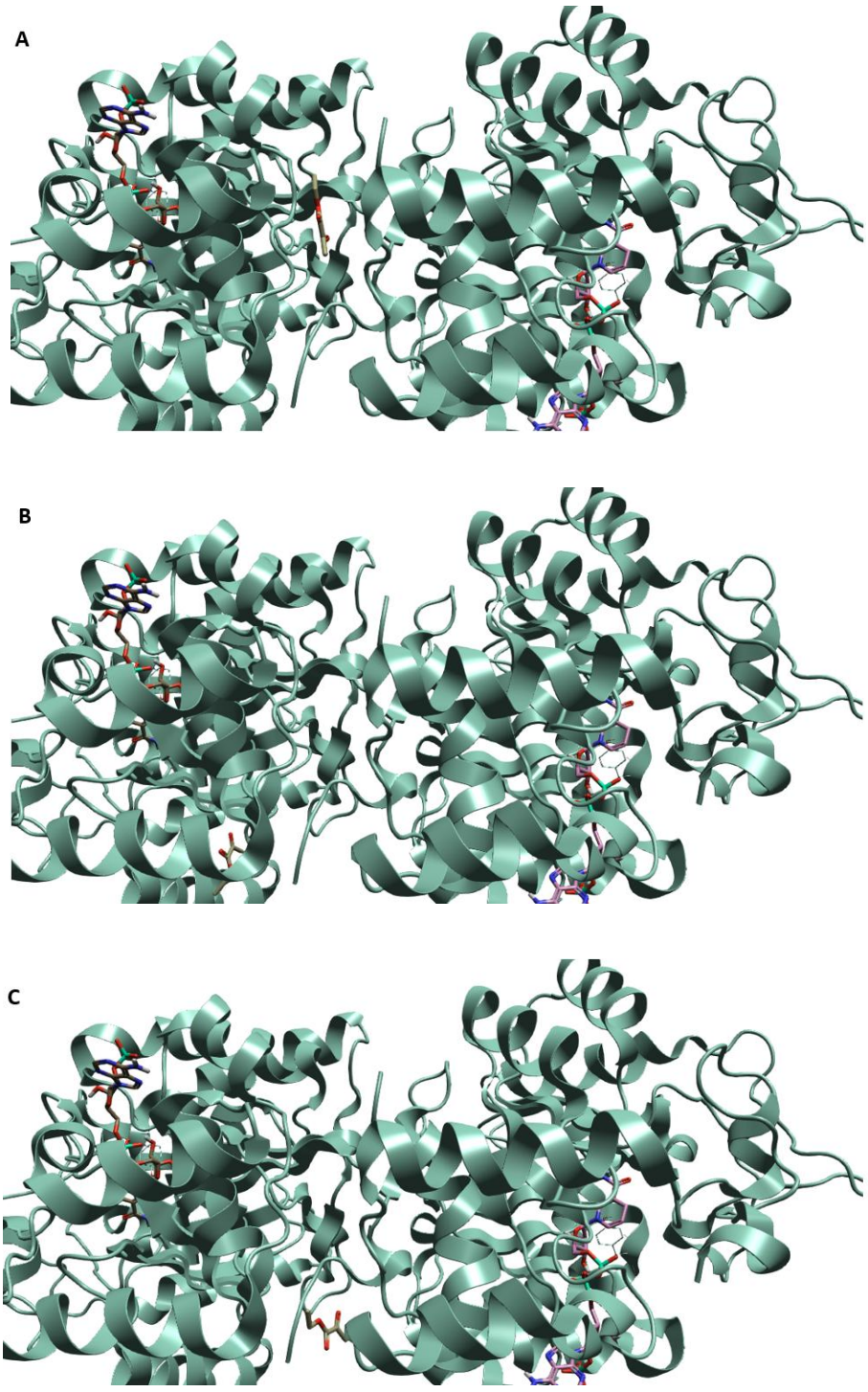

Figure 46. Ara1 crystal structure with EP docked into pocket 2 in three different positions: pose 1 (a), pose 2 (b), and pose 3 (c).

EP poses 1 (Figure 47a), 4, and 5 are located in binding site 1, pose 2 (Figure 47b) is located in binding site 2, and pose 3 (Figure 47c) is located in binding site 3. EP's binding energies in pocket 2 (Table 10) are generally lower than its binding energies in pocket 1. The Rank Scores for pocket 2 are generally similar to the Rank Scores for all poses in pocket 1 except for pose 1, which has a Rank Score of -2.714. Three poses exhibit steric clashes; pose 2 in binding site 2 clashes with T280C, and two poses in binding site 1 clash with S300A. EP is completely linear in poses 1 and 4.

Table 10. Scores and interactions for EP's docking poses in pocket 2.

Pose	Rank Score	dG (kcal/mol)	Hydrogen-Bonding Contacts (Distance in Å)	Van der Waals Contacts (Number of Interactions)	Steric Clashes (Distance in Å)
1	-2.091	-3.591	R277A (2.5), S300A (2.0)	L16C, Y263C (2)	S300A (2.8, 2.9)
2	-2.004	-3.106	R227C (2.0, 2.6)		T280C (2.8)
3	-1.981	-3.535	R277C (2.5, 2.0), N264A (2.6)	T302C, M15A, E297A (2)	
4	-1.975	-3.402	R277A (2.1, 2.5, 2.2), N264C (2.9)	E297C	
5	-1.92	-3.482	K303A (2.0), R277A (2.9, 2.4)	Y263C (2), N264C	S300A (3.0)

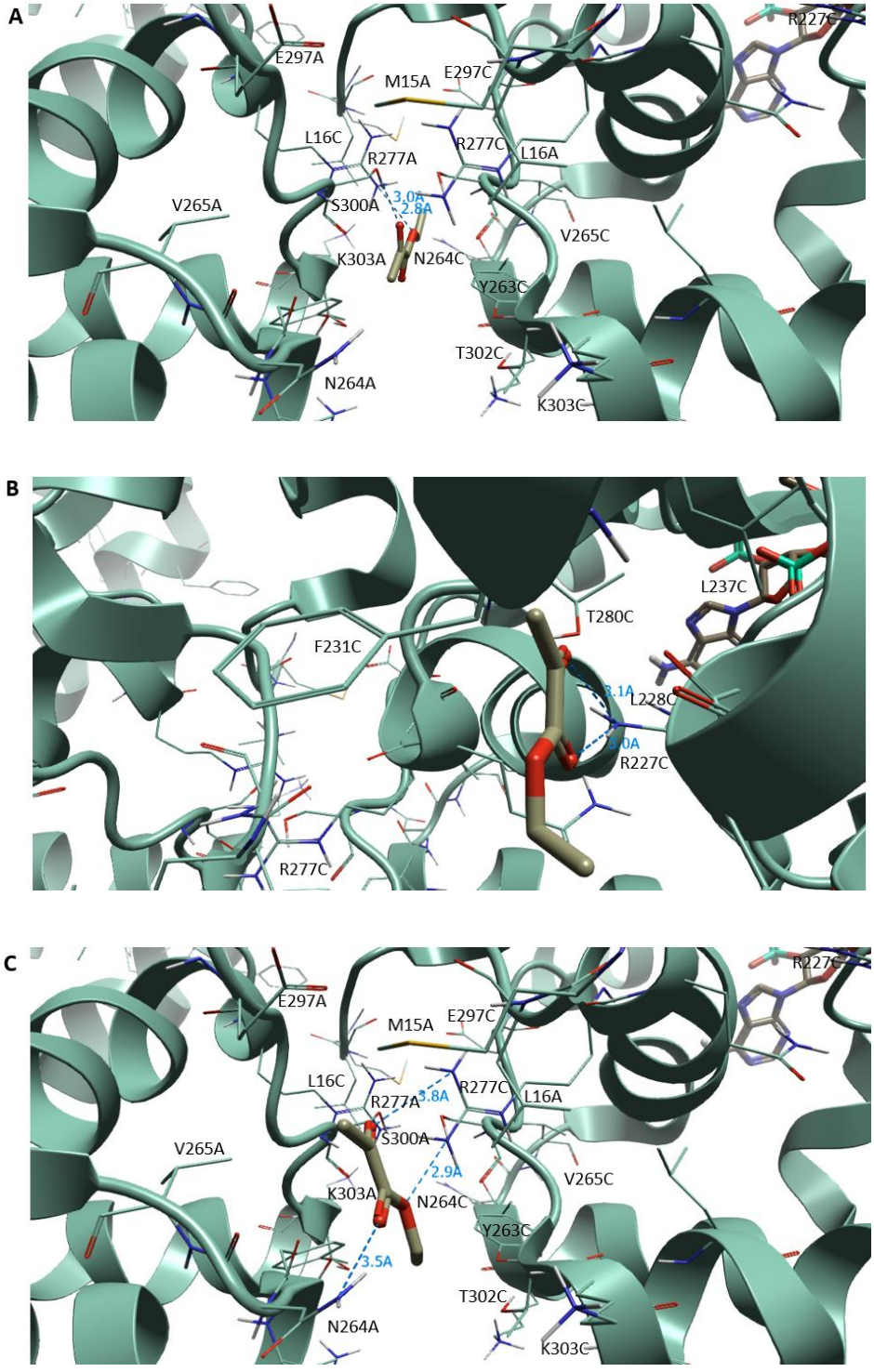

Figure 47. EP docked into binding site 1 (pose 1, a), binding site 2 (pose 2, b), and binding site 3 (pose 3, c) in pocket 2.

The free energies and Rank Scores for E4ClAA in pocket 2 (Table 14 in the Appendix) are similar to the data for pocket 1. Poses 2, 4, and 5 docked in binding site 3, while pose 1 (Figure 55 in the Appendix) docked in binding site 1 and pose 3 docked in binding site 2. The free energies for binding site 3 are greater than those for binding sites 1 and 2. Unlike EP and 2,3-PD, E4ClAA does not exhibit any steric clashes in pocket 2. Like pocket 1, E4ClAA is more contorted in pocket 2 than EP and 2,3-PD.

2,3-PD poses 1 (Figure 56 in the Appendix), 4, and 5 docked into binding site 2, while pose 2 docked into binding site 3 and pose 3 docked into binding site 1. In other words, 2,3-PD favors binding site 2, in contrast to EP and E4ClAA. 2,3-PD's binding energies for binding site 2 are lower than the energies for the other binding sites (Table 15 in the Appendix), which is characteristic of pocket 2. The binding energies are lower than those observed for pocket 1, while the Rank Scores are similar. Pose 1 and pose 3 exhibit steric clashes. Both 2,3-PD and EP exhibited a steric clash with T280C when docking into binding site 2. On the other hand, EP exhibited a steric clash with S300A in binding site 1, while 2,3-PD clashed with E297C. 2,3-PD is nonlinear in all poses, with some rotation around the C4-C5 axis occurring.

All substrates docked in the same general location in pocket 3 (Figure 48), near two α-helices on the enzyme's outer edge. The substrates typically formed hydrogen bonds with the backbone amines of V109C, D110C, and R111C within one of the α-helices. In some poses, the substrates formed hydrogen bonds with the R group of K176C, located on the second α-helix. Van der Waals contacts most commonly occurred with Q173C, K176C, and I177C. Steric clashes occurred most frequently with Q173C. Free energies for binding in pocket 3 were generally lower compared to pockets 1 and 2.

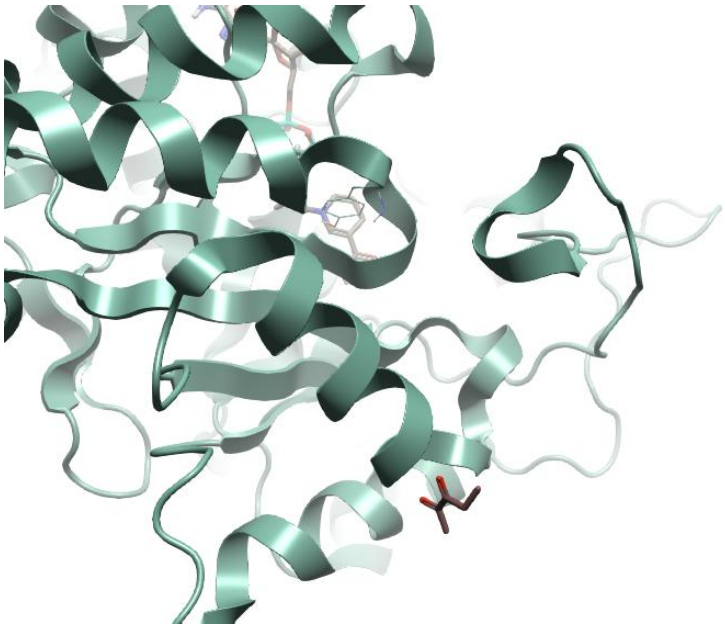

Figure 48. Ara1 crystal structure with EP docked into pocket 3.

While the free energies for EP poses 1 (Figure 49a) and 4 in pocket 3 (Table 11) are similar to those typically observed for pocket 2, the free energies for the rest of the poses are noticeably lower compared to those typically observed for pockets 1 and 2. The Rank Scores for poses 4 (Figure 49b) and 5 are lower than those typically observed for EP poses docked into other pockets. In pose 1, the reactive carbonyl and the alkoxy group in the ester form hydrogen bonds with V109C, D110C, and R111C, whereas in poses 2 and 3, both carbonyls form hydrogen bonds with these residues. Pose 3 exhibits a steric clash between the ester carbonyl and Q173C. In poses 4 and 5, one carbonyl points toward the α-helix containing V109C, D110C, and R111C, and the other carbonyl hydrogen bonds with K176C's R group. In pose 4, the ester carbonyl hydrogen bonds with K176C, and in pose 5, the reactive carbonyl hydrogen bonds with K176C. All poses exhibit some rotation of the ethyl group next to the ester, with pose 1 exhibiting the least rotation.

Table 11. Scores and interactions for EP's docking poses in pocket 3.

Pose	Rank Score	dG (kcal/mol)	Hydrogen-Bonding Contacts (Distance in Å)	Van der Waals Contacts (Number of Interactions)	Steric Clashes (Distance in Å)
1	-2.247	-3.351	V109C (2.9), D110C (2.0, 2.7), R111C (2.0)	Q173C, I177C (2), D110C	
2	-2.005	-2.898	V109C (2.5), D110C (1.9), R111C (1.9)	R111C	
3	-1.899	-2.992	R111C (2.0), D110C (2.8, 1.8), V109C (2.2)	K176C	Q173C (2.6)
4	-1.752	-3.138	K176C (2.1), D110C (2.1)	I177C, Q173C	
5	-1.681	-2.989	K176C (2.4), D110C (1.8), V109C (2.8)	D110C, I177C, K176C	

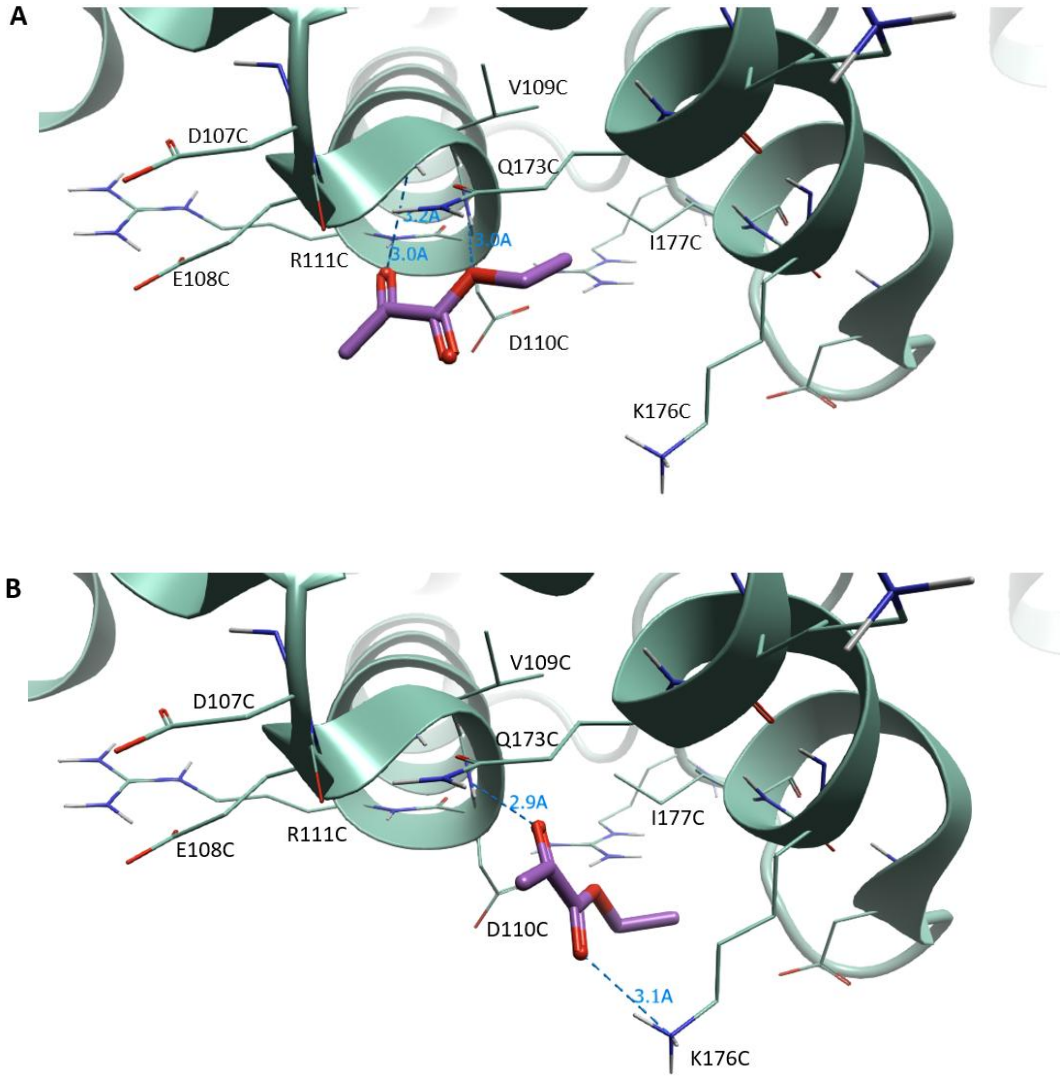

Figure 49. EP poses 1 (a) and 4 (b) docked into pocket 3.

E4ClAA's binding energies for pocket 3 (Table 16 in the Appendix) are greater than those for EP and 2,3-PD, as is typical, but they are lower than E4ClAA's binding energies for pockets 1 and 2. None of E4ClAA's poses exhibit hydrogen bonds with K176C, unlike EP and 2,3-PD. Poses 1 (Figure 57 in the Appendix), 4, and 5 exhibit steric clashes with Q173C. Pose 4 exhibits an additional steric clash between the chlorine atom and D107C, which was not observed for any other poses or substrates. In poses 1, 4, and 5, both carbonyls hydrogen bond with V109C,

D110C, and R111C. In poses 2 and 3, the reactive carbonyl and the ester alkoxy group form hydrogen bonds with these residues, preventing the steric clash with Q173C. E4ClAA is less contorted in pocket 3 compared to the other two pockets, with pose 1 representing the most linear pose.

2,3-PD's binding energies for pocket 3 (Table 17 in the Appendix) are similar to EP's. In pose 5, 2,3-PD forms a hydrogen bond with K176C. Poses 2, 3, and 4 exhibit steric clashes with Q173C. In poses 1 (Figure 58 in the Appendix), 2, and 3, both carbonyls point toward the α-helix containing V109C, D110C, and R111C. In poses 4 and 5, only one carbonyl points toward this α-helix. Pose 1 is the most linear pose.

Discussion

Purification

SDS-PAGE indicates that AKR 308 was sufficiently purified. Eluting fractions 2 and 3 produced a single band with a size of approximately 68 kDa, and concentrated AKR 308 was slightly larger in size than concentrated AKR 163. The size of the Ara1 monomer is 40 kDa,[75] and the size of Ydl124w is 36 kDa.[59] GST-fused AKR 308 and AKR 163 have molecular weights of 68 kDa and 64 kDa, respectively. Therefore, the molecular mass of the isolated enzyme is consistent with GST-tagged AKR 308.

Two additional bands were produced for concentrated AKR 308 and AKR 163, indicating that these protein samples are not completely pure. One band is between 25 kDa and 37 kDa in size, and the other band is between 37 and 50 kDa in size. There are a few possibilities that could explain these contaminating bands. First, several publications reported observing a band

corresponding to a 39 kDa Ara1 degradation product.[72,75,76] Cleavage of Ara1 to form this degradation product occurs at the N-terminal end,[76] which is the site of GST tag fusion. The GST tag is 26 kDa in size, so N-terminal cleavage of AKR 308 would produce fragments with sizes corresponding to the contaminating bands. However, the AKR 308 degradation product would have needed to bind to glutathione in order to appear in the eluting fractions. While N-terminal cleavage would not explain the contaminating bands observed for AKR 163, it is plausible that these bands may simply be spill-over from the AKR 308 lane. Another possibility is that the column may have contained leftover TEV protease, which was used previously to cleave the GST tag from AKR 163. The band between 37 and 50 kDa in size could also correspond to a bacterial protein that binds glutathione. Finally, the contaminating bands might represent protein samples that degraded during the heating process. Although these contaminating bands may be a minor cause for concern, concentrated AKR 308 still produced a band of the appropriate size that was much darker than the contaminating bands, indicating purification of this enzyme to a sufficient degree for experimental studies.

Substrate Specificity

Substrates Without Electron-Withdrawing Groups: The Impact of Steric Bulk

While AKR 308 and AKR 163 display similar kinetic parameters for EAA, they have different tolerance levels for increasing steric bulk. AKR 163 displays lower k_{cat}, K_M, and efficiency values with E2MAA compared to EAA,[5] and it does not appear to catalyze E2EAA reduction. These findings imply that AKR 163 prefers β-keto esters with less branching, or more generally, β-keto esters with less steric bulk. In contrast, AKR 308 displays a higher k_{cat} value,

lower K_M value, and higher efficiency value with E2EAA than with EAA. Thus, while AKR 163 only displays an increase in substrate binding affinity with bulkier substrates, AKR 308 displays an increase in both substrate binding affinity and catalytic activity, producing higher efficiency values for bulkier substrates. In other words, AKR 308 prefers β-keto esters with more extensive branching. However, this assumption is complicated by the findings for AKR 308-catalyzed E2MAA reduction. While the higher velocities relative to EAA reduction suggest a greater k_{cat} value compared to EAA, the linearity of the velocity plot suggests a larger K_M value compared to EAA and E2EAA. One would need to examine higher concentrations of E2MAA in order to confirm the kinetic parameters.

There is only one example in the literature of Ara1 reducing a branched compound with quantitative activity data. Nakamura et al.[84] compared reduction of ethyl 2-oxobutanoate (Figure 50a) and ethyl 3-methyl-2-oxobutanoate (Figure 50b) by YKER-V, which was later confirmed to be Ara1[85]. YKER-V's activity with ethyl 2-oxobutanoate was 31% of its activity with ethyl pyruvate, while its activity with ethyl 3-methyl-2-oxobutanoate was 7% of its activity with ethyl pyruvate. Nakamura et al. also determined the k_{cat} and K_M values of YKER-V-catalyzed reduction of ethyl pyruvate, ethyl 2-oxohexanoate (Figure 50c), and ethyl 3-methyl-2-oxobutanoate. While ethyl 3-methyl-2-oxobutanoate's k_{cat} value (37.0 s^{-1}) was slightly higher than the other substrates (30.5 s^{-1} and 27.8 s^{-1}), its K_M value (79.4 mM) is much greater than the other substrates (5.06 mM and 5.72 mM), indicating slightly higher catalytic power but much poorer binding affinity. An increase in k_{cat} with increasing steric bulk was also observed in this study. On the other hand, while the decrease in binding affinity aligns with the apparently high K_M value for E2MAA, it contradicts the lower K_M value for E2EAA compared to EAA. It is

important to note, however, that ethyl 3-methyl-2-oxobutanoate is an α-keto ester, and the bulky substrates examined in this study are β-keto esters.

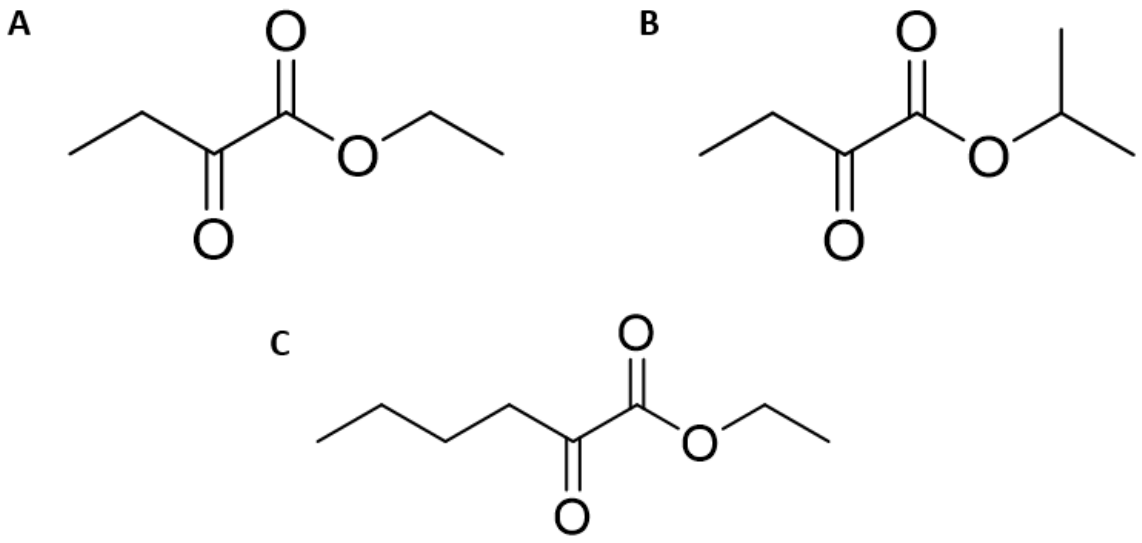

Figure 50. Structures of (a) ethyl-2-oxobutanoate, (b) ethyl-3-methyl-2-oxobutanoate, and (c) ethyl 2-oxohexanoate.

One other consideration with regard to steric bulk is the effect of increasing chain length, which was not examined in this study. According to the literature, Ara1 appears to better tolerate increased chain length than branching, although studies have not examined increasing the chain length of β-keto esters specifically. For example, YKER-V-catalyzed ethyl pyruvate reduction had a k_{cat} value of 30.5 s^{-1} and a K_M value of 5.06 mM, and YKER-V-catalyzed ethyl-2-oxo-hexanoate reduction had a k_{cat} value of 27.8 s^{-1} and a K_M value of 5.72 mM.[84] The decreases in k_{cat} and K_M are minimal despite a five-carbon increase in chain length. Ara1 also displays similar activity levels[86] and kinetic parameters[72] with 2,3-pentanedione and 2,3-hexanedione.

Interestingly, Ara1's efficiency values for its physiological substrates increase from 0.30 s^{-1} mM^{-1} (methylglyoxal) to 1.41 s^{-1} mM^{-1} (2,3-pentanedione) with increasing chain length.[69]

AKR 163 has been tested with ethyl propionyl acetate[5] (Figure 51a) and ethyl 3-oxohexanoate (Figure 51b; Goldman and Cassano, unpublished data), which are β-keto esters with longer chain lengths than EAA. Similar to the branched substrates, k_{cat} and K_M both decreased with increasing chain length. It would be of interest to examine the AKR 308-catalyzed reduction of these substrates in order to determine whether AKR 308 prefers increasing chain length as well as more extensive branching.

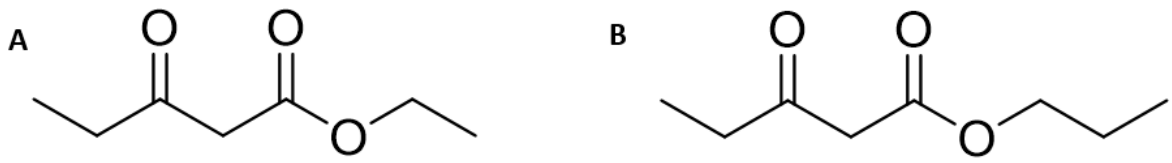

Figure 51. Structures of (a) ethyl propionyl acetate and (b) ethyl 3-oxohexanoate.

The docking results provide some insight into AKR 308's preference for E2EAA over EAA. Compared to all of E2EAA's poses, E2EAA's catalytic pose has the highest free energy as well as the third-highest Rank Score. In contrast, EAA exhibits four noncatalytic poses with higher Rank Scores and binding affinity than the catalytic pose. E2EAA also exhibits more van der Waals interactions with AKR 308's residues compared to EAA, which likely explains its increased binding affinity.

Kinetic Parameters of Electron-Withdrawing Substrates

There are some intriguing differences in AKR 163's and AKR 308's k_{cat} and K_M values for substrates with electron-withdrawing substituents (E4ClAA, E2FAA, EP, and 2,3-PD). In general, AKR 308 exhibited higher k_{cat} and K_M values than AKR 163, indicating that it reduces substrates with a higher catalytic turnover number. The increase in K_M may simply reflect the increase in k_{cat} rather than a decrease in binding affinity. The discrepancy in K_M values is greater than the discrepancy in k_{cat} values. For example, AKR 308's k_{cat} value for E4ClAA is 25% higher than AKR 163's k_{cat} value for E4ClAA, but AKR 308's K_M for E4ClAA is 20 times greater than AKR 163's K_M for E4ClAA. This large discrepancy in K_M values was not observed for EAA, as AKR 308's K_M for this substrate was only three times greater than AKR 163's K_M.

The substitution of the halogen in E2FAA versus E4ClAA also affected binding affinity to a greater extent for AKR 308 than for AKR 163. E2FAA is branched, while E4ClAA is straight-chained. Therefore, it is possible that the branching of E2FAA is the cause of the higher K_M for AKR 308 compared to E4ClAA. On the other hand, AKR 163 may better tolerate E2FAA's branching. This would align with Nakamura et al.'s findings regarding ethyl 3-methyl-2-oxobutanoate[84] as well as E2MAA's apparently high K_M value, but it does not align with the present study's findings regarding EAA and E2EAA, where K_M decreased with more extensive branching. One potential explanation is that branching of halogen substituents may have a different effect than branching of alkyl substituents. Investigations of other substrates containing branched halogen substituents would be necessary to confirm this.

Previous studies have explored the reduction of 2,3-PD by Ara1. van Bergen et al.[69] reported a K_M of 4.2 mM and a k_{cat} of 5.9 s^{-1} for 2,3-PD, and Calam et al.[72] reported a K_M of 2.2 mM and a k_{cat} of 6.4 s^{-1} for 2,3-PD. The k_{cat} of AKR 308 for 2,3-PD is 7 s^{-1}, which is close to the literature values. However, the K_M of AKR 308 for 2,3-PD is 80 mM, which is much higher than the literature values and likely exceeds the 2,3-PD concentration *in vivo*. The discrepancy may have been caused by pH; van Bergen et al. and Calam et al. both used buffers with a pH of 7, whereas the current study used a buffer with a pH of 8. The high background absorbance of 2,3-PD might also have distorted the rate measurements. Furthermore, 2,3-PD was difficult to pipet due to its viscosity, so inaccurate concentrations may have been produced during the serial dilution process. Regardless, 2,3-PD exhibited the highest k_{cat} out of all of the substrates tested, which is consistent with its role as AKR 308's physiological substrate.

Nakamura et al.[84] report kinetic parameters for the reduction of EP by YKER-V and YKER-IV (which Ishihara et al.[59] hypothesize is Ydl124w). YKER-V's K_M for EP reduction was 5.06 mM, and the k_{cat} was 30.5 s^{-1}. By comparison, the K_M value for AKR 308-catalyzed reduction of EP was 6.7 mM, and the k_{cat} was 1.5 s^{-1}. While the K_M values agree, the k_{cat} for AKR 308 is much lower than what the literature reports. Nakamura et al. did not observe substrate inhibition or cooperativity for Ara1-catalyzed EP reduction, which may explain the discrepancy. Additionally, calculation of AKR 308's k_{cat} did not account for substrate inhibition due to the complexity of Equation 4, so it does not reflect the actual turnover number for AKR 308-catalyzed EP reduction. Nakamura et al. also used buffers with a pH of 7 and did not use an affinity tag in their purification of YKER-V, which could also contribute to the difference in kinetic behavior. Interestingly, Nakamura et al. also found that the K_M for the reduction of EP by

YKER-IV was 0.434 mM, which is almost identical to the value of 0.38 mM determined for AKR 163. The lower K_M for YKER-IV compared to YKER-V is consistent with the present study's findings regarding the K_M values for AKR 163 compared to AKR 308. Nakamura et al. also obtained a k_{cat} value of 1.66 s^{-1} for the YKER-IV-catalyzed reduction of EP, which is similar to the k_{cat} value of 2.5 s^{-1} obtained by Akbary et al.[5] Nakamura et al.'s k_{cat} values imply that Ara1 has a larger k_{cat} for EP reduction compared to Ydl124w, which was not the case in the present study. However, this discrepancy might also result from the presence of cooperativity and substrate inhibition in the present study as well as the calculation of k_{cat} from Equation 3.

β-Diketones: Poor Substrates

As kinetic investigations expanded to the α-diketone 2,3-PD, it became of interest to evaluate AKR 308's behavior with β-diketones as well. 2,4-PD was chosen due to its structural similarity to 2,3-PD, and TF-2,4-PD was selected because it is a dicarbonyl with an electron-withdrawing substituent, similar to EP. Both 2,4-PD and TF-2,4-PD were exceptionally poor substrates with limited reactivity. AKR 308's velocity with 15 mM 2,3-PD greatly exceeded its velocities with 125 mM 2,4-PD and 164 mM TF-2,4-PD. 2,4-PD and TF-2,4-PD were also less reactive than EAA, AKR 308's poorest β-keto ester substrate. Thus, β-diketones are worse substrates for AKR 308 than α-diketones and β-keto esters. A study of Ara1 by Heidlas and Tressl[86] aligns with this finding. Compared to baseline activity with diacetyl, Ara1 displayed 151% relative activity with 2,3-PD, 39% relative activity with EAA, and 5% relative activity with 2,4-PD.

α-diketones like 2,3-PD contain two adjacent carbonyls, so the reactive carbonyl is adjacent to an electron-withdrawing group that increases its reactivity. Like β-diketones, a β-keto ester like EAA lacks an electron-withdrawing group adjacent to the reactive carbonyl. However, EAA does contain an electron-withdrawing ester functionality. In this case, the ester functionality in EAA may function as a stronger electron-withdrawing group than the second carbonyl in β-diketones, increasing the reactivity of EAA compared to 2,4-PD and TF-2,4-PD.

The docking results for 2,4-PD offer a structural basis for its low reactivity that supplements the above hypothesis. 2,4-PD's catalytic pose exhibits steric clashes with NADPH and W102, and noncatalytic poses of 2,4-PD have higher Rank Scores than the catalytic pose, indicating that the catalytic pose is unlikely to be observed experimentally.

TF-2,4-PD represents a more perplexing case than 2,4-PD, as one would expect the three fluorine atoms to act as an electron-withdrawing group that increases reactivity. It is important to note, however, that the reactive carbonyl in TF-2,4-PD's catalytic pose is 4.1 Å away from NADPH, which represents the longest distance to NADPH among the catalytic poses. Unlike the other substrates, the nonreactive carbonyl in TF-2,4-PD is closer to NADPH compared to the reactive carbonyl. The longer distance would make hydride transfer from NADPH less efficient, leading to slower catalysis.

Substrate Inhibition

AKR 308 displayed markedly different patterns in substrate inhibition compared to AKR 163. Substrate inhibition was observed with E4ClAA, E2FAA, and EP but not with EAA and other substrates lacking electron-withdrawing groups.[5] This pattern suggested that an electron-

withdrawing group adjacent to the reduced carbonyl induced substrate inhibition in AKR 163. Because lower K_M values were observed for E4ClAA, E2FAA, and EP compared to EAA, it was hypothesized that the electron-withdrawing substituent increases the rate of hydride transfer, allowing the substrate to bind to the enzyme-$NADP^+$ complex and induce substrate inhibition. In contrast, only EP induced substrate inhibition in AKR 308, with E4ClAA and E2FAA exhibiting Michaelis-Menten kinetics. This suggests that AKR 308 does not follow the mechanism of substrate inhibition proposed for AKR 163. Because both EP and 2,3-PD contain a 2,3-dicarbonyl functional group, 2,3-PD was tested with AKR 308 to determine whether substrate inhibition is general for this functional group. A linear increase in velocity was observed up to 15 mM 2,3-PD. While saturation of AKR 308 with 2,3-PD could not be achieved due to high background absorbance, it is evident that substrate inhibition would occur, if at all, at 2,3-PD concentrations that are not biologically or practically relevant. This behavior contrasts with EP, as substrate inhibition was observed at concentrations greater than 10 mM. Thus, for AKR 308, substrate inhibition is not a function of electron-withdrawing substituents or of the 2,3-dicarbonyl functionality. Interestingly, EP does exhibit the lowest K_M value out of all of the substrates tested with AKR 308, which is consistent with the observed correlation between lower K_M values and substrate inhibition for AKR 163.

AKR 163's kinetic behavior with 2,3-PD also provides implications for the model of AKR 163's substrate inhibition. As a 2,3-diketone, 2,3-PD does contain an electron-withdrawing group next to the reduced carbonyl. 2,3-PD exhibited a lower K_M than EAA but a higher K_M than E4ClAA, E2FAA, and EP. While 2,3-PD may exhibit substrate inhibition of AKR 163, this inhibition is far less potent than for the other three substrates with electron-withdrawing groups,

if it occurs at all. 2,3-PD contains a weaker electron-withdrawing group since it lacks the ester functionality, which may explain both the observed K_M and the apparent lack of substrate inhibition. If the kinetic model for 2,3-PD was confirmed to be Michaelis-Menten after testing of higher 2,3-PD concentrations, this would indicate that either the 2,3-diketone functionality is not potent enough to induce inhibition or that substrate inhibition is not a general feature of electron-withdrawing substituents for AKR 163, which would be consistent with AKR 308.

Fluorescence data for AKR 308-$NADP^+$ complex formation provides further insight into the mechanism of AKR 308's substrate inhibition. AKR 308's K_D value for $NADP^+$ binding is 1.2 ± 0.2 μM. Previous researchers found that AKR 163's K_D value for $NADP^+$ binding in one trial was 0.5 ± 0.1 μM (Stafford and Cassano, unpublished data). The difference in K_D values is small, and fluorescence titrations of AKR 163 would need to be repeated in order to confirm this result. However, the larger K_D value for AKR 308 does suggest slightly lower binding affinity for $NADP^+$, which is consistent with the hypothesis that AKR 308's substrate inhibition is not mediated by substrate binding to the enzyme-$NADP^+$ complex. The larger K_D value would indicate faster dissociation of the AKR 308-$NADP^+$ complex after hydride transfer. As a result, substrate molecules would not have enough time to bind to the AKR 308-$NADP^+$ complex following hydride transfer, preventing them from causing substrate inhibition.

Docking studies suggest that rather than binding to the enzyme-$NADP^+$ complex, EP adopts nonproductive poses in the active site that lead to substrate inhibition. EP exhibits two nonproductive poses (3 and 5) with higher free energies and Rank Scores than the catalytic pose. In other words, these poses are more likely to be observed experimentally than the catalytic pose, and they have higher binding affinity than the catalytic pose. In addition, poses 3 and 5 do not

exhibit any steric clashes. It is plausible that at higher concentrations, EP may favor pose 3 or pose 5 over the catalytic pose, forming a dead-end complex that cannot proceed to catalysis. Poses 3 and 5 would also dissociate more slowly from the dead-end complex because they have a higher binding affinity than the catalytic pose, which would mean that the nonproductive complex would dominate over the catalytic complex.

E4ClAA and 2,3-PD are more likely to adopt catalytic poses compared to EP. E4ClAA poses 2, 4, and 6 exhibit similar Rank Scores and binding affinities to the catalytic pose. However, these noncatalytic poses are disfavored due to steric clashes with NADPH. In pose 2, a large chlorine atom is next to NADPH, and in poses 4 and 6, carbon groups are in close proximity to NADPH. In contrast, the catalytic pose is twisted so that the ester portion hydrogen bonds with W132 and does not come in contact with NADPH. Additionally, four of 2,3-PD's poses are catalytic in nature, indicating that 2,3-PD is more likely to adopt a catalytic pose than a noncatalytic pose. Thus, E4ClAA and 2,3-PD would not be expected to adopt nonproductive poses in AKR 308's active site, which could explain why these substrates do not inhibit AKR 308.

One caveat to the proposed model of AKR 308's substrate inhibition is that EAA and 2,4-PD also exhibit noncatalytic poses that have greater Rank Scores and binding affinities than the catalytic pose and lack steric clashes, yet these substrates do not inhibit AKR 308. In this case, more favorable formation of noncatalytic poses may be linked to these substrates' low reactivity. It is also important to note that the concentrations of EAA tested do not approach the K_M value, so the possibility of substrate inhibition cannot be excluded.

There are two noteworthy examples in the literature of substrate inhibition in AKRs that relate to the models described above. Based on studies of the inhibitors zopolrestat and sorbinil, Nakano and Petrash[62] proposed that human aldose reductase (AKR1B1) is inhibited by substrate binding to the enzyme-$NADP^+$ complex, which is consistent with the model of AKR 163's inhibition. For the human steroid 5β reductase AKR1D1, on the other hand, substrate inhibition is mediated by binding of substrates in nonproductive poses. AKR1D1 exhibits substrate inhibition with C18 and C19 steroids such as testosterone but not with C21 steroids such as cortisone.[63] An analysis of the AKR1D1 crystal structure revealed that testosterone adopted a nonproductive binding orientation at the high substrate concentrations used for crystallization, while cortisone did not.[87] This mechanism aligns with the trends observed in the docking poses of EP, E4ClAA, and 2,3-PD in Ara1's active site. Notably, AKR1D1 lacks the "safety belt" found in AKR1B1 that locks cofactor into place,[87] which would decrease AKR1D1's affinity for cofactor and make substrate binding to the enzyme-$NADP^+$ complex less likely. Similarly, fluorescence data indicates that AKR 308 has a lower affinity for $NADP^+$ compared to AKR 163.

To further investigate the role of "safety belt" formation in AKR 163's and AKR 308's inhibition, the AKR1B1 sequence was aligned with the AKR 163 and AKR 308 sequences (Figure 52). Orange shading denotes alignment of the AKR 163 and AKR 308 sequences with the "safety belt" sequence in AKR1B1. For AKR 163, A216 aligns with A221 in the "safety belt" (Figure 52a). There are also three instances where biochemically similar amino acids align: AKR 163 K213 with AKR1B1 R217, AKR 163 Q218 with AKR1B1 K222, and AKR 163 D220 with AKR1B1 E224. Charges are conserved in two of these cases, indicating conservation of the salt bridges through which the "safety belt" stabilizes cofactor binding[28]. With AKR 308, on the other

hand, the only alignment with the “safety belt” occurs between P241 and AKR1B1 P219 (Figure 52b). Interestingly, there is a gap in the portion of the AKR 308 sequence that aligns with the “safety belt.” Overall, the aligned AKR 163 sequence appears to be more reminiscent of the “safety belt” compared to AKR 308, which could produce increased affinity for $NADP^+$. However, a more comprehensive investigation of the role of the “safety belt” in substrate inhibition would require alignment of more AKR sequences, which was beyond the scope of the present study.

A

Score	Expect	Method	Identities	Positives	Gaps
111 bits(277)	2e-31	Compositional matrix adjust.	87/294(30%)	146/294(49%)	36/294(12%)

```
AKR 1B1   7    LNNGAKMP---ILGLGT--WKSPPGQVT------EAVKVAIDV-GYRHIDCAHVYQNENE  54
               LNNG K+P   I+G GT  +K+     T      E +  A+ + G  HID A +Y+   E
AKR 163   10   LNNGNKIPAIAIIGTGTRWYKNEETDATFSNSLVEQIVYALKLPGIIHIDAAEIYRTYPE  69

AKR 1B1   55   VGVAIQEKLREQVVKREELFIVSKLWCTYHEKGLVKGACQKTLSDLKLDYLDLYLIHWPT  114
               VG A+   L E+   R  +F+  K                  L  +  DY+DLYL+H P
AKR 163   70   VGKALS--LTEK--PRNAIFLTDKYSPQIKMSDSPAEGLDLALKKMGTDYVDLYLLHSP-  124

AKR 1B1   115  GFKPGKEFFPLDESGNVVPSDTNILDTWAAMEELVDEGLVKAIGISNFNHLQVEMILNKP  174
                     F   + +G       ++ + W  ME+L   G  K IG+SNF    ++ IL
AKR 163   125  -------FVSKEANG------LSLEEAWKDMEQLYKSGKAKNIGVSNFAVEDLQRILKVA  171

AKR 1B1   175  GLKYKPAVNQIECHPYLTQEK--LIQYCQSKGIVVTAYSPLGSPDRPWAKPEDPSLLEDP  232
                 + KP VNQIE  P+L  +   + ++CQ   I++ AYSPLG   +  A+ +     E
AKR 163   172  --EVKPQVNQIEFSPFLQNQTPGIYKFCQEHDILLEAYSPLGPLQKKTAQDDSQPFFE--  227

AKR 1B1   233  RIKAIAAKHNKTTAQVLIRFPMQRNLVVIPKSVTPERIAENFKVFDFELSSQDM  286
                +K ++ K+ K+ AQ+++R+  +R ++ +  S  P+RI++   +F F+L+++++
AKR 163   228  YVKELSEKYIKSEAQIILRWVTKRGVLPVTTSSKPQRISDAQNLFSFDLTAEEV  281
```

B

Score	Expect	Method	Identities	Positives	Gaps
171 bits(432)	3e-55	Compositional matrix adjust.	107/284(38%)	170/284(59%)	28/284(9%)

```
AKR 1B1   7    LNNGAKMPILGLGTWKSPPGQVTE---AVKVAIDVGYRHIDCAHVYQNENEVGVAIQEKL  63
               LNNG ++P LGLGT  +P  ++ E   AVK AI  GYRHID A  Y+ E  VG AI+E L
AKR 308   27   LNNGVRIPALGLGT-ANPHEKLAETKQAVKAAIKAGYRHIDTAWAYETEPFVGEAIKELL  85

AKR 1B1   64   REQVVKREELFIVSKLWCTYHEKGLVKGACQKTLSDLKLDYLDLYLIHWPTGFKPGKE--  121
                +  +KRE+LFI +K+W    ++  V  +  ++L  L L+Y+DL L HWP  F+  K+
AKR 308   86   EDGSIKREDLFITTKVWPILWDE--VDRSLNESLKALGLEYVDLLLQHWPLCFEKIKDPK  143

AKR 1B1   122  ------FFPLDESGNVV-PSDTNILDTWAAMEELV---DEGLVKAIGISNFNHLQVEMIL  171
                     P+D+SG  +  +D + L+T+  +E++    ++  V+AIG+SNF+   +E ++
AKR 308   144  GISGLVKTPVDDSGKTMYAADGDYLETYKQLEKIYLDPNDHRVRAIGVSNFSIEYLERLI  203

AKR 1B1   172  NKPGLKYKPAVNQIECHPYLTQEKLIQYCQSKGIVVTAYSPLGSPDRPWAKPEDPSLLED  231
                +   + KP VNQ+E HP+L Q +L ++C    I++TAYSPLGS   P         L+
AKR 308   204  KE--CRVKPTVNQVETHPHLPQMELRKFCFMHDILLTAYSPLGSHGAPN--------LKI  253

AKR 1B1   232  PRIKAIAAKHNKTTAQVLIRFPMQRNLVVIPKSVTPERIAENFK  275
               P +K +A K+N T   +LI + +++  +VIP+S+ P RI+ + +
AKR 308   254  PLVKKLAEKYNVTGNDLLISYHIRQGTIVIPRSLNPVRISSSIE  297
```

Figure 52. Alignments of the AKR1B1 sequence with a) AKR 163 and b) AKR 308. Orange shading marks the alignment with AKR1B1's "safety belt" sequence.

Substrate inhibition has not been previously reported for Ara1. The lack of substrate inhibition with 2,3-PD is consistent with the literature.[69,72] However, while substrate inhibition was observed with EP in the present study, Nakamura et al.[84] did not mention substrate inhibition in their description of YKER-V-catalyzed EP reduction (although they do note that substrate inhibition of YKER-IV occurred at α-keto ester concentrations greater than 1 mM). Nakamura et al. did not state the concentrations of EP that they tested, so it is possible that they did not test EP concentrations above 10 mM and therefore would not have observed inhibition. Thus, the findings from the present study regarding substrate inhibition fill a gap in the literature and improve the scientific understanding of substrate inhibition in AKRs.

Cooperativity

One unexpected result from the present study was the observation that EP exhibits cooperative binding with AKR 308. In contrast to the other substrates tested, the velocity curve for EP is distinctly sigmoidal. Because Ara1 is dimeric,[77] cooperative binding is a logical possibility. In addition, because cooperative binding was not observed for E4ClAA, E2FAA, or 2,3-PD, cooperativity is not a function of electron-withdrawing substituents or a 2,3-dicarbonyl functionality. Interestingly, the Hill coefficient for EP is 3.9, which indicates the presence of four binding sites. This finding is not consistent with Ara1's dimeric structure. One possible explanation involves the dimerization of the GST tag,[88] which could lead to tetramer formation. GST tag dimerization could also explain why Nakamura et al.[84] did not observe cooperativity with YKER-V, as they did not include affinity tags in their purification process. It is also possible that the Hill coefficient is an overestimate resulting from the use of Equation 3, which does not account for the effect of substrate inhibition and therefore underestimates V_{max} and K_M.

Cooperativity has not been previously reported for Ara1, but there are other examples of oxidoreductases that exhibit this phenomenon. Two examples are 11β-hydroxysteroid dehydrogenase 1 (11β-HSD1) and cis-retinol/androgen dehydrogenase (CRAD) isoforms 1 and 2. These enzymes belong to the short-chain dehydrogenase superfamily, which catalyzes carbonyl oxidations and reductions via a different mechanism than AKRs. Therefore, these examples are meant to illustrate biological functions of cooperativity in oxidoreductases rather than mechanistic principles. The dimeric 11β-HSD1 exhibits cooperative behavior with cortisone and dehydroxycortisone as substrates but not with cortisol and dehydroxycortisol as substrates.[89] 11β-HSD1 reduces cortisone to cortisol *in vivo*, so this enzyme's cooperative behavior in the reduction direction likely enables an effective response to fluctuations in glucocorticoid levels. On the other hand, 11β-HSD1 does not function as a cortisol dehydrogenase, which would explain its Michaelis-Menten kinetics with this substrate. 11β-HSD1 also exhibits cooperative behavior in the reduction of the carcinogenic cigarette component NNK[90] as well as the reduction of the chemotherapeutic drug oracin to both of its enantiomers.[91] The tetrameric CRAD-1 exhibits cooperative behavior for the oxidation of 9-*cis*-retinol and 11-*cis*-retinol to their corresponding retinals, but it exhibits Michaelis-Menten kinetics for the oxidation of 3α-hydroxysteroids like androsterone.[92] On the other hand, CRAD-2 exhibits cooperative behavior for the oxidation of the 3α-hydroxysteroid testosterone but Michaelis-Menten kinetics for retinols.[93] Because the actions of 3α-hydroxysteroids and retinoic acids oppose each other,[92] the contrasting cooperative behaviors of the two isozymes may serve a regulatory role.

There are also examples of cooperativity within the aldo-keto reductase superfamily. For example, a cytosolic human liver AKR metabolized the HIV integrase inhibitor S-1360 in a

cooperative manner.[94] This AKR was most likely a member of the AKR1C family. Because AKR1C enzymes are monomeric, the cooperative behavior was most likely facilitated by allosteric site binding rather than conformational changes at multiple active sites. Additionally, TcAKR from the parasite *Trypanosoma cruzi* exhibits Michaelis-Menten kinetics with 4-nitrobenzaldehyde and 2-dihydroxyacetone but exhibits cooperative behavior with orthoquinones.[95] The authors cite a unique catalytic mechanism used for quinone reduction[96] as a potential explanation for this observation.

These examples provide some insight into potential biological roles of AKR 308's cooperativity. Ara1's physiological function involves metabolizing toxic diketones,[69] consistent with a general role of AKRs in stress responses.[38,40] Cooperative behavior would allow Ara1 to adjust its activity based on fluctuating diketone concentrations associated with stress; catalytic activity would be lower in basal conditions and would increase in more stressful conditions. This behavior would be similar to what has been observed for 11β-HSD1.[89] The oxidoreductases described above also display both cooperative and Michaelis-Menten behavior depending on the substrate, similar to AKR 308. The implication is that AKR 308 would be more likely to exhibit cooperative behavior with its physiological substrates, but this is inconsistent with the finding that AKR 308 displays Michaelis-Menten kinetics with 2,3-PD as well as the literature on Ara1-catalyzed 2,3-PD reduction. However, it is possible that AKR 308 may exhibit cooperative behavior with diacetyl and methylglyoxal, Ara1's other biological substrates. Additionally, the enzymes described above display cooperative behavior with xenobiotic substrates, which represent potential stressors and which would only demand high catalytic activity at high concentrations. Interestingly, ethyl pyruvate exhibited anti-microbial activity against pathogenic

yeast species,[97] indicating that it could serve as an external stressor. It is also notable that orthoquinones contain two adjacent carbonyl groups,[95] similar to EP. However, this observation does not account for the Michaelis-Menten kinetics observed for 2,3-PD with AKR 308.

Studies of perakine reductase[98] from *Rauvolfia serpentina* and AKRtyl[99] from *Streptomyces fradiae* describe structural mechanisms of cooperativity in AKRs. The monomeric perakine reductase undergoes an extensive conformational change upon NADPH binding that opens a large cavity for substrate binding, leading to cooperative kinetics when the NADPH concentration is varied. This mechanism is likely related to perakine reductase's unique barrel structure, which consists of eight α-helices and six β-strands. The octameric AKRtyl exhibits cooperative behavior with its substrate tylosin. This substrate generates cooperative behavior by binding to an allosteric site, which causes slight conformational changes to the active site that improve tylosin binding. AKRtyl is especially notable, however, because it exhibits both substrate inhibition and cooperative binding with NADPH, similar to AKR 308's behavior with EP. AKRtyl-NADPH crystal structures and fluorescence studies revealed that the binding of NADPH results in a concerted conformational change from a disordered T state to an ordered R state, a model that is consistent with cooperativity. Meanwhile, at high concentrations, NADPH binds to the substrate binding site, resulting in substrate inhibition. While AKRtyl comes closest to matching AKR 308's unique kinetic behavior, AKR 308 appears to be the first example of an AKR exhibiting both substrate inhibition and cooperative binding induced by a carbonyl substrate.

There are two mechanisms by which EP's cooperative binding could occur. In the first mechanism, binding of EP to one active site would generate a conformational change transmitted

across both subunits, improving the affinity of both active sites for EP. This is the mechanism by which aspartate induces cooperativity in aspartate transcarbamoylase.[21] In the second mechanism, binding of EP to an allosteric site would generate a conformational change that improves the affinity of both active sites for EP, similar to the mechanism that tylosin utilizes for cooperative binding to AKRtyl[99]. Examining the first mechanism computationally would require complex molecular dynamics simulations, which were beyond the scope of this study. The second mechanism was examined by generating potential allosteric sites using PASSer and docking EP, E4ClAA, and 2,3-PD into the allosteric sites.

The pockets with the three highest probabilities of being allosteric sites were examined in this study. The binding sites generated for pockets 1 and 2 suggest a potential conformational change that could lead to cooperativity. In pocket 1, substrates docked near a β-sheet that extends to the active site. Hypothetically, substrate binding could shift the β-sheet and produce a conformational change in the active site that improves binding affinity. In pocket 2, two binding sites were located within the dimeric interface. Substrate binding within the dimeric interface has the potential to generate conformational changes in both subunits. In pocket 3, substrate binding would likely alter the three-dimensional arrangement of the outer α-helices, but it is not clear how this would change the active site conformation and produce cooperative behavior. This is consistent with pocket 3 having the lowest probability of being an allosteric site. Molecular dynamics simulations would be required to computationally determine which conformational changes occur upon substrate binding, if any. It is also important to note that analysis of the allosteric pockets does not account for conformational changes induced by the GST tag.

Based on the docking results for EP, E4ClAA, and 2,3-PD, pocket 1 appears most likely to be the allosteric site that facilitates EP's cooperativity. EP exhibits greater binding affinities in pocket 1 than in pockets 2 and 3. All five poses of EP docked into the same position in pocket 1, indicating a consistent binding site. On the other hand, there was slight variation in EP's docking position in pocket 3 and considerable variation in docking position in pocket 2. Remarkably, EP does not exhibit any steric clashes in pocket 1, in contrast to pockets 2 and 3. Binding of EP to pocket 1 also appears to be more favorable than binding of E4ClAA and 2,3-PD to pocket 1. All of E4ClAA's binding poses and three of 2,3-PD's binding poses in pocket 1 exhibit steric clashes. 2,3-PD also binds in two different sites in pocket 1, and E4ClAA's poses in pocket 1 are more contorted than EP's poses.

One important caveat to these findings is that the allostery probabilities for pockets 1, 2, and 3 are less than 50%, and PASSer's Ensemble algorithm only labels a pocket as allosteric if the probability is greater than 50%.[100] According to this definition, the pockets analyzed in this study would not be considered allosteric sites, which means that EP's cooperativity is likely not mediated through allosteric site binding. However, molecular dynamics simulations and experimental studies would be necessary to confirm whether this is true.

Conclusion

This study aimed to compare the kinetic behavior, substrate specificity, and substrate inhibition patterns of AKR 308 and AKR 163, representing the first investigation of an SC108 AKR other than AKR 163. AKR 308 and AKR 163 were found to exhibit significant differences in these areas. For example, AKR 308 displays greater preference for steric bulk and higher K_M

values with substrates containing electron-withdrawing groups compared to AKR 163. Most importantly, AKR 308's substrate inhibition is not general across substrates containing electron-withdrawing groups, as AKR 308 is inhibited by EP but not by E4ClAA, E2FAA, or 2,3-PD. This indicates that AKR 163's mechanism of substrate inhibition is not general across the SC108 AKRs. Fluorescence experiments and substrate docking studies suggest that AKR 308's substrate inhibition may be mediated by nonproductive substrate poses rather than substrate binding to the enzyme-$NADP^+$ complex. AKR 308 exhibits a slightly higher K_D for $NADP^+$ binding compared to AKR 163, indicating that AKR 308 has a lower affinity for $NADP^+$. This would reduce the probability of substrate binding to the enzyme-$NADP^+$ complex. Furthermore, substrate docking predicts nonproductive binding poses for EP that are more energetically favorable and more likely to be observed experimentally than the catalytic pose. On the other hand, E4ClAA's and 2,3-PD's catalytic poses would be expected to dominate over nonproductive poses based on the docking results. Overall, this study represents the first systematic structure-function study of substrate inhibition in AKRs. While reports of substrate inhibition in AKRs focus on sporadic inhibition or inhibition with a biological substrate, this research identifies patterns in substrate inhibition based on carbonyl reactivity and examines how these patterns differ among AKRs.

The most unexpected finding from this study was EP's cooperativity with AKR 308. Like AKR 308's substrate inhibition, cooperativity is not a function of electron-withdrawing groups or 2,3-dicarbonyl functionality. Potential allosteric sites were generated and evaluated computationally to determine if EP's cooperativity is mediated through an allosteric mechanism. Pocket 1 exhibited a consistent EP binding site, lacked steric clashes with EP, and accommodated EP better than E4ClAA and 2,3-PD, suggesting that this pocket could serve as an allosteric

binding site for EP. However, the low allostery probabilities generated through PASSer suggest that EP's cooperativity is not in fact allosteric in nature.

Limitations

There are a number of limitations to this study that should be taken into consideration. With regard to the kinetic experiments, 2,3-PD posed significant problems for data collection. Its high absorbance prevented velocity measurements at concentrations above 15 mM, and its high viscosity could have produced pipetting errors. These factors mean that the possibility of 2,3-PD exerting substrate inhibition cannot be definitively eliminated, and they could explain AKR 308's high K_M value for 2,3-PD, which is not consistent with the literature. Furthermore, the velocity curve for E2MAA was too linear to determine kinetic parameters, which limits the conclusions that can be drawn about AKR 308's preference for steric bulk. Finally, EP's kinetic parameters are inaccurate due to the use of Equation 3, which does not account for substrate inhibition. Use of Equation 3 also means that EP's K_i could not be determined.

The fluorescence experiments also exhibit limitations. First, K_D values for substrate binding could not be determined due to high substrate absorbance in the excitation range. These K_D values would more accurately reflect substrate binding affinity compared to K_M values, and they could have provided insight into AKR 163's and AKR 308's substrate inhibition mechanisms. Additionally, AKR 163's K_D value for $NADP^+$ was obtained from a single trial. to repeat the AKR 163-$NADP^+$ fluorescence titrations were unsuccessful due to abnormally high ΔF values for low $NADP^+$ concentrations that prevented calculation of the K_D value. While AKR

163-$NADP^+$ fluorescence titrations were planned for the present study, they could not be completed due to time constraints.

There are also important caveats to the docking study. First, the LeadFinder algorithm is optimized for drug discovery applications, which involve large molecules with maximized binding affinity for the protein. AKR 308's substrates do not fit in this category. To illustrate, many of the binding energies calculated in this study would be considered "extremely poor binding" according to LeadFinder's criteria.[81] This limits the interpretability of the docking scores. Second, computational docking cannot produce the actual binding pose of the substrate, which would need to be confirmed via experimental techniques like X-ray crystallography or cryo-electron microscopy. The predicted free energies of binding also lack an empirical basis. For example, the K_D value calculated from E4ClAA's catalytic pose's free energy of binding was 0.25 M, which is much higher than the K_M of 10 mM determined experimentally. While the docking results may provide potential explanations for experimental findings, these explanations are speculative and would need to be confirmed experimentally. In cases where experimental and computational findings conflict, the experimental findings should be viewed as more trustworthy. Third, the docking study did not address conformational changes in AKR 308 upon substrate binding. This includes conformational changes in the active site as well as conformational changes across subunits upon binding of EP to the active site or to allosteric sites. More sophisticated molecular dynamics simulations would have revealed additional structural determinants of substrate specificity, and they would have clarified the mechanism that facilitates EP's cooperativity. Fourth, the crystal structures of Ara1 and AKR 308 may not be identical, especially given the differences between Ara1's and AKR 308's behavior.

Future Directions

There are several experiments that could be performed to expand on the findings of the present study. For example, one could evaluate AKR 308's kinetic behavior with additional substrates to better establish its substrate specificity. AKR 308 could be tested with ethyl propionyl acetate and ethyl 3-oxohexanoate in order to determine whether its preference for steric bulk extends to substrates with longer chain lengths. It would also be of interest to evaluate Ara1's physiological substrates diacetyl and methylglyoxal to see if AKR 308 exhibits substrate inhibition or cooperativity with these substrates.

Another unresolved question from the present study is the cause of the Hill coefficient of 3.9 for AKR 308-catalyzed EP reduction. Cross-linking studies with dimethyl suberimidate[101] were performed in order to examine GST tag dimerization and tetramer formation, which could explain the Hill coefficient (Goldman and Cassano, unpublished data). These studies revealed dimerization of the monomeric AKR 163, which was most likely induced by GST tag dimerization, and they provided preliminary evidence of AKR 308 tetramer formation. However, confirming GST tag dimerization would require cleaving the GST tag from AKR 308 and AKR 163. Size-exclusion chromatography could also be performed to investigate AKR 308 oligomer formation.

It would also be of interest to perform a docking study of Ydl124w. Unfortunately, researchers have not yet determined Ydl124w's crystal structure. An AlphaFold structure of Ydl124w has been generated (Cassano, unpublished data), but docking into this structure would likely produce less accurate results compared to docking into the Ara1 crystal structure. NADPH

would also need to be docked into the Ydl124w AlphaFold structure, which proved to be difficult in previous attempts. A docking study of Ydl124w would provide insight into the differences in kinetic parameters between AKR 163 and AKR 308 as well as AKR 163's mechanism of substrate inhibition. If catalytic poses of substrates containing electron-withdrawing groups were favored over nonproductive poses, this would provide further evidence for the hypothesis that AKR 163's and AKR 308's substrate inhibition are mediated through different mechanisms.

One final area of investigation is the other three AKRs cloned from SC108: AKRs 169, 304, and 456. AKR 304, which is homologous to the xylose reductase Gre3,[4] was recently isolated from *E. coli*, and it only exhibited enzymatic activity with xylose as its substrate (Orellana, De'Stefano, and Cassano, unpublished data). The kinetic behaviors of AKR 169 and AKR 456 have not yet been determined. AKR 456 is particularly interesting since it is also homologous to Ara1.[4] Kinetic studies of these AKRs would reveal whether they exhibit substrate inhibition and, by extension, whether they conform more closely to AKR 163's or AKR 308's mechanism of substrate inhibition. This would permit more general conclusions about the mechanisms of substrate inhibition in AKRs.

Implications for Biocatalysis

In addition to comparing the substrate inhibition patterns of AKR 163 and AKR 308, a major motivation for the present study was to evaluate the biocatalytic applications of these enzymes. This research aligns with other screening studies of novel AKRs, which establish the substrate specificity of these enzymes and help researchers select AKRs that are well-suited for certain biocatalytic reactions. Kinetic studies of AKR 163 and AKR 308 revealed that these

enzymes would be optimal for biocatalysis under different conditions. For example, AKR 163 would be well-suited for reduction of E4ClAA and EP at concentrations lower than 1 mM due to its low K_M. On the other hand, AKR 308 would be the more ideal choice for reduction of E4ClAA at concentrations higher than 1 mM because AKR 163 exhibits substrate inhibition at these concentrations. AKR 308-catalyzed EP reduction would be most optimal at concentrations between 3 mM and 10 mM, which corresponds to the exponential portion of the sigmoidal velocity curve. Finally, AKR 308 would be preferred over AKR 163 for reductions of branched compounds. It is also important to note that AKR 163 and AKR 308 would be predicted to differ in their stereoselectivity; Ara1 reduces 2,3-diketones to the (*S*) enantiomer of the alcohol, whereas Ydl124w reduces 2,3-diketones to the (*R*)-enantiomer of the alcohol.

Because substrate inhibition impairs biocatalysis, it is of interest to develop methods to ameliorate this behavior. For AKR 163, one method to alleviate substrate inhibition is the use of low pH and salt ions, which disrupt salt bridge interactions involved in binding of substrate to the enzyme-$NADP^+$ complex. For example, AKR 163-catalyzed E4ClAA reduction at pH 6 in 1 M NaCl produced a velocity curve approximating Michaelis-Menten kinetics.[102] However, this method is less likely to alleviate the substrate inhibition of AKR 308, as this enzyme's inhibition appears to be mediated via formation of nonproductive substrate poses as opposed to substrate binding to the enzyme-$NADP^+$ complex. An alternative approach for AKR 308 may be to mutate residues involved in stabilizing the nonproductive poses of EP, such as A70, K150, and W132. This would then favor formation of EP's catalytic pose over the nonproductive poses, potentially alleviating substrate inhibition.

References

1. Rossino, G.; Robescu, M. S.; Licastro, E.; Tedesco, C.; Martello, I.; Maffei, L.; Vincenti, G.; Bavaro, T.; Collina, S. Biocatalysis: A Smart and Green Tool for the Preparation of Chiral Drugs. *Chirality* **2022**, *34* (11), 1403–1418. https://doi.org/10.1002/chir.23498.

2. Hanefeld, U.; Hollmann, F.; Paul, C. E. Biocatalysis Making Waves in Organic Chemistry. *Chem. Soc. Rev.* **2022**, *51* (2), 594–627. https://doi.org/10.1039/D1CS00100K.

3. Penning, T. M. The Aldo-Keto Reductases (AKRs): Overview. *Chem. Biol. Interact.* **2015**, *234*, 236–246. https://doi.org/10.1016/j.cbi.2014.09.024.

4. Akbary, Z. Ketoreductase Activity of 45-Million-Year-Old Yeast Strains Revived from Amber. Undergraduate Thesis, Drew University, Madison, NJ, 2019.

5. Akbary, Z.; Yu, H.; Lorenzo, I.; Paez, K.; Lee, N. D.; DeBeVoise, K.; Moses, J.; Sanders, N.; Connors, N.; Cassano, A. Electron Withdrawing Group-Dependent Substrate Inhibition of an α-Ketoamide Reductase from *Saccharomyces cerevisiae*. *Biochem. Bioph. Res. Co.* **2023**, *676*, 97–102. https://doi.org/10.1016/j.bbrc.2023.07.030.

6. Brooks, W. H.; Guida, W. C.; Daniel, K. G. The Significance of Chirality in Drug Design and Development. *Curr. Top. Med. Chem.* **2011**, *11* (7), 760–770. https://doi.org/10.2174/156802611795165098.

7. Kirk, O.; Borchert, T. V.; Fuglsang, C. C. Industrial Enzyme Applications. *Curr. Opin. Biotech.* **2002**, *13* (4), 345–351. https://doi.org/10.1016/S0958-1669(02)00328-2.

8. Raju, M. N.; Kumar, N. U.; Reddy, B. S.; Anitha, N.; Srinivas, G.; Bhattacharya, A.; Mukkanti, K.; Kolla, N.; Bandichhor, R. An Efficient Synthesis of Dexlansoprazole Employing

Asymmetric Oxidation Strategy. *Tetrahedron Lett.* **2011**, *52* (42), 5464–5466. https://doi.org/10.1016/j.tetlet.2011.08.033.

9. Liu, F.; Shou, C.; Geng, Q.; Zhao, C.; Xu, J.; Yu, H. A Baeyer-Villiger Monooxygenase from *Cupriavidus basilensis* Catalyzes Asymmetric Synthesis of (R)-Lansoprazole and Other Pharmaco-Sulfoxides. *Appl. Microbiol. Biotechnol.* **2021**, *105* (8), 3169–3180. https://doi.org/10.1007/s00253-021-11230-0.
10. Martinez, C. A.; Hu, S.; Dumond, Y.; Tao, J.; Kelleher, P.; Tully, L. Development of a Chemoenzymatic Manufacturing Process for Pregabalin. *Org. Process Res. Dev.* **2008**, *12* (3), 392–398. https://doi.org/10.1021/op7002248.
11. Savile, C. K.; Janey, J. M.; Mundorff, E. C.; Moore, J. C.; Tam, S.; Jarvis, W. R.; Colbeck, J. C.; Krebber, A.; Fleitz, F. J.; Brands, J.; Devine, P. N.; Huisman, G. W.; Hughes, G. J. Biocatalytic Asymmetric Synthesis of Chiral Amines from Ketones Applied to Sitagliptin Manufacture. *Science* **2010**, *329* (5989), 305–309. https://doi.org/10.1126/science.1188934.
12. Tymoczko, J.; Berg, J.; Gatto, G.; Stryer, L. *Biochemistry: A Short Course*, 4th ed.; W. H. Freeman: New York, NY, 2019.
13. Scholey, J. M. Compare and Contrast the Reaction Coordinate Diagrams for Chemical Reactions and Cytoskeletal Force Generators. *Mol. Biol. Cell* **2013**, *24* (4), 433–439. https://doi.org/10.1091/mbc.e12-07-0545.
14. Robinson, P. K. Enzymes: Principles and Biotechnological Applications. *Essays Biochem* **2015**, *59*, 1–41. https://doi.org/10.1042/bse0590001.
15. Wolfenden, R.; Snider, M. J. The Depth of Chemical Time and the Power of Enzymes as Catalysts. *Acc. Chem. Res.* **2001**, *34* (12), 938–945. https://doi.org/10.1021/ar000058i.

16. Johnson, K. A.; Goody, R. S. The Original Michaelis Constant: Translation of the 1913 Michaelis–Menten Paper. *Biochemistry* **2011**, *50* (39), 8264–8269. https://doi.org/10.1021/bi201284u.

17. Kokkonen, P.; Beier, A.; Mazurenko, S.; Damborsky, J.; Bednar, D.; Prokop, Z. Substrate Inhibition by the Blockage of Product Release and Its Control by Tunnel Engineering. *RSC Chem. Biol.* **2021**, *2* (2), 645–655. https://doi.org/10.1039/D0CB00171F.

18. Yoshino, M.; Murakami, K. Analysis of the Substrate Inhibition of Complete and Partial Types. *SpringerPlus* **2015**, *4* (1), 292. https://doi.org/10.1186/s40064-015-1082-8.

19. Reed, M. C.; Lieb, A.; Nijhout, H. F. The Biological Significance of Substrate Inhibition: A Mechanism with Diverse Functions. *BioEssays* **2010**, *32* (5), 422–429. https://doi.org/10.1002/bies.200900167.

20. Cornish-Bowden, A. Understanding Allosteric and Cooperative Interactions in Enzymes. *FEBS J.* **2014**, *281* (2), 621–632. https://doi.org/10.1111/febs.12469.

21. Lipscomb, W. N.; Kantrowitz, E. R. Structure and Mechanisms of *Escherichia coli* Aspartate Transcarbamoylase. *Acc. Chem. Res.* **2012**, *45* (3), 444–453. https://doi.org/10.1021/ar200166p.

22. Monti, D.; Ottolina, G.; Carrea, G.; Riva, S. Redox Reactions Catalyzed by Isolated Enzymes. *Chem. Rev.* **2011**, *111* (7), 4111–4140. https://doi.org/10.1021/cr100334x.

23. Wu, S.; Snajdrova, R.; Moore, J. C.; Baldenius, K.; Bornscheuer, U. T. Biocatalysis: Enzymatic Synthesis for Industrial Applications. *Angew Chem. Int. Ed.* **2021**, *60* (1), 88–119. https://doi.org/10.1002/anie.202006648.

24. Barski, O. A.; Tipparaju, S. M.; Bhatnagar, A. The Aldo-Keto Reductase Superfamily and Its Role in Drug Metabolism and Detoxification. *Drug Metab. Rev.* **2008**, *40* (4), 553–624. https://doi.org/10.1080/03602530802431439.

25. Huisman, G. W.; Liang, J.; Krebber, A. Practical Chiral Alcohol Manufacture Using Ketoreductases. *Curr. Opin. Chem. Biol.* **2010**, *14* (2), 122–129. https://doi.org/10.1016/j.cbpa.2009.12.003.

26. Kratzer, R.; Wilson, D.; Nidetzky, B. Catalytic Mechanism and Substrate Selectivity of Aldo-Keto Reductases: Insights from Structure-Function Studies of *Candida tenuis* Xylose Reductase. *IUBMB Life* **2006**, *58* (9), 499–507. https://doi.org/10.1080/15216540600818143.

27. Di Luccio, E.; Elling, R. A.; Wilson, D. K. Identification of a Novel NADH-Specific Aldo-Keto Reductase Using Sequence and Structural Homologies. *Biochem. J.* **2006**, *400* (1), 105–114. https://doi.org/10.1042/BJ20060660.

28. Sanli, G.; Dudley, J. I.; Blaber, M. Structural Biology of the Aldo-Keto Reductase Family of Enzymes: Catalysis and Cofactor Binding. *Cell Biochem. Biophys.* **2003**, *38* (1), 79–101. https://doi.org/10.1385/CBB:38:1:79.

29. Jez, J. M.; Bennett, M. J.; Schlegel, B. P.; Lewis, M.; Penning, T. M. Comparative Anatomy of the Aldo–Keto Reductase Superfamily. *Biochem. J.* **1997**, *326* (3), 625–636. https://doi.org/10.1042/bj3260625.

30. Borhani, D. W.; Harter, T. M.; Petrash, J. M. The Crystal Structure of the Aldose Reductase·NADPH Binary Complex. *J. Biol. Chem.* **1992**, *267* (34), 24841–24847. https://doi.org/10.1016/S0021-9258(18)35840-X.

31. Campbell, E.; Chuang, S.; Banta, S. Modular Exchange of Substrate-Binding Loops Alters Both Substrate and Cofactor Specificity in a Member of the Aldo-Keto Reductase Superfamily. *Protein Eng. Des. Sel.* **2013**, *26* (3), 181–186. https://doi.org/10.1093/protein/gzs095.

32. Ratnam, K.; Ma, H.; Penning, T. M. The Arginine 276 Anchor for NADP(H) Dictates Fluorescence Kinetic Transients in 3α-Hydroxysteroid Dehydrogenase, a Representative Aldo−Keto Reductase. *Biochemistry* **1999**, *38* (24), 7856–7864. https://doi.org/10.1021/bi982838t.

33. Bohren, K. M.; Grimshaw, C. E.; Lai, C. J.; Harrison, D. H.; Ringe, D.; Petsko, G. A.; Gabbay, K. H. Tyrosine-48 Is the Proton Donor and Histidine-110 Directs Substrate Stereochemical Selectivity in the Reduction Reaction of Human Aldose Reductase: Enzyme Kinetics and Crystal Structure of the Y48H Mutant Enzyme. *Biochemistry* **1994**, *33* (8), 2021–2032. https://doi.org/10.1021/bi00174a007.

34. Schlegel, B. P.; Jez, J. M.; Penning, T. M. Mutagenesis of 3α-Hydroxysteroid Dehydrogenase Reveals a “Push−Pull” Mechanism for Proton Transfer in Aldo−Keto Reductases. *Biochemistry* **1998**, *37* (10), 3538–3548. https://doi.org/10.1021/bi9723055.

35. Grimshaw, C. E.; Bohren, K. M.; Lai, C.-J.; Gabbay, K. H. Human Aldose Reductase: Rate Constants for a Mechanism Including Interconversion of Ternary Complexes by Recombinant Wild-Type Enzyme. *Biochemistry* **1995**, *34* (44), 14356–14365. https://doi.org/10.1021/bi00044a012.

36. Cooper, W. C.; Jin, Y.; Penning, T. M. Elucidation of a Complete Kinetic Mechanism for a Mammalian Hydroxysteroid Dehydrogenase (HSD) and Identification of All Enzyme Forms

on the Reaction Coordinate. *J. Biol. Chem.* **2007**, *282* (46), 33484–33493. https://doi.org/10.1074/jbc.m703414200.

37. Akbary, Z.; Yu, H.; Lorenzo, I.; Paez, K.; Lee, N. D.; DeBeVoise, K.; Moses, J.; Sanders, N.; Connors, N.; Cassano, A. Electron Withdrawing Group-Dependent Substrate Inhibition of an Aldo-Keto Reductase from a Yeast Isolated from Ancient Amber; Indianapolis, IN, 2023.
38. Farahyar, S.; Zaini, F.; Kordbacheh, P.; Rezaie, S.; Safara, M.; Raoofian, R.; Heidari, M. Overexpression of Aldo-Keto-Reductase in Azole-Resistant Clinical Isolates of *Candida glabrata* Determined by cDNA-AFLP. *DARU J. Pharm. Sci.* **2013**, *21* (1), 1. https://doi.org/10.1186/2008-2231-21-1.
39. Chang, Q.; Griest, T. A.; Harter, T. M.; Mark Petrash, J. Functional Studies of Aldo-Keto Reductases in *Saccharomyces cerevisiae*. *BBA-Mol. Cell. Res.* **2007**, *1773* (3), 321–329. https://doi.org/10.1016/j.bbamcr.2006.10.009.
40. Chang, Q.; Petrash, J. M. Disruption of Aldo-Keto Reductase Genes Leads to Elevated Markers of Oxidative Stress and Inositol Auxotrophy in *Saccharomyces cerevisiae*. *BBA-Mol. Cell. Res.* **2008**, *1783* (2), 237–245. https://doi.org/10.1016/j.bbamcr.2007.08.008.
41. Petrash, J. M.; Murthy, B. S. N.; Young, M.; Morris, K.; Rikimaru, L.; Griest, T. A.; Harter, T. Functional Genomic Studies of Aldo–Keto Reductases. *Chem. Biol. Interact.* **2001**, *130–132*, 673–683. https://doi.org/10.1016/S0009-2797(00)00258-1.
42. Liang, J.; Lalonde, J.; Borup, B.; Mitchell, V.; Mundorff, E.; Trinh, N.; Kochrekar, D. A.; Nair Cherat, R.; Pai, G. G. Development of a Biocatalytic Process as an Alternative to the (−)-DIP-Cl-Mediated Asymmetric Reduction of a Key Intermediate of Montelukast. *Org. Process Res. Dev.* **2010**, *14* (1), 193–198. https://doi.org/10.1021/op900272d.

43. Gooding, O. W.; Voladri, R.; Bautista, A.; Hopkins, T.; Huisman, G.; Jenne, S.; Ma, S.; Mundorff, E. C.; Savile, M. M.; Truesdell, S. J.; Wong, J. W. Development of a Practical Biocatalytic Process for (*R*)-2-Methylpentanol. *Org. Process Res. Dev.* **2010**, *14* (1), 119–126. https://doi.org/10.1021/op9002246.

44. Penning, T. M.; Drury, J. E. Human Aldo–Keto Reductases: Function, Gene Regulation, and Single Nucleotide Polymorphisms. *Arch. Biochem. Biophys.* **2007**, *464* (2), 241–250. https://doi.org/10.1016/j.abb.2007.04.024.

45. Burczynski, M. E.; Sridhar, G. R.; Palackal, N. T.; Penning, T. M. The Reactive Oxygen Species- and Michael Acceptor-Inducible Human Aldo-Keto Reductase AKR1C1 Reduces the α,β-Unsaturated Aldehyde 4-Hydroxy-2-Nonenal to 1,4-Dihydroxy-2-Nonene. *J. Biol. Chem.* **2001**, *276* (4), 2890–2897. https://doi.org/10.1074/jbc.M006655200.

46. Rižner, T. L.; Šmuc, T.; Rupreht, R.; Šinkovec, J.; Penning, T. M. AKR1C1 and AKR1C3 May Determine Progesterone and Estrogen Ratios in Endometrial Cancer. *Mol. Cell. Endocrinol.* **2006**, *248* (1–2), 126–135. https://doi.org/10.1016/j.mce.2005.10.009.

47. Crosas, B.; Hyndman, D. J.; Gallego, O.; Martras, S.; Parés, X.; Flynn, T. G.; Farrés, J. Human Aldose Reductase and Human Small Intestine Aldose Reductase Are Efficient Retinal Reductases: Consequences for Retinoid Metabolism. *Biochem. J.* **2003**, *373* (3), 973–979. https://doi.org/10.1042/bj20021818.

48. Breyer-Pfaff, U.; Martin, H.-J.; Ernst, M.; Maser, E. Enantioselectivity of Carbonyl Reduction of 4-Methylnitrosamino-1-(3-Pyridyl)-1-Butanone by Tissue Fractions from Human and Rat and by Enzymes Isolated from Human Liver. *Drug Metab. Dispos.* **2004**, *32* (9), 915–922. https://doi.org/10.1016/S0090-9556(24)02973-8.

49. Ireland, L. S.; Harrison, D. J.; Neal, G. E.; Hayes, J. D. Molecular Cloning, Expression and Catalytic Activity of a Human AKR7 Member of the Aldo–Keto Reductase Superfamily: Evidence That the Major 2-Carboxybenzaldehyde Reductase from Human Liver Is a Homologue of Rat Aflatoxin B1-Aldehyde Reductase. *Biochem. J.* **1998**, *332* (1), 21–34. https://doi.org/10.1042/bj3320021.

50. Wsol, V.; Szotakova, B.; Martin, H.; Maser, E. Aldo-Keto Reductases (AKR) from the AKR1C Subfamily Catalyze the Carbonyl Reduction of the Novel Anticancer Drug Oracin in Man. *Toxicology* **2007**, *238* (2–3), 111–118. https://doi.org/10.1016/j.tox.2007.05.021.

51. Ohara, H.; Miyabe, Y.; Deyashiki, Y.; Matsuura, K.; Kara, A. Reduction of Drug Ketones by Dihydrodiol Dehydrogenases, Carbonyl Reductase and Aldehyde Reductase of Human Liver. *Biochem. Pharmaco.* **1995**, *50* (2), 221–227. https://doi.org/10.1016/0006-2952(95)00124-I.

52. Fukumoto, S.; Yamauchi, N.; Moriguchi, H.; Hippo, Y.; Watanabe, A.; Shibahara, J.; Taniguchi, H.; Ishikawa, S.; Ito, H.; Yamamoto, S.; Iwanari, H.; Hironaka, M.; Ishikawa, Y.; Niki, T.; Sohara, Y.; Kodama, T.; Nishimura, M.; Fukayama, M.; Dosaka-Akita, H.; Aburatani, H. Overexpression of the Aldo-Keto Reductase Family Protein AKR1B10 Is Highly Correlated with Smokers' Non–Small Cell Lung Carcinomas. *Clin. Cancer Res.* **2005**, *11* (5), 1776–1785. https://doi.org/10.1158/1078-0432.CCR-04-1238.

53. Hotta, N.; Toyota, T.; Matsuoka, K.; Shigeta, Y.; Kikkawa, R.; Kaneko, T.; Takahashi, A.; Sugimura, K.; Koike, Y.; Ishii, J.; Sakamoto, N.; The SNK-860 Diabetic Neuropathy Study Group. Clinical Efficacy of Fidarestat, a Novel Aldose Reductase Inhibitor, for Diabetic Peripheral Neuropathy. *Diabetes Care* **2001**, *24* (10), 1776–1782. https://doi.org/10.2337/diacare.24.10.1776.

54. Takemura, M.; Endo, S.; Matsunaga, T.; Soda, M.; Zhao, H.-T.; El-Kabbani, O.; Tajima, K.; Iinuma, M.; Hara, A. Selective Inhibition of the Tumor Marker Aldo-Keto Reductase Family Member 1B10 by Oleanolic Acid. *J. Nat. Prod.* **2011**, *74* (5), 1201–1206. https://doi.org/10.1021/np200118q.

55. Kaluzna, I. A.; Matsuda, T.; Sewell, A. K.; Stewart, J. D. Systematic Investigation of *Saccharomyces cerevisiae* Enzymes Catalyzing Carbonyl Reductions. *J. Am. Chem. Soc.* **2004**, *126* (40), 12827–12832. https://doi.org/10.1021/ja0469479.

56. Kaluzna, I. A.; Feske, B. D.; Wittayanan, W.; Ghiviriga, I.; Stewart, J. D. Stereoselective, Biocatalytic Reductions of α-Chloro-β-Keto Esters. *J. Org. Chem.* **2005**, *70* (1), 342–345. https://doi.org/10.1021/jo0484981.

57. Ni, Y.; Li, C.-X.; Ma, H.-M.; Zhang, J.; Xu, J.-H. Biocatalytic Properties of a Recombinant Aldo-Keto Reductase with Broad Substrate Spectrum and Excellent Stereoselectivity. *Appl. Microbiol Biotechnol.* **2011**, *89* (4), 1111–1118. https://doi.org/10.1007/s00253-010-2941-4.

58. Liang, C.; Nie, Y.; Mu, X.; Xu, Y. Gene Mining-Based Identification of Aldo–Keto Reductases for Highly Stereoselective Reduction of Bulky Ketones. *Bioresour. Bioprocess.* **2018**, *5* (1), 33. https://doi.org/10.1186/s40643-018-0220-x.

59. Ishihara, K.; Yamamoto, H.; Mitsuhashi, K.; Nishikawa, K.; Tsuboi, S.; Tsuji, H.; Nakajima, N. Purification and Characterization of α-Keto Amide Reductase from *Saccharomyces cerevisiae*. *Biosci. Biotech. Biochem.* **2004**, *68* (11), 2306–2312.

60. Jung, J.; Park, H. J.; Uhm, K.-N.; Kim, D.; Kim, H.-K. Asymmetric Synthesis of (S)-Ethyl-4-Chloro-3-Hydroxy Butanoate Using a *Saccharomyces cerevisiae* Reductase:

Enantioselectivity and Enzyme–Substrate Docking Studies. *BBA-Proteins Proteom.* **2010**, *1804* (9), 1841–1849. https://doi.org/10.1016/j.bbapap.2010.06.011.

61. Feske, B. D.; Kaluzna, I. A.; Stewart, J. D. Enantiodivergent, Biocatalytic Routes to Both Taxol Side Chain Antipodes. *J. Org. Chem.* **2005**, *70* (23), 9654–9657. https://doi.org/10.1021/jo0516077.

62. Nakano, T.; Petrash, J. M. Kinetic and Spectroscopic Evidence for Active Site Inhibition of Human Aldose Reductase. *Biochemistry* **1996**, *35* (34), 11196–11202. https://doi.org/10.1021/bi9608121.

63. Chen, M.; Drury, J. E.; Penning, T. M. Substrate Specificity and Inhibitor Analyses of Human Steroid 5β-Reductase (AKR1D1). *Steroids* **2011**, *76* (5), 484–490. https://doi.org/10.1016/j.steroids.2011.01.003.

64. Yamamoto, K.; Wilson, D. K. Identification, Characterization, and Crystal Structure of an Aldo–Keto Reductase (AKR2E4) from the Silkworm *Bombyx mori*. *Arch. Biochem. Biophys.* **2013**, *538* (2), 156–163. https://doi.org/10.1016/j.abb.2013.08.018.

65. Kita, K.; Fukura, T.; Nakase, K.-I.; Okamoto, K.; Yanase, H.; Kataoka, M.; Shimizu, S. Cloning, Overexpression, and Mutagenesis of the *Sporobolomyces salmonicolor* AKU4429 Gene Encoding a New Aldehyde Reductase, Which Catalyzes the Stereoselective Reduction of Ethyl 4-Chloro-3-Oxobutanoate to Ethyl (*S*)-4-Chloro-3-Hydroxybutanoate. *Appl. Environ. Microbiol.* **1999**, *65* (12), 5207–5211. https://doi.org/10.1128/AEM.65.12.5207-5211.1999.

66. Zhang, J.; Tao, S.; Zhang, B.; Wu, X.; Chen, Y. Microparticle-Based Strategy for Controlled Release of Substrate for the Biocatalytic Preparation of L-Homophenylalanine. *ACS Catal.* **2014**, *4* (5), 1584–1587. https://doi.org/10.1021/cs4011919.

67. Ma, Y.; Liu, N.; Greisen, P.; Li, J.; Qiao, K.; Huang, S.; Stephanopoulos, G. Removal of Lycopene Substrate Inhibition Enables High Carotenoid Productivity in *Yarrowia lipolytica*. *Nat. Commun.* **2022**, *13* (1), 572. https://doi.org/10.1038/s41467-022-28277-w.

68. Grimshaw, C. E.; Shahbaz, M.; Putney, C. G. Spectroscopic and Kinetic Characterization of Nonenzymic and Aldose Reductase Mediated Covalent NADP-Glycolaldehyde Adduct Formation. *Biochemistry* **1990**, *29* (42), 9936–9946. https://doi.org/10.1021/bi00494a026.

69. Van Bergen, B.; Strasser, R.; Cyr, N.; Sheppard, J. D.; Jardim, A. α,β-Dicarbonyl Reduction by *Saccharomyces* D-Arabinose Dehydrogenase. *BBA-Gen. Subjects* **2006**, *1760* (11), 1636–1645. https://doi.org/10.1016/j.bbagen.2006.08.025.

70. Katz, M.; Hahn-Hägerdal, B.; Gorwa-Grauslund, M. F. Screening of Two Complementary Collections of *Saccharomyces cerevisiae* to Identify Enzymes Involved in Stereo-Selective Reductions of Specific Carbonyl Compounds: An Alternative to Protein Purification. *Enzyme Microb. Tech.* **2003**, *33* (2–3), 163–172. https://doi.org/10.1016/S0141-0229(03)00086-3.

71. González, E.; Fernández, M. R.; Marco, D.; Calam, E.; Sumoy, L.; Parés, X.; Dequin, S.; Biosca, J. A. Role of *Saccharomyces cerevisiae* Oxidoreductases Bdh1p and Ara1p in the Metabolism of Acetoin and 2,3-Butanediol. *Appl. Environ. Microbiol.* **2010**, *76* (3), 670–679. https://doi.org/10.1128/AEM.01521-09.

72. Calam, E.; Porté, S.; Fernández, M. R.; Farrés, J.; Parés, X.; Biosca, J. A. Biocatalytic Production of Alpha-Hydroxy Ketones and Vicinal Diols by Yeast and Human Aldo–Keto Reductases. *Chem. Biol. Interact.* **2013**, *202* (1–3), 195–203. https://doi.org/10.1016/j.cbi.2012.12.006.

73. Kovacic, P.; Cooksy, A. L. Role of Diacetyl Metabolite in Alcohol Toxicity and Addiction via Electron Transfer and Oxidative Stress. *Arch. Toxicol.* **2005**, *79* (3), 123–128. https://doi.org/10.1007/s00204-004-0602-z.

74. Godon, C.; Lagniel, G.; Lee, J.; Buhler, J.-M.; Kieffer, S.; Perrot, M.; Boucherie, H.; Toledano, M. B.; Labarre, J. The H_2O_2 Stimulon in *Saccharomyces cerevisiae*. *J Biol Chem* **1998**, *273* (35), 22480–22489. https://doi.org/10.1074/jbc.273.35.22480.

75. Kim, S.-T.; Huh, W.-K.; Lee, B.-H.; Kang, S.-O. D-Arabinose Dehydrogenase and Its Gene from *Saccharomyces cerevisiae*. *BBA-Protein Struct. M.* **1998**, *1429* (1), 29–39. https://doi.org/10.1016/S0167-4838(98)00217-9.

76. Amako, K.; Fujita, K.; Iwamoto, C.; Sengee, M.; Fuchigami, K.; Fukumoto, J.; Ogishi, Y.; Kishimoto, R.; Goda, K. $NADP^+$-Dependent D-Arabinose Dehydrogenase Shows a Limited Contribution to Erythroascorbic Acid Biosynthesis and Oxidative Stress Resistance in *Saccharomyces cerevisiae*. *Biosci. Biotech. Biochem.* **2006**, *70* (12), 3004–3012. https://doi.org/10.1271/bbb.60399.

77. Hu, X.-Q.; Guo, P.-C.; Ma, J.-D.; Li, W.-F. Structures of *Saccharomyces cerevisiae* D-Arabinose Dehydrogenase Ara1 and Its Complex with NADPH: Implications for Cofactor-Assisted Substrate Recognition. *Acta Crystallogr. F Struct. Biol. Cryst. Commun.* **2013**, *69* (11), 1190–1195. https://doi.org/10.1107/S1744309113026857.

78. Pace, C. N.; Vajdos, F.; Fee, L.; Grimsley, G.; Gray, T. How to Measure and Predict the Molar Absorption Coefficient of a Protein. *Protein Sci.* **1995**, *4* (11), 2411–2423. https://doi.org/10.1002/pro.5560041120.

79. Flare; Cresset: Litlington, Cambridgeshire, UK. https://cresset-group.com/flare/.

80. LeadFinder; BiolMolTech: Toronto, Ontario, Canada. https://cresset-group.com/lead-finder/.

81. Stroganov, O. V.; Novikov, F. N.; Stroylov, V. S.; Kulkov, V.; Chilov, G. G. Lead Finder: An Approach To Improve Accuracy of Protein−Ligand Docking, Binding Energy Estimation, and Virtual Screening. *J. Chem. Inf. Model.* **2008**, *48* (12), 2371–2385. https://doi.org/10.1021/ci800166p.

82. Tian, H.; Xiao, S.; Jiang, X.; Tao, P. PASSer: Fast and Accurate Prediction of Protein Allosteric Sites. *Nucleic Acids Res.* **2023**, *51* (W1), W427–W431. https://doi.org/10.1093/nar/gkad303.

83. Jez, J. M.; Schlegel, B. P.; Penning, T. M. Characterization of the Substrate Binding Site in Rat Liver 3α-Hydroxysteroid/Dihydrodiol Dehydrogenase. *J. Biol. Chem.* **1996**, *271* (47), 30190–30198. https://doi.org/10.1074/jbc.271.47.30190.

84. Nakamura, K.; Kondo, S.; Kawai, Y.; Nakajima, N.; Ohno, A. Purification and Characterization of *α* -Keto Ester Reductases from Bakers' Yeast. *Biosci. Biotech. Biochem.* **1994**, *58* (12), 2236–2240. https://doi.org/10.1271/bbb.58.2236.

85. Ishihara, K.; Kondo, S.; Nakamura, K.; Nakajima, N. Protein Sequences of Two Keto Ester Reductases: Possible Identity as Hypothetical Proteins. *Biosci. Biotech. Biochem.* **1996**, *60* (9), 1538–1539. https://doi.org/10.1271/bbb.60.1538.

86. Heidlas, J.; Tressl, R. Purification and Properties of Two Oxidoreductases Catalyzing the Enantioselective Reduction of Diacetyl and Other Diketones from Baker's Yeast. *Eur. J. Biochem.* **1990**, *188* (1), 165–174. https://doi.org/10.1111/j.1432-1033.1990.tb15384.x.

87. Di Costanzo, L.; Drury, J. E.; Penning, T. M.; Christianson, D. W. Crystal Structure of Human Liver Δ4-3-Ketosteroid 5β-Reductase (AKR1D1) and Implications for Substrate Binding and

Catalysis. *J. Biol. Chem.* **2008**, *283* (24), 16830–16839. https://doi.org/10.1074/jbc.M801778200.

88. Fabrini, R.; De Luca, A.; Stella, L.; Mei, G.; Orioni, B.; Ciccone, S.; Federici, G.; Lo Bello, M.; Ricci, G. Monomer−Dimer Equilibrium in Glutathione Transferases: A Critical Re-Examination. *Biochemistry* **2009**, *48* (43), 10473–10482. https://doi.org/10.1021/bi901238t.

89. Maser, E.; Völker, B.; Friebertshäuser, J. 11β-Hydroxysteroid Dehydrogenase Type 1 from Human Liver: Dimerization and Enzyme Cooperativity Support Its Postulated Role as Glucocorticoid Reductase. *Biochemistry* **2002**, *41* (7), 2459–2465. https://doi.org/10.1021/bi015803t.

90. Maser, E.; Friebertshauser, J.; Volker, B. Purification, Characterization and NNK Carbonyl Reductase Activities of 11b-Hydroxysteroid Dehydrogenase Type 1 from Human Liver: Enzyme Cooperativity and Significance in the Detoxification of a Tobacco-Derived Carcinogen. *Chem. Biol. Interact.* **2003**, *143–144*, 435–448.

91. Wsól, V.; Szotáková, B.; Skálová, L.; Maser, E. The Novel Anticancer Drug Oracin: Different Stereospecificity and Cooperativity for Carbonyl Reduction by Purified Human Liver 11β-Hydroxysteroid Dehydrogenase Type 1. *Toxicology* **2004**, *197* (3), 253–261. https://doi.org/10.1016/j.tox.2004.01.009.

92. Chai, X.; Zhai, Y.; Napoli, J. L. cDNA Cloning and Characterization of a Cis-Retinol/3α-Hydroxysterol Short-Chain Dehydrogenase. *J. Biol. Chem.* **1997**, *272* (52), 33125–33131. https://doi.org/10.1074/jbc.272.52.33125.

93. Su, J.; Chai, X.; Kahn, B.; Napoli, J. L. cDNA Cloning, Tissue Distribution, and Substrate Characteristics of a Cis-Retinol/3α-Hydroxysterol Short-Chain Dehydrogenase Isozyme. *J. Biol. Chem.* **1998**, *273* (28), 17910–17916. https://doi.org/10.1074/jbc.273.28.17910.

94. Rosemond, M. J. C.; St. John-Williams, L.; Yamaguchi, T.; Fujishita, T.; Walsh, J. S. Enzymology of a Carbonyl Reduction Clearance Pathway for the HIV Integrase Inhibitor, S-1360: Role of Human Liver Cytosolic Aldo-Keto Reductases. *Chem. Biol. Interact.* **2004**, *147* (2), 129–139. https://doi.org/10.1016/j.cbi.2003.12.001.

95. Garavaglia, P. A.; Cannata, J. J. B.; Ruiz, A. M.; Maugeri, D.; Duran, R.; Galleano, M.; García, G. A. Identification, Cloning and Characterization of an Aldo-Keto Reductase from *Trypanosoma cruzi* with Quinone Oxido-Reductase Activity. *Mol. Biochem. Parasit.* **2010**, *173* (2), 132–141. https://doi.org/10.1016/j.molbiopara.2010.05.019.

96. Schlegel, B. P.; Ratnam, K.; Penning, T. M. Retention of NADPH-Linked Quinone Reductase Activity in an Aldo-Keto Reductase Following Mutation of the Catalytic Tyrosine. *Biochemistry* **1998**, *37* (31), 11003–11011. https://doi.org/10.1021/bi980475r.

97. Debebe, T.; Krüger, M.; Huse, K.; Kacza, J.; Mühlberg, K.; König, B.; Birkenmeier, G. Ethyl Pyruvate: An Anti-Microbial Agent That Selectively Targets Pathobionts and Biofilms. *PLoS ONE* **2016**, *11* (9), e0162919. https://doi.org/10.1371/journal.pone.0162919.

98. Sun, L.; Chen, Y.; Rajendran, C.; Mueller, U.; Panjikar, S.; Wang, M.; Mindnich, R.; Rosenthal, C.; Penning, T. M.; Stöckigt, J. Crystal Structure of Perakine Reductase, Founding Member of a Novel Aldo-Keto Reductase (AKR) Subfamily That Undergoes Unique Conformational Changes during NADPH Binding. *J. Biol. Chem.* **2012**, *287* (14), 11213–11221. https://doi.org/10.1074/jbc.M111.335521.

99. Xiao, Z.; Zha, J.; Yang, X.; Huang, T.; Huang, S.; Liu, Q.; Wang, X.; Zhong, J.; Zheng, J.; Liang, R.; Deng, Z.; Zhang, J.; Lin, S.; Dai, S. A Three-Level Regulatory Mechanism of the Aldo-Keto Reductase Subfamily AKR12D. *Nat. Commun.* **2024**, *15* (1), 2128. https://doi.org/10.1038/s41467-024-46363-z.

100. Tian, H.; Jiang, X.; Tao, P. PASSer: Prediction of Allosteric Sites Server. *Mach. Learn.: Sci. Technol.* **2021**, *2* (3), 035015. https://doi.org/10.1088/2632-2153/abe6d6.

101. Davies, G. E.; Stark, G. R. Use of Dimethyl Suberimidate, a Cross-Linking Reagent, in Studying the Subunit Structure of Oligomeric Proteins. *Proc. Natl. Acad. Sci. U.S.A.* **1970**, *66* (3), 651–656. https://doi.org/10.1073/pnas.66.3.651.

102. Moses, J. A. Investigating the Effects of pH and Salt Concentration on Substrate Inhibition of Yeast Aldo-Keto Reductase 163, Drew University, 2024.

Appendix

Derivation of the Michaelis-Menten Equation

Derivation of the Michaelis-Menten model requires several key assumptions. The first is that the enzyme and substrate form an enzyme-substrate complex, or ES complex.[16] As shown in Equation 1, the ES complex can either break down to enzyme (E) and substrate (S), or it can proceed to product (P) formation.

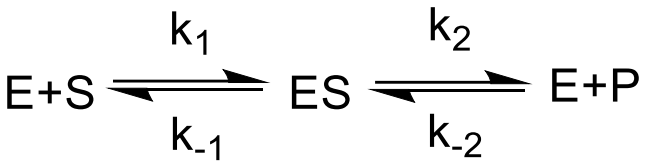

(1)

The rate constant k_{-2} describes the reverse reaction in which E and P react to re-form the ES complex. To prevent products from influencing the reaction via product inhibition, Michaelis and Menten measured the initial velocity of enzymatic reactions, when product formation was negligible.[16] Thus, Equation 1 can be simplified by considering only initial velocities in which the reverse reaction described by k_{-2} does not occur to any appreciable extent. This permits the omission of k_{-2}, leading to Equation 2.

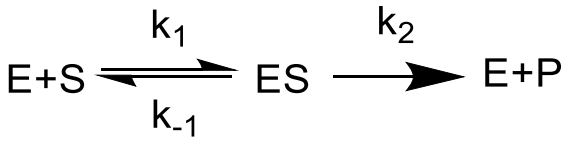

(2)

Michaelis and Menten assumed that the rate of an enzyme-catalyzed reaction was proportional to the ES complex concentration.[16] This relationship is represented by Equation 3, in which V_0 represents catalytic velocity, or the rate of product formation.

$$V_0 = k_2[ES] \text{ (3)}$$

The next step in the derivation is to relate Equation 3 to Equation 2, which includes the enzyme and substrate concentrations and additional rate constants.[12] To do this, [ES] is expressed using the terms of Equation 2, as shown in equations 4 and 5.

$$\text{Rate of formation of ES} = k_1[E][S] \text{ (4)}$$

$$\text{Rate of breakdown of ES} = (k_{-1} + k_2)[ES] \text{ (5)}$$

Equations 4 and 5 can be simplified using the steady-state assumption, otherwise known as the Briggs-Haldane assumption. According to the steady-state assumption, because the total substrate concentration is much larger than the total enzyme concentration, the rate of change of [ES] is negligible compared to the rate of change of the substrate and product concentrations.[16] Thus, [ES] is assumed to be constant, and the rates of ES complex formation and breakdown are assumed to be equal. This allows Equations 4 and 5 to be set equal to each other, producing Equation 6.

$$k_1[E][S] = (k_{-1} + k_2)[ES] \text{ (6)}$$

Equation 6 can be rearranged to give Equation 7.

$$\frac{[E][S]}{[ES]} = \frac{k_{-1}+k_2}{k_1} \text{ (7)}$$

The expression on the right side of Equation 7 simplifies to a constant known as K_M, or the Michaelis constant, which has units of concentration.[12] This is shown in Equation 8.

$$K_M = \frac{k_{-1}+k_2}{k_1} \text{ (8)}$$

One can then substitute K_M into Equation 7 and solve for [ES] to yield Equation 9.

$$[ES] = \frac{[E][S]}{K_M} (9)$$

In Equation 9, [S] and [E] represent uncombined substrate and enzyme, respectively. Because the total substrate concentration is much larger than the total enzyme concentration,[16] [S] is assumed to be the same as the total substrate concentration. In addition, [E] can be represented as the total enzyme concentration ($[E]_T$) minus [ES], as shown in equation 10.

$$[E] = [E]_T - [ES] (10)$$

Substituting Equation 10 for [E] in Equation 9 gives Equation 11.

$$[ES] = \frac{([E]_T - [ES])[S]}{K_M} (11)$$

Solving Equation 11 for [ES] gives Equation 12.

$$[ES] = \frac{{}^{[E]_T[S]}/_{K_M}}{1+{}^{[S]}/_{K_M}} (12)$$

Equation 12 can be rearranged to give Equation 13.

$$[ES] = [E]_T \frac{[S]}{[S]+K_M} (13)$$

Equation 13 can then be substituted into Equation 3 to obtain Equation 14.

$$V_0 = k_2[E]_T \frac{[S]}{[S]+K_M} (14)$$

When $[ES]=[E]_T$, all enzyme active sites are saturated with substrate, and the maximum enzyme velocity is obtained.[12] Thus, V_{max} can be defined as shown in Equation 15.

$$V_{max} = k_2[E]_T \text{ (15)}$$

Substituting Equation 15 into Equation 14 yields the final form of the Michaelis-Menten equation, or Equation 16.

$$V_0 = V_{max}\frac{[S]}{[S]+K_M} \text{ (16)}$$

Results of E4ClAA and 2,3-PD Docking into Allosteric Sites

Table 12. Scores and interactions for E4ClAA's docking poses in pocket 1.

Pose	Rank Score	dG (kcal/mol)	Hydrogen-Bonding Contacts (Distance in Å)	Van der Waals Contacts (Number of Interactions)	Steric Clashes (Distance in Å)
1	-2.243	-4.947	R227A (2.1), L237A (1.8)	F231A, R227A (2), L237A	I235 (3.0)
2	-1.891	-4.655	L237A (2.1)	L236A, F231A	R227A (3.0)
3	-1.852	-4.721	L237A (2.7, 2.0)	L236A	L236A (2.9)
4	-1.84	-4.852	L237A (2.3)	L236A, F231	T280 (3.0)
5	-1.821	-4.734	L237A (2.0)	L236A	I235 (2.8), Q278A (2.9)

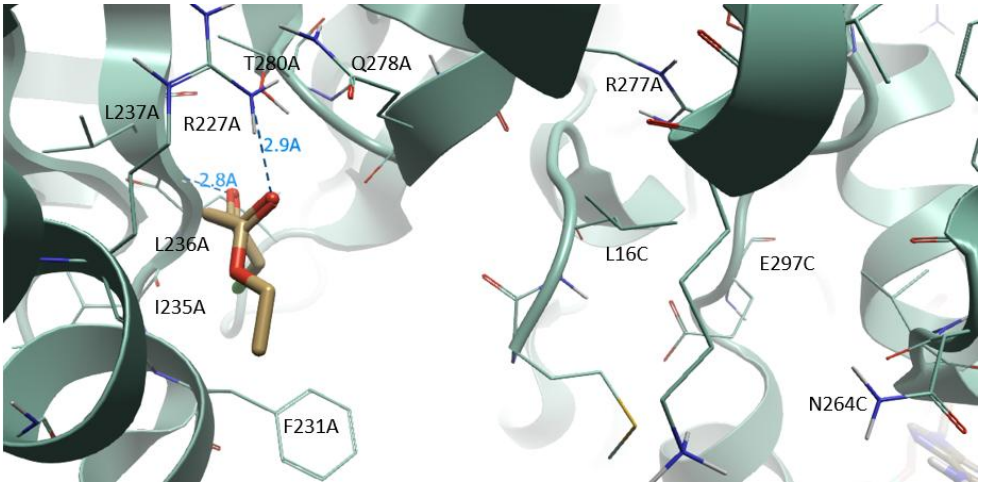

Figure 53. E4ClAA pose 1 docked into pocket 1.

Table 13. Scores and interactions for 2,3-PD's docking poses in pocket 1.

Pose	Rank Score	dG (kcal/mol)	Hydrogen-Bonding Contacts (Distance in Å)	Van der Waals Contacts (Number of Interactions)	Steric Clashes (Distance in Å)
1	-2.057	-3.619	L237A (2.0), T280A (2.5), R227A (2.5)	F231A, L236A, R227A	
2	-1.864	-3.458	R277A (1.9, 2.7, 2.0)	L16C (3), N264C	E297C (2.9)
3	-1.818	-3.53	L237A (2.0)	F231 (2), L236A, R227A (2)	I235A (3.0)
4	-1.741	-3.503	L237A (2.0)	R227A, L236	T280 (2.9)
5	-1.694	-3.433	L237A (2.1)	L237A (3), R227A (2), L236A	

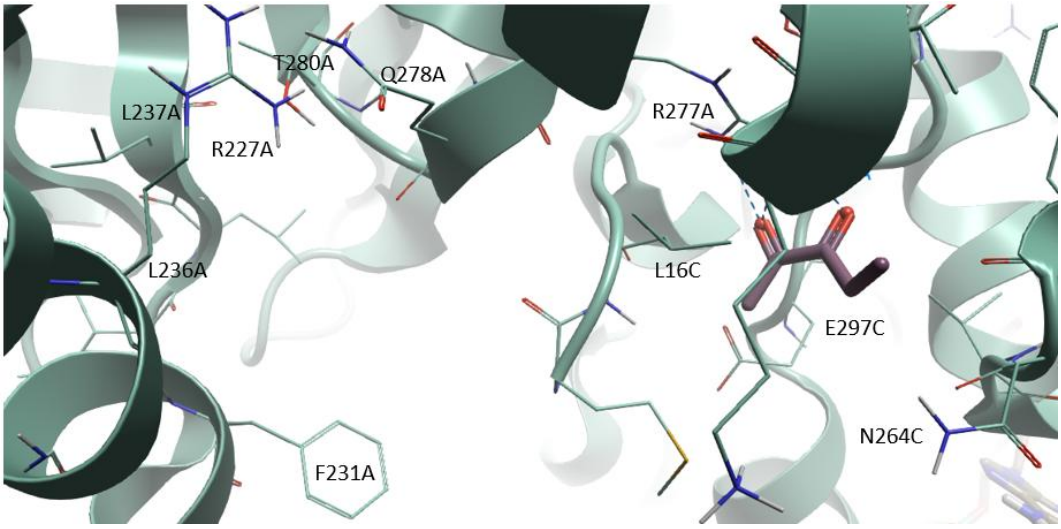

Figure 54. 2,3-PD pose 2 docked into pocket 1.

Table 14. Scores and interactions for E4ClAA's docking poses in pocket 2.

Pose	Rank Score	dG (kcal/mol)	Hydrogen-Bonding Contacts (Distance in Å)	Van der Waals Contacts (Number of Interactions)
1	-2.131	-4.615	N264C (2.7), R277A (2.0, 2.3, 2.3)	Y263C, V265C
2	-2.07	-4.618	K303C (3.1), N264A (3.1)	L16A
3	-2.032	-4.357	R227C (2.0)	K228C, F231C
4	-1.949	-4.941	R277C (2.0, 3.0), N264A (2.1), K303C (2.8)	L16A (2), N264A
5	-1.795	-4.739	R277C (2.0, 2.1), K303C (2.7)	V265A, M15A, E297A

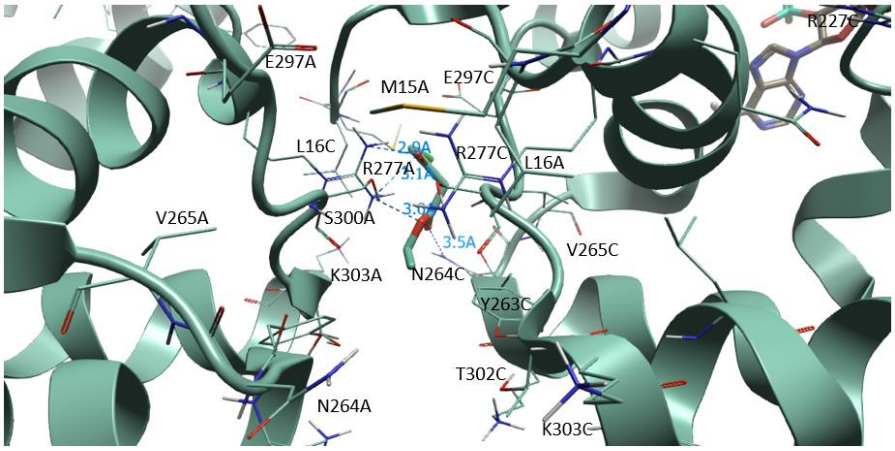

Figure 55. E4ClAA pose 1 docked into pocket 2.

Table 15. Scores and interactions for 2,3-PD's docking poses in pocket 2.

Pose	Rank Score	dG (kcal/mol)	Hydrogen-Bonding Contacts (Distance in Å)	Van der Waals Contacts (Number of Interactions)	Steric Clashes (Distance in Å)
1	-1.973	-3.062	R227C (1.9, 2.7)	F231C, R227C	T280C (2.8)
2	-1.927	-3.397	R277C (1.9), N264A (2.2)	L16A, V265A	
3	-1.862	-3.349	R277A (2.0, 2.6, 2.0)	L16C (4), N264C	E297C (2.9)
4	-1.791	-3.128	R227C (2.1)	F231C (2), L237C (2), R227C (2.1)	
5	-1.77	-3.071	R227C (2.0)	L237C (3), R227C (2), F231C	

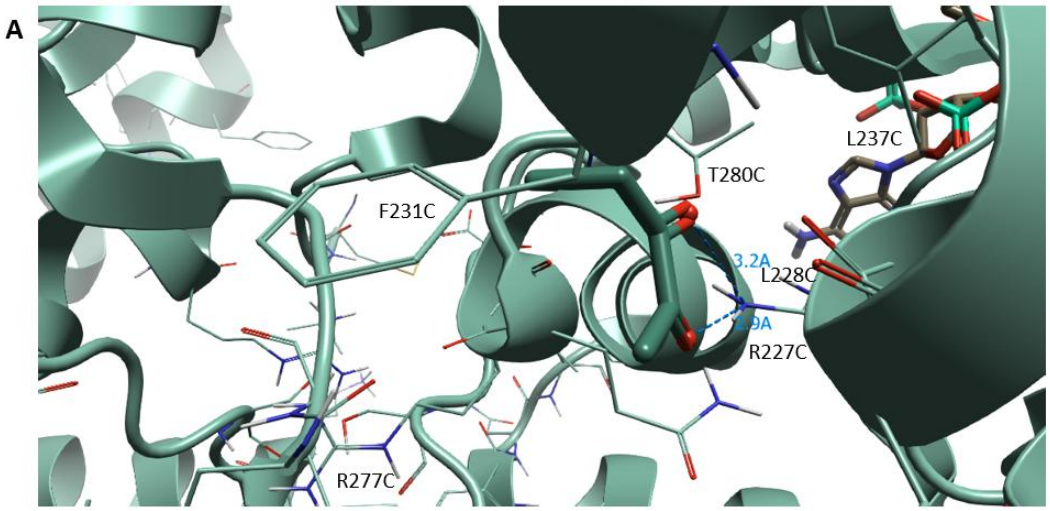

Figure 56. 2,3-PD pose 1 docked into pocket 2.

Table 16. Scores and interactions for E4ClAA's docking poses in pocket 3.

Pose	Rank Score	dG (kcal/mol)	Hydrogen-Bonding Contacts (Distance in Å)	Van der Waals Contacts (Number of Interactions)	Steric Clashes (Distance in Å)
1	-2.149	-4.071	R111C (2.0), D110C (2.7, 1.8), V109C (2.5)	E108C, R111C	Q173C (2.7)
2	-2.124	-4.074	D110C (2.1, 2.7), R111C (2.0)	K176C, Q173 (2)	
3	-2.102	-3.831	V109C (2.9), D110C (2.1, 2.7), R111C (2.0)	I177C (2), D110C	
4	-1.975	-3.587	R111C (1.8), D110C (2.1), V109C (2.5)	R111C	Q173C (2.6), D107C (3.0)
5	-1.74	-3.873	R111C (1.8), V109C (2.3), D110C (2.1)	D110C (2), I177C (2)	Q173C (2.7)

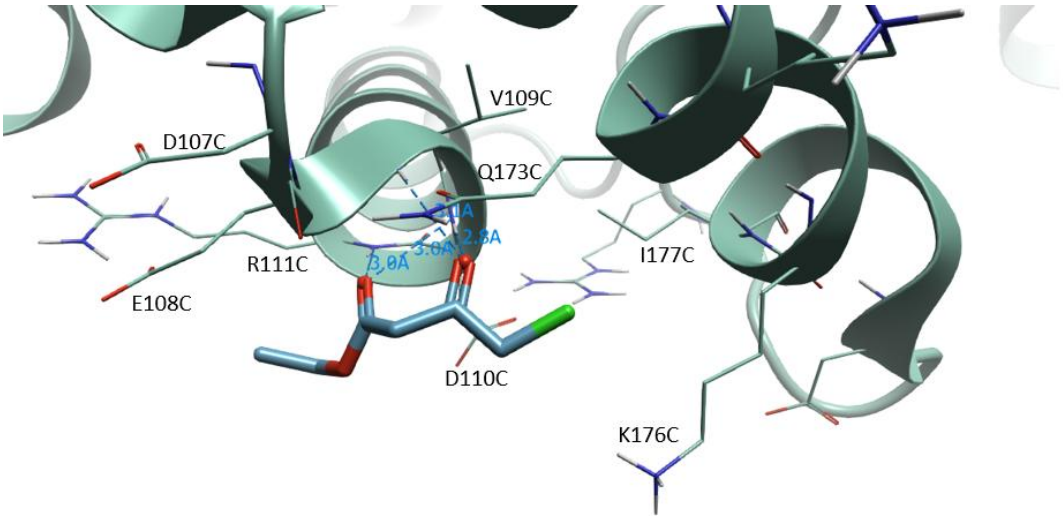

Figure 57. E4ClAA pose 1 docked into pocket 3.

Table 17. Scores and interactions for 2,3-PD's docking poses in pocket 3.

Pose	Rank Score	dG (kcal/mol)	Hydrogen-Bonding Contacts (Distance in Å)	Van der Waals Contacts (Number of Interactions)	Steric Clashes (Distance in Å)
1	-2.033	-3.011	V109C (2.4), D110C (1.9, 2.7), R111C (2.0)	E108C (2)	
2	-1.97	-2.93	R111C (2.0), D110C (2.7, 2.0), V109C (2.3)		Q173C (2.7)
3	-1.819	-3.116	V109C (2.2), D110C (2.1, 2.0)	K176C (2), I177C (2)	Q173 (2.7)
4	-1.672	-3.012	D110C (1.9), V109C (2.4)	K176C, I177C (4), D110C (2)	Q173C (2.8)
5	-1.473	-2.803	K176C (2.5), D110C (2.1)	K176C, I177C (4), D110C	

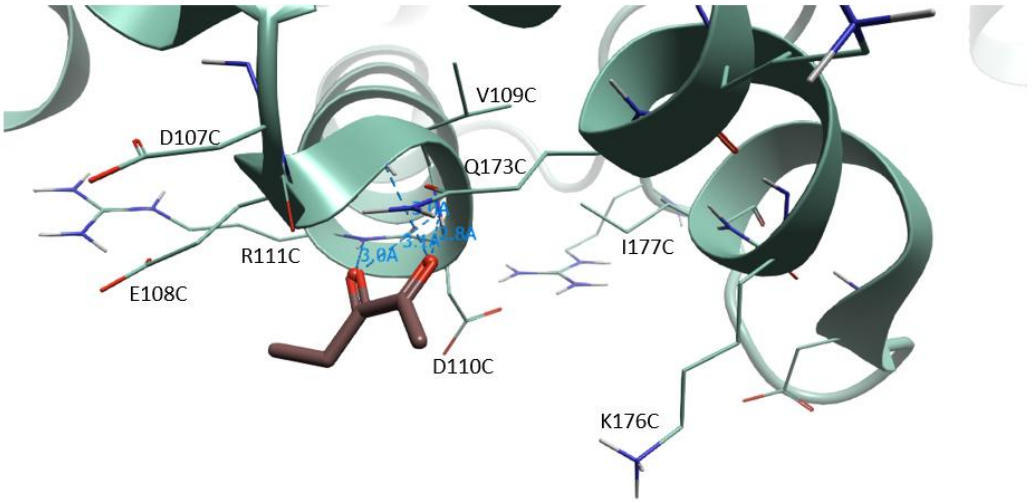

Figure 58. 2,3-PD pose 1 docked into pocket 3.